HARVARD
Kenneth C. Griffin

GRADUATE SCHOOL
OF ARTS AND SCIENCES

DISSERTATION ACCEPTANCE CERTIFICATE

The undersigned, appointed by the

Department of Chemistry & Chemical Biology

have examined a dissertation entitled:

Development of Halo Tag-Based Tools for Recording Synaptic Dynamics

presented by: Doyeon Kim

candidate for the degree of Doctor of Philosophy and hereby certify that it is worthy of acceptance.

Signature _____

Typed name: Professor Adam E. Cohen

Signature _____

Typed name: Professor Xiaowei Zhuang

Signature _____

Typed name: Professor Bernardo L. Sabatini

Date: 7 Apr 2025

Development of HaloTag-Based Tools for Recording Synaptic Dynamics

a dissertation presented by
Doyeon Kim
to
The Department of Chemistry and Chemical Biology

in partial fulfillment of the requirements for
the degree of
Doctor of Philosophy in
the subject of Chemistry

Harvard University
Cambridge, Massachusetts
April 2025

©2025 – Doyeon Kim
all rights reserved.

Dissertation Advisor: Professor Adam E. Cohen Doyeon Kim

Development of HaloTag-Based Labeling Tools for Synaptic Activity Dynamics

Abstract

Synaptic transmission and plasticity are fundamental processes that underlie inter-neuronal communication, learning, and memory. However, current methods for tracking synaptic changes *in vivo* have limited spatial resolution, imaging depth, and imaging volume. This dissertation presents two novel HaloTag-based molecular labeling techniques designed to map presynaptic activity and postsynaptic plasticity *in situ* in live animals.

The first technique, Extracellular Protein Surface Labeling in Neurons (EPSILON), uses a pulse-chase strategy with membrane-impermeable dyes to selectively track α-amino-3-hydroxy-5-methyl-4-isoxazolepropionic acid receptor (AMPAR) exocytosis, a key indicator of synaptic potentiation. By labeling newly surface-exposed AMPARs at genetically targeted synapses, EPSILON provides high-resolution maps of synaptic plasticity *in vivo*. In hippocampal CA1 pyramidal neurons, EPSILON was employed to investigate the relationship between AMPAR exocytosis and cFos expression during contextual fear conditioning. This study revealed a strong correlation between synaptic potentiation and immediate early gene

activation, suggesting a synapse-level mechanism for the formation of memory engrams. Additionally, EPSILON uncovered spatial patterns of synaptic plasticity, including preferential potentiation in perisomatic dendrites and localized clustering of potentiated spines, highlighting the structured organization of synaptic modifications during learning.

The second technique enables time-resolved tracking of presynaptic vesicle release, *in vitro* and *in vivo*. This method uses HaloTag fusion constructs of presynaptic proteins, such as synaptophysin and vesicular glutamate transporter 1, to selectively label active presynaptic terminals upon neurotransmitter vesicle exocytosis. In cultured neurons, optogenetic stimulation or chemical depolarization significantly increased HaloTag dye labeling on presynaptic boutons, demonstrating the method's sensitivity to presynaptic activity. In live mice, this technique was used to map presynaptic activity under optogenetic stimulation or sensory deprivation, revealing distinct patterns of presynaptic vesicle release dynamics in response to neural activity changes *in vivo*. Furthermore, sequential labeling with multiple dyes confirmed that this approach enables multiplexed tracking of synaptic activity across different time points, providing a powerful tool for studying functional synaptic connectivity in naturalistic conditions.

Together, these two techniques offer complementary approaches for investigating the dynamics of synaptic activity and plasticity. Unlike conventional real-time imaging methods, which are limited by optical access and restricted fields of view, these HaloTag-based approaches enable synaptic events to be recorded *in situ* and

read out *ex vivo*, allowing for comprehensive analysis of synaptic modifications throughout the brain. Future applications of these methods may include simultaneous tracking of presynaptic and postsynaptic changes, brain-wide mapping of synaptic modifications, and integration with advanced imaging, proteomic, or transcriptomic approaches. By enhancing the ability to study synaptic changes *in vivo* with high precision, this dissertation contributes to a deeper understanding of the molecular mechanisms underlying functional neural circuits in the brain.

Contents

Title Page i
Copyright ii
Abstract iii
Table of Contents vi
List of Figures vii
Dedication viii
Acknowledgements ix
1 Introduction 1
1.1 Molecular mechanisms underlying synaptic transmission 5
1.2 Molecular mechanisms underlying synaptic plasticity 7
1.3 Molecular integrators 9
1.4 HaloTag labeling approaches 10
1.5 HaloTag labeling for synapses 12
1.6 Pulse-chase HaloTag labeling of synaptic transmission and plasticity 12
2 EPSILON: A method for pulse-chase labeling to probe synaptic AMPAR exocytosis during memory formation 14
2.1 Abstract 15
2.2 Introduction 15
2.3 Results 20
2.4 Discussion 35
2.5 Methods 41
2.6 Supplemental figures 63
2.7 Manuscript information 78
3 Multicolor HaloTag labeling for mapping presynaptic dynamics 80
3.1 Abstract 81
3.2 Introduction 81
3.3 Results 84
3.4 Discussion 98
3.5 Methods 100
3.6 Manuscript information 110
4 Conclusion 111
References 120

List of figures

2.1 EPSILON tags freshly exposed AMPARs 19

2.2 EPSILON reports sensory-induced AMPAR exocytosis *in vivo* 25

2.3 Contextual fear conditioning evokes correlated changes in AMPAR exocytosis and cFos expression 30

2.4 Sub-cellular distribution of AMPAR exocytosis after CFC in CA1 pyramidal neurons 34

2.5 *In vitro* characterization of EPSILON 64

2.6 Effects of MNI-glutamate uncaging and cLTP on AMPAR exocytosis 66

2.7 Validation of EPSILON in mouse brain 68

2.8 HaloTag dye labeling in live mouse brain 70

2.9 Validation of contextual fear conditioning protocol 71

2.10 Relationships among cFos expression, AMPAR exocytosis levels, and percentage of potentiated spines 72

2.11 Subcellular distribution of potentiated spines 74

2.12 Comparison of AMPAR exocytosis in basal vs. apical dendrites 75

2.13 Clustering of potentiated spines in context-only control 76

2.14 Possible extensions of the EPSILON technique 77

3.1 Induced synaptic activity increases the dye-labeling levels of Syp-HT and vGluT1-HT *in vitro* 87

3.2 Multi-color HaloTag labeling of presynaptic synaptophysin pools in mouse barrel cortex 90

3.3 Optogenetically induced synaptic activity increases the dye-labeling levels of Syp-HT *in vivo* 92

3.4 Sensory deprivation decreases the *in vivo* dye-labeling levels of Syp-HT in the barrel cortex 95

3.5 Sequential injections of membrane-impermeable dyes consistently label released vesicles without saturation 97

To my family.

Acknowledgments

First, I want to express my heartfelt gratitude to my wonderful wife, Hyun Ji Yoo, who has been my mental, emotional, and linguistic support throughout my Ph.D. journey. Meeting her in this city, dating her, and eventually marrying her are the highest three achievements of my life. Every day, I am inspired by her broad perspectives and diverse interests. Our after-work life—enjoying her delicious cooking, playing board and mobile games together, skiing, and more—motivates me to work hard and allows me to focus more on my science during the day (and sometimes during the night).

I also acknowledge my mother, Kilim Lee, for her continuous and unconditional support in every aspect of my life, always cheering me on in the career path I choose. I extend my sincere thanks to my sister, Jiyun Kim. As both a family member and a fellow scientist, she has been a steadfast ally in my journey. I also want to thank my parents-in-law and brother-in-law for their unwavering support.

I extend my deepest appreciation to my advisor, Adam Cohen, for his exceptional mentorship over the past six years. His lab mantra, “In our lab, we do what we need to do, not what we can do,” inspired me to tackle challenging scientific questions. His emphasis on collaboration and continuous learning has significantly influenced my development both professionally and personally, and his sincere dedication to his students' growth is truly motivating. Moreover, his ability to balance a demanding academic career with his dedication to his family exemplifies what it means to be both a brilliant scientist and a remarkable human being.

One of the great privileges I experienced during my Ph.D. in the Cohen lab was the opportunity to work with incredibly talented colleagues from diverse cultural and scientific backgrounds—Urs Boehm, Phil Brooks, David Combs, Hunter Davis, Linlin Fan, Daozheng Gong, Rebecca Frank Hayward, Maddie Howell, Yi-Chieh Huang, Sarah Innes-Gold, Daniel Itkis, Bill Jia, Xiuyuan (Ted) Li, Byung Hun Lee, Dingchang Lin, Harry McNamara, Eric Moult, Ethan Perets, Pojeong Park, Yitong Qi, He Tian, Yangdong Wang, David Wong-Campos, Xiang Wu, Katherine Xiang, Junjie Xu, and Jinfan Zhang. I learned a great deal from all of them, both in science and in life, and I truly enjoyed my time at Harvard. Special thanks go to David Wong-Campos and Pojeong Park for the engaging scientific and non-

scientific discussions that greatly contributed to my growth as a mature scientist. I also thank He Tian for her dedicated mentorship during my rotation and for her invaluable advice later on.

I thank Shahin Begum, Camila Bodden, Maggie Kenar, Hillary Piccerillo, and Andrew Preecha for their invaluable assistance over the years. I also thank the rotation and undergraduate students—Phil Che, Mona Liu, Ariana-Dalia Vlad, and Jiahao Zhang.

Beyond the lab, I was fortunate to collaborate and engage in insightful discussions with great scientists—individuals I aspire to emulate in the future. I am deeply grateful to Luke Lavis and Jonathan Grimm for their state-of-the-art HaloTag technologies, which made all of my Ph.D. research projects possible. The scientific discussions during conferences and on Zoom with Seth Grant, Michael Hoppa, Richard Huganir, YoungJu Jo, Boaz Mohar, Steve Ramirez, Bernardo Sabatini, Nelson Spruston, Karel Svoboda, Michael Tadross, and Ryohei Yasuda were invaluable in enhancing the sophistication of my project and fostering my intellectual growth. I also thank the professors who served on my thesis committee, Xiaowei Zhuang and Bernardo Sabatini, whose insights and guidance greatly enhanced my research.

All my friends in Korea, Boston, and other parts of the world have also been great support during my Ph.D. Special thanks to the members of the band JACS for creating unforgettable memories at the three concerts we shared, and to Joonhyuk Cho, Eunseok Lee, and Jaeyeon Won for their help during my wedding. I also thank all the tennis players in the Boston area who have played with me for their patience.

I also give special thanks to my undergraduate advisors, Insung Choi, YongKeun Park, and Jerrin Kuriakose who encouraged me to pursue a Ph.D. in the USA and introduced me to the world of research in Chemistry and Physics.

I thank the Harvard Chemistry and Chemical Biology Department, the Harvard Center for Biological Imaging, the Simmons family, and the Korea Foundation for Advanced Studies for their prize and funding support.

1

Introduction

Rapid intercellular communication is fundamental to cell biology, and understanding how signaling dynamics are encoded and transmitted between cells is crucial for elucidating how distinct inputs are integrated across networks to generate systems-level behaviors[1]. In the brain, neurons communicate via synapses, where neurotransmitters such as glutamate are released from the presynaptic terminal and activate corresponding receptors on the postsynaptic membrane[2]. Each neuron integrates excitatory, inhibitory, and neuromodulatory inputs to compute

outputs in the form of subthreshold voltage fluctuations, electrical action potentials, and downstream molecular signaling cascades[3]. The strength of synaptic connections is continuously modified, a process that underlies essential cognitive functions such as learning and memory[4].

In neuroscience, electrophysiological measurements of membrane voltage have been extensively employed to record synaptic inputs and the corresponding neuronal outputs. For instance, patch-clamp recordings enable the quantification of currents generated by individual neurotransmitter quanta, referred to as miniature postsynaptic currents[5]. Changes in synaptic strength can also be detected by measuring currents elicited by electrical stimulation of axons before and after a plasticity-inducing stimulus[6]. While this method remains a powerful tool due to its unparalleled temporal resolution and sensitivity, it lacks spatial information, preventing precise determination of the pre- and post-synaptic origins of recorded synaptic dynamics[7]. Moreover, the patch-clamp technique is severely limited in throughput, prompting research into advances in silicon-based probes[8] that allow simultaneous recordings from hundreds of cells and aim to enhance sensitivity to subthreshold synaptic inputs.

Real-time optical imaging using genetically engineered sensors for ions and small molecules holds significant promise due to its spatial resolution and high throughput[7]. Moreover, the cell-type-specific expression of these sensors confers genetic specificity, thereby facilitating studies of the functions and roles of various

neuronal populations in the brain[7]. Genetically encoded calcium indicators (GECIs)[9] have been widely used to monitor the calcium influx that follows neuronal activities, while recent advances in genetically encoded voltage indicators (GEVIs)[10] have enabled the direct visualization of membrane voltage fluctuations. Although both sensor types have reported subregional calcium[11] and voltage[12,13] dynamics in neurons, using these sensors to measure synaptic activities remains challenging because calcium ions and membrane voltage fluctuate dynamically at both cellular and synaptic levels. Therefore, additional efforts are required to decouple cell-wide and subcellular signals[14].

To address this issue, fluorescent sensors for synapse-specific molecular events have been developed for use with real-time optical imaging. For example, the sensor iGluSnFR[15] directly converts released synaptic glutamate into a fluorescent signal. Additionally, the pH-dependent green fluorescent protein superecliptic pHluorin (SEP)[16] was fused to presynaptic vesicular proteins, such as synaptophysin[17] or vesicular glutamate transporter 1 (vGluT1)[18], to monitor presynaptic vesicle release via pH changes changes between the neutral extracellular space vs. the acidic vesicle lumen.

Real-time optical imaging has been employed to measure the dynamics of synaptic strength as well. One common proxy for synaptic strength is spine size; by using constitutively expressed fluorescent proteins, researchers have tracked the size of individual spines under various behavioral paradigms that induce memory

formation[19,20]. Measuring SEP-fused postsynaptic receptors provides a more direct method for estimating synaptic strength, as the density of surface receptors correlates with synaptic efficacy by converting presynaptic chemical signals into electrical signals. Using these sensors, the dynamics of synaptic strength have been observed in response to altered sensory input[20,21] and learning[20].

However, real-time optical imaging has limitations. First, imaging depth is restricted due to the scattering properties of brain tissue[22]. Additionally, limitations in scanning speed constrain the observable area[23]. Consequently, *in vivo* synaptic imaging is typically performed on a few apical tuft dendrites in layer 1, rather than capturing entire neurons within the limited imageable volume[20,21,24]. Moreover, imaging subcortical regions, such as the hippocampus, requires the installation of optical cannulas[25], which is invasive. Finally, despite recent advances in miniaturized microscopes[26], their low numerical aperture means that most *in vivo* synaptic imaging is still conducted on head-fixed animals, a condition that deviates from naturalistic contexts.

Molecular integrators offer an alternative strategy by generating persistent chemical signatures that record transient events *in situ*[27]. Although the encoding occurs within the living organism, the readout is typically obtained *ex vivo*, often after tissue fixation. This enables the history of neuronal events to be traced back to their precise sites of occurrence throughout the brain. Moreover, this approach holds potential for whole-brain dynamics mapping. Recent advances in self-

labeling protein domains, such as SNAP-tag[28] and HaloTag[29]—which are labeled with exogenously introduced synthetic dyes—have even enabled recordings at multiple time points[27].

Although most molecular integrators have focused on recording whole-cell activities, the same principle can be applied to capture synaptic dynamics. Such tools would elucidate the *in vivo* mechanisms of synaptic transmission and plasticity in brain regions that are not yet well understood. Furthermore, they would provide a versatile platform for investigating the synaptic effects of chemical neuromodulators[30] across different brain regions and cell types, ultimately deepening our insight into treatment strategies for neuropsychiatric disorders[31].

The primary aim of this dissertation is to develop novel methods for recording synaptic transmission and plasticity *in vivo* using HaloTag labeling. First, I provide an overview of the molecular mechanisms underlying synaptic transmission and plasticity, which informed the development of these methods. Next, I review the progress in molecular integrators that laid the groundwork for my approach. Finally, I present two HaloTag-based labeling methods designed to assess postsynaptic plasticity and presynaptic vesicle release.

1.1 Molecular mechanisms underlying synaptic transmission

Synaptic transmission is the process that converts electrical impulses into chemical signals crossing the synaptic cleft[3]. This intricate process begins when an action

potential reaches the presynaptic terminal, triggering a cascade of molecular events that trigger release of neurotransmitters[3,32].

Upon the arrival of the action potential, voltage-gated calcium channels open in the presynaptic membrane, allowing an influx of calcium ions into the terminal[32]. This rapid increase in intracellular calcium concentration initiates the vesicle fusion process. Synaptic vesicles, which store neurotransmitters, are docked at the active zone of the presynaptic membrane and undergo a priming process that prepares them for rapid release[33]. The actual fusion of these vesicles with the presynaptic membrane is mediated by a complex of proteins known as SNAREs[34]. Proteins such as synaptobrevin[35] on the vesicle, along with syntaxin[35] and SNAP-25[36] on the plasma membrane, assemble into a SNARE complex that draws the vesicle into close proximity with the membrane. The calcium sensor synaptotagmin[37] detects the influx of calcium and triggers the final fusion event, leading to the exocytosis of neurotransmitters into the synaptic cleft.

Once released, neurotransmitters diffuse rapidly across the synaptic cleft and bind to specific receptors on the postsynaptic membrane. These receptors, which can be ionotropic or metabotropic, transduce the chemical signal into an electrical or biochemical response in the postsynaptic neuron[38]. Ionotropic receptors, such as α-amino-3-hydroxy-5-methyl-4-isoxazolepropionic acid receptors (AMPARs)[39] and N-methyl-D-aspartate receptors (NMDARs)[40], directly mediate changes in membrane potential by permitting the flow of ions, while metabotropic receptors[38]

activate intracellular signaling cascades that modulate neuronal activity over longer time scales. The termination of the synaptic signal is achieved through mechanisms including neurotransmitter reuptake, enzymatic degradation, or diffusion away from the synapse[41]. Additionally, synaptic vesicles are recycled via endocytosis, ensuring that the presynaptic terminal remains prepared for subsequent rounds of transmission[41].

Integral to the vesicular membrane, synaptophysin regulates synaptic vesicle endocytosis and recycling, ensuring a steady supply of vesicles for neurotransmitter release[42]. By interacting with endocytic proteins and synaptobrevin, synaptophysin helps maintain vesicle pool homeostasis and synaptic efficacy, especially during periods of high-frequency synaptic activity[43,44]. Moreover, vGluT1 is essential for excitatory synapses, as it is responsible for loading glutamate—the principal excitatory neurotransmitter—into synaptic vesicles prior to their release[45].

1.2 Molecular mechanisms underlying synaptic plasticity

Synaptic plasticity refers to the ability of synapses to change their strength in response to varying patterns of activity[4]. One well-studied form of plasticity is long-term potentiation (LTP), which is often triggered in brain slices by high-frequency stimulation of presynaptic neurons[46]. This stimulation leads to a rapid influx of calcium ions through NMDARs located on the postsynaptic membrane. The elevated calcium levels activate intracellular signaling cascades, including the

activation of calcium/calmodulin-dependent protein kinase II (CaMKII) and protein kinase C (PKC)[47]. These kinases enhance synaptic strength by phosphorylating AMPARs[48], which increases their ion conductance[49], capturing laterally diffusing AMPARs[50], and promoting the insertion of additional AMPAs into the postsynaptic membrane[51].

In contrast, long-term depression (LTD) represents a decrease in synaptic strength and is typically induced by low-frequency stimulation or prolonged low-level activity[52]. This type of stimulation results in a moderate, sustained rise in postsynaptic calcium levels that preferentially activates protein phosphatases such as calcineurin[53]. These phosphatases dephosphorylate AMPARs and associated proteins[54], leading to the internalization of AMPARs via endocytosis, thereby reducing synaptic efficacy[55]. Additionally, LTD may involve metabotropic glutamate receptors (mGluRs), which initiate signaling pathways that further facilitate receptor removal and synaptic weakening[56].

Beyond these rapid changes, synaptic plasticity also involves slower, transcription-dependent processes that stabilize long-lasting modifications in synaptic strength[46]. These processes include the synthesis of new proteins and the structural remodeling of synapses, such as alterations in dendritic spine morphology[57]. Together, these molecular mechanisms enable dynamic regulation of synaptic connections and are suggested to underlie the basic mechanisms of learning, memory, and overall neural circuit adaptability[4].

1.3 Molecular integrators

Light-gated calcium integrators are among the most prevalent molecular integrators, capturing a snapshot of calcium activity by creating a durable chemical trace during a light-defined time window[27]. For instance, CaMPARI[58] irreversibly shifts from green to red fluorescence in the presence of both calcium and violet light, facilitating the *ex vivo* mapping of circuits activated *in vivo*. Another family of light-gated calcium integrators—including ST-Cal-Light[59], FLiCRE[60], and scFLARE2[61]—further enables transcriptional readout. In these tools, a transcription factor anchored to the cell membrane is released upon the simultaneous presence of calcium and light. This approach allows both *in situ* recording of whole-cell activity and subsequent perturbation by selectively expressing optogenetic actuators or silencers in activated neurons[62].

The principle of light-gated calcium integrators has also been applied to map synaptic activities. Pre- and post-SynTagMa[63]—presynaptically and postsynaptically expressed versions of CaMPARI, respectively—record synaptic calcium signals during synaptic transmission, although local postsynaptic calcium events are often confounded by global calcium influx driven by back-propagating action potentials (bAPs). There are also other types of synaptic molecular recorders which do not rely on calcium events. SynActive[64] combined dendritic targeting element from Arc 5’ and 3’-undranslated region, NMDAR C terminus signal

peptide, and PSD-95-PDZ binding consensus sequence to drive fluorescent protein expression selectively in activated spines. SynaptoZip[65], expressed on presynaptic vesicles, binds the exogenously delivered Synbond peptide upon vesicle exocytosis, thereby labeling active presynaptic terminals. Dual-eGRASP[66] has been used to distinguish four distinct types of synaptic connectivity: engram synapse-to-engram synapse, engram synapse-to-non-engram synapse, non-engram synapse-to-engram synapse, and non-engram synapse-to-non-engram synapse. This approach enables comparisons of spine sizes—a proxy for synaptic plasticity—during memory formation.

These tools share a critical limitation: they provide only a single readout[27]. Ideally, one would track signal changes linked to specific experimental conditions, yet current methods can be confounded by background activity unrelated to the experiment. Moreover, having multiple readouts over time would allow for comparisons of neural activation patterns under various conditions within the same animal. In addition, current light-gated integrators rely on blue[59–61] or violet light[58,63] for activation, which, due to strong tissue scattering, restricts recording depth to less than 1 mm[67], unless using invasive optical fibers[62].

1.4 HaloTag labeling approaches

Self-labeling protein tags are genetically encoded fusion proteins that covalently bind to specific synthetic ligands, allowing for the selective labeling of proteins in

living cells[68]. Among the most commonly used self-labeling tags are HaloTag[69], SNAP-tag[28], and CLIP-tag[70]. HaloTag, for instance, reacts with chloroalkane ligands to form a stable covalent bond. SNAP-tag and CLIP-tag use benzylguanine and benzylcytosine derivatives, respectively, to achieve similar covalent labeling. These technologies enable researchers to attach various probes, such as fluorescent dyes or affinity tags, to their proteins, thereby facilitating dynamic studies of protein localization, interaction, and function in real time[29].

With reaction kinetics that are approximately 10- to 100-fold faster than other self-labeling tags[68], HaloTag is currently the most widely favored self-labeling protein tag. Additionally, the flexibility of choosing different probes from an extensive library[69] allows for multiplexed labeling of neuronal activities at different time points. Protein tickertapes are linearly extending HaloTag-fused protein fibers that incorporate green fluorescent protein (GFP) bands during periods of neural activity[71]. These fibers are stained with different colored HaloTag ligand dyes at various time points, and the resulting color bands—reflecting GFP (neural activity) and the dye signal (measurement time points)—are analyzed *ex vivo*. Another example is Caprola[72], which comprises split HaloTag fragments connected by calmodulin and an M13 peptide. In the presence of high calcium, the split HaloTag pair reconstitutes, enabling labeling by HaloTag-ligand substrates. This system has been successfully used to record asymmetric visual stimulation in flies and zebrafish larvae.

1.5 HaloTag labeling for synapses

HaloTag labeling approaches have primarily focused on recording whole-cell activities[71,72]. While the application of this strategy for recording synaptic activities remains underexplored, several attempts have been made. For example, the lifetime of PSD-95[73]—a scaffold protein of excitatory synapses—was measured at individual synapses across the whole brain by tracking the amount of labeled protein in fixed brain tissue from PSD-95-HaloTag transgenic mice[74]. However, tracking proteins labeled at a single time point can be confounded by basal protein level, prompting subsequent studies to employ a pulse-chase method. In DELTA (Dye Estimation of the Lifetime of proTeins in the brAin)[75], the lifetime of synaptic proteins was measured by initially labeling their HaloTag fusion with one HaloTag-ligand dye and then separately labeling newly synthesized protein constructs with a different colored dye. By measuring the ratio of these dyes, researchers can quantify new protein synthesis normalized to the basal protein level at individual synapses. Although these techniques have successfully visualized protein lifetime dynamics—which change with aging or learning— they do not directly identify the synapses responsible for signal transmission or synaptic strength modifications.

1.6 Pulse-chase HaloTag labeling of synaptic transmission and plasticity

Motivated by the unsolved challenges of mapping synaptic transmission and

plasticity *in vivo*, my dissertation develops novel HaloTag-based pulse-chase synaptic labeling methods. In Chapter 2, I introduce a HaloTag pulse-chase method named EPSILON (Extracellular Protein Surface Labeling in Neurons), designed to selectively label newly exocytosed membrane proteins. After validating EPSILON in primary cultures, acute slices, and live animals, I applied it to label potentiated spines in the hippocampal CA1 during contextual memory formation, revealing a strong correlation between immediate early gene expression and synaptic potentiation.

Building on this, Chapter 3 applies the principles of EPSILON to selectively label released presynaptic vesicles during synaptic transmission. This technique, validated in both primary cultures and live animals, can distinguish differences in presynaptic activity levels following optogenetic stimulation or sensory deprivation. In Chapter 4, I explore potential applications of the techniques I developed for studying synaptic circuit dynamics *in vivo* and discuss avenues for further improvement.

2

EPSILON:
A method for pulse-chase labeling to probe synaptic AMPAR exocytosis during memory formation

2.1 Abstract

A tool to map changes in synaptic strength during a defined time window could provide powerful insights into the mechanisms of learning and memory. Here, we developed a technique, Extracellular Protein Surface Labeling in Neurons (EPSILON), to map α-amino-3-hydroxy-5-methyl-4-isoxazolepropionic acid receptor (AMPAR) exocytosis *in vivo* by sequential pulse-chase labeling of surface AMPARs with membrane-impermeable dyes. This approach yields synaptic-resolution maps of AMPAR exocytosis, a proxy for synaptic potentiation, in genetically targeted neurons during memory formation. In mice undergoing contextual fear conditioning (CFC), we investigated the relationship between synapse-level AMPAR exocytosis in CA1 pyramidal neurons, and cell-level expression of the immediate early gene product cFos, a frequently used marker of engram neurons. We observed a strong correlation between AMPAR exocytosis and cFos expression, suggesting a synaptic mechanism for the association of cFos expression with memory engrams. The EPSILON technique is a useful tool for mapping synaptic plasticity and may be extended to investigate trafficking of other transmembrane proteins.

2.2 Introduction

Changes in synaptic strength are an important component of learning and memory[76],

but the rules that map a memory onto a specific set of synapses are not well understood. Which synapses represent which memories? How are changes in synaptic strength related to other markers of memory, such as expression of immediate early genes? To answer these questions, one would like a tool to map changes in synaptic strength during a defined time window in genetically defined neurons.

The synaptic density of α-amino-3-hydroxy-5-methyl-4-isoxazolepropionic acid receptors (AMPARs) is a major contributor to synaptic strength[77]. The density of AMPARs changes during long-term potentiation (LTP) via a combination of exocytosis and capture of laterally diffusing AMPARs[50,51]. AMPARs are stored in intracellular vesicles, which fuse with the postsynaptic membrane during LTP, exposing the N-terminal glutamate-binding domain to the extracellular space.

Several techniques have been developed for monitoring AMPAR dynamics in synapses *in vivo*. A fusion of the pH-sensitive Super Ecliptic pHluorin (SEP), to the N terminus of the AMPAR subunit GluA1 shows an increase in fluorescence when acidic AMPAR-containing vesicles fuse with the postsynaptic membrane[24]. The techniques of GFP reconstitution across synaptic partners (GRASP)[78], and its enhancement (eGRASP)[66], map synaptic contact area between genetically defined pairs of neurons. A related technique called synaptic proximity ligation assay (SYNPLA), maps AMPAR density in synapses between genetically defined pairs of neurons[79]. Finally, a technique to biotinylate surface-exposed AMPARs has been

used to track their lateral diffusion *in vivo*[80]. However, no technique has yet been able to identify all the potentiated synapses in a defined neuron, time-window, and arbitrary brain location (e.g., one that is too deep to image in real-time via a cranial window).

Protein labeling with HaloTag ligand (HTL) dyes has been used to probe protein turnover at the level of translation and degradation *in vivo*[74,75]. A fusion of a target protein and the HaloTag receptor (HT) can be covalently and irreversibly labeled with a fluorescent HTL dye. A technique called DELTA (Dye Estimation of the Lifetime of proTeins in the brAin) used saturated labeling of a HT fusion to a target protein with one dye color (pulse) and subsequent labeling of newly synthesized proteins with different colors (chase), to map protein synthesis *in vivo*, with an *ex vivo* readout[75]. Since the dyes used in DELTA were membrane permeable, this technique was not sensitive to membrane trafficking, but only to total protein level.

Here we developed an approach to map AMPAR insertion by pulse-chase labeling of surface AMPARs with membrane-impermeable fluorescent dyes. We call the technique EPSILON (Extracellular Protein Surface Labeling in Neurons). We fused a HT to the N terminus of GluA1 (**Figure 2.1a**). We expressed HT-GluA1 in neurons, and then saturated surface-exposed HT-GluA1 via direct brain injection of a membrane-impermeable HTL dye. A second dye of a different color was then added to label newly surface-exposed HT-GluA1, and the animal was exposed to a

variety of learning paradigms (**Figure 2.1b**). Subsequent *ex vivo* multi-color imaging revealed maps of AMPAR exocytosis with single-synapse resolution across large volumes of brain tissue and in multiple brain regions.

We went on to map synaptic plasticity and cFos expression in hippocampal CA1 pyramidal cells upon contextual fear conditioning (CFC). In mice subjected to CFC, but not in controls, we observed a tight correlation between the degree of synaptic plasticity and the cFos expression level. This finding suggests a synaptic mechanism for the observed association of cFos expression with memory engrams. We also observed more plasticity in perisomatic than in distal synapses; and clusters of plasticity among nearby synapses. These features may reflect interactions between plasticity and dendritic excitability properties[81]. Overall, EPSILON tagging of AMPAR exocytosis is a powerful tool to investigate the distribution and time-course of synaptic plasticity, and we expect that the EPSILON approach could be applied to other transmembrane proteins.

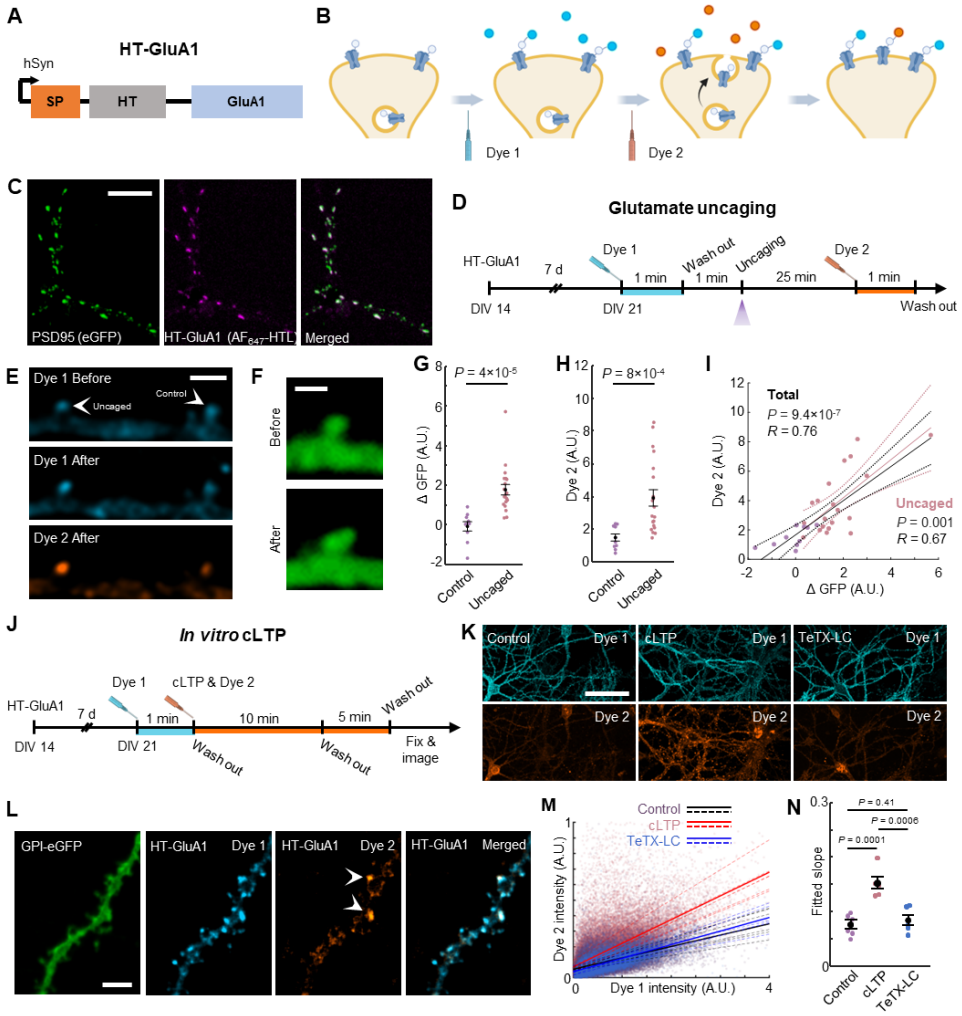

Figure 2.1: EPSILON tags freshly exposed AMPARs. (a) Composition of HT-GluA1: SP, GluA1 signaling peptide; HT, HaloTag receptor. **(b)** EPSILON scheme for labeling freshly surface-exposed AMPARs using membrane-impermeable dyes. Dye 1 saturates HT labeling sites on preexisting HT-GluA1. Dye 2 tags newly exocytosed HT-GluA1. **(c)** HT-GluA1 localization in a neuron. Left: PSD95 (PSD95.FingR-eGFP); Middle: HT-GluA1 (AF_{647}-HTL); Right: Merge. Scale bar, 10 µm. Micrographs represent one of three independent experiments. **(d)** Timeline for pulse-chase labeling during glutamate photo-uncaging. DIV, days *in vitro*. **(e)** Glutamate uncaging triggers AMPAR exocytosis. Top: Preexisting HT-GluA1 (Dye 1); Middle: Dye 1 post-uncaging; Bottom: Newly exposed HT-GluA1 (Dye 2). Scale bar, 2 µm. **(f)** Dendritic spine in GPI-eGFP-labeled neuron before (top) and after (bottom) uncaging. Scale bar, 1 µm. Glutamate uncaging induced **(g)** spine growth and **(h)** increased Dye 2 labeling. Control: $n = 10$ spines; Uncaged: $n = 20$ spines. Two-sided Wilcoxon rank-sum test. Error bars, mean ± s.e.m. **(i)** Correlation between Dye 2 intensity and spine size change (R, Pearson's correlation; P, Student's t-test). **(j)** Timeline for pulse-chase labeling during cLTP. **(k)** Spine labeling for Control, cLTP, and TeTX-LC groups. Top: Preexisting HT-GluA1 (Dye 1); Bottom: Newly exposed HT-GluA1 (Dye 2). Scale bar, 10 µm. **(l)** Spines with elevated HT-GluA1 exocytosis evoked by cLTP. Scale bar, 5 µm. **(m)** cLTP increased Dye 2/Dye 1 ratios. Control: $n = 32{,}828$ spines; cLTP: $n = 47{,}090$; TeTX-LC: $n = 17{,}231$ (6 cultures each). Outliers shown in **Figure 2.6f**. **(n)** Slopes from **(m)**. Two-sided Student's t-test. Error bars, mean ± s.e.m. Parts of (a), (d), and (j) were created using Biorender and are used with permission.

2.3 Results

2.3.1 Development of EPSILON and validation in cultured neurons

We replaced the pH-sensitive SEP domain in SEP-GluA1 with HT to create HT-GluA1. This design used a flexible glycine linker between HT and GluA1 and retained the N-terminal GluA1 signal peptide[82] to ensure proper protein trafficking[24].

We first tested the EPSILON labeling scheme in cultured rat hippocampal neurons. We characterized (1) expression and trafficking of HT-GluA1, (2) the labeling kinetics of membrane impermeable HTL dyes, and (3) the turnover rate of surface HT-GluA1. Live-cell labeling with a membrane-impermeable dye selectively tagged the surface-exposed HT-GluA1 receptors (**Figure 2.5a**). Surface-labeled HT-GluA1 strongly colocalized with the postsynaptic density marker PSD95.FingR-eGFP[83] (Manders' overlap coefficient 0.87 ± 0.025, mean ± s.e.m., n = 13 dendrites from 7 neurons; **Figure 2.1c** and **2.5b**). The sub-cellular distribution of HT-GluA1 labeled with a permeable HTL dye (JF_{549}) strongly correlated with the distribution of all GluA1 as reported by anti-GluA1 immunostaining (Pearson $R = 0.73$, $P < 10^{-4}$, n = 32 spines, 5 neurons; **Figure 2.5c, d**). Anti-GluA1 immunostaining showed no difference in total GluA1 between cells +/- HT-GluA1 expression (**Figure 2.5e**). Together these measurements indicated that the surface-exposed and intracellular pools of HT-GluA1 followed close-to native trafficking patterns.

Pulse labeling of surface HT-GluA1 reached steady state after approximately 300 s for AF_{488} (100 nM), 60 s for JF_{549i} [84] (1 μM), and 60 s for AF_{647} (1 μM; see

Methods for synthesis of AF_{647}-HTL; **Figure 2.5f-i**). Subsequent chase labeling with a different-colored impermeable dye showed no additional labeling (**Figure 2.5j-o**), indicating that the pulse had saturated the surface-exposed HT receptors. In subsequent pulse-chase labeling experiments in cultured neurons, we used conditions that saturated labeling (AF_{488}: 100 nM for 5 min; JF_{549i}: 1 μM for 60 s; AF_{647}: 1 μM for 60 s).

We next determined the basal turnover rate of surface HT-GluA1 (**Figure 2.5p-r**) by pulsing with AF_{488}, and then chasing with JF_{549i} after a variable delay. The ratio of the preexisting (labeled with AF_{488}) and newly inserted (labeled with JF_{549i}) surface HT-GluA1 yielded the turnover rate. The half-life of surface HT-GluA1 was approximately 30 min in cultured neurons.

We then asked whether pulse-chase labeling of surface HT-GluA1 could serve as a proxy of synaptic potentiation. We saturated the surface HT-GluA1 with Dye 1 (AF_{647}), washed out unreacted dye, and then induced structural LTP in individual spines via focally targeted pulsed glutamate uncaging (60 pulses at 1 Hz) in Mg^{2+}-free solution (Methods, **Figure 2.1d**)[85]. Glutamate uncaging triggered rapid spine growth followed by slight shrinkage (**Figure 2.6a, b**), as previously reported[85]. Spine growth trajectories were indistinguishable between neurons +/- HT-GluA1 expression (**Figure 2.6b**), indicating that HT-GluA1 expression did not perturb structural plasticity. We then stained the cells with Dye 2 (JF_{549i}) to label the freshly exocytosed HT-GluA1, and performed high-resolution 3-color confocal imaging of a

non-specific membrane marker (GPI-eGFP), Dye 1, and Dye 2. The spines exposed to glutamate uncaging showed increased spine size (measured by GFP fluorescence, indicating structural LTP), increased Dye 1 signal (likely indicating recruitment of pre-existing surface-exposed HT-GluA1 by lateral diffusion), and increased Dye 2 (indicating freshly exocytosed HT-GluA1; **Figure 2.1e-h** and **2.6c, d**). Finally, the labeling levels of Dye 1 and Dye 2 correlated with the increase in spine size on a spine-by-spine basis (**Figure 2.1i** and **Figure 2.6e**). These results indicate that Dye2 was a robust proxy for LTP at the single spine level.

We further validated the EPSILON technique via glycine-induced chemical LTP (cLTP) in cultured neurons (Methods)[86]. We saturated the surface HT-GluA1 with Dye 1 (AF_{647}), induced cLTP, and then stained with Dye 2 (JF_{549i}) to label the newly exocytosed HT-GluA1 (**Figure 2.1j-n** and **2.6f, g**). The slope of the plot of Dye 2 vs. Dye 1 in cLTP-treated neurons was 2-fold higher compared to controls (cLTP: 0.15 ± 0.01, n = 47,090 spines; control: 0.076 ± 0.008, n = 32,828 spines, P = 0.0001, **Figure 2.1k** and **m, n**). We also observed a significantly larger fraction of spines highly labeled with Dye 2 in cLTP-treated neurons compared to controls (**Figure 2.1l** and **Figure 2.6f, g**, cLTP: 1,024 of 47,090 spines above threshold (2.2%), n = 44 neurons, 6 dishes; control: 195 of 32,828 spines above threshold (0.6%), n = 54 neurons, 6 dishes; P = 0.043, two-sided Student's t-test). Co-transduction with tetanus toxin light chain (TeTX-LC)[51] blocked the increase in the fitted slope upon cLTP treatment and reduced the fraction of spines above threshold, implying that

both parameters depend on AMPAR exocytosis (**Figure 2.1k-n** and **2.6f, g**, TeTX-LC: slope = 0.086 ± 0.009; 35 of 17,231 spines above threshold (0.2%); *n* = 45 neurons, 6 dishes). This analysis revealed that cLTP induced both an increase in the fraction of spines undergoing AMPAR exocytosis and also an increase in the amount of exocytosis in each spine.

2.3.2 Validation of EPSILON in barrel cortex, *in vivo*

To characterize HT-GluA1 in the live mouse brain, we co-expressed HT-GluA1 and myc-GluA2 in layer 2/3 neurons in mouse barrel cortex via *in utero* electroporation (IUE) (**Figure 2.2a**). As in prior experiments with SEP-GluA1, we used a 1:1 ratio of HT-GluA1 and myc-GluA2 to maintain the endogenous subunit stoichiometry[24]. In some experiments, we co-expressed a membrane marker, GPI-eGFP, and verified that HT-GluA1 was well trafficked at morphologically defined spines (**Figure 2.2a**). In separate experiments, we co-expressed a spine marker, PSD95.FingR-eGFP, and verified HT-GluA1 co-localization with molecularly defined spines (**Figure 2.7a-g**). In acute brain slices, patch clamp recordings with extracellular stimulation of excitatory synaptic inputs showed that HT-GluA1/myc-GluA2 expression did not significantly alter AMPAR-mediated excitatory post-synaptic currents (EPSCs) or the AMPAR/NMDAR ratio (**Figure 2.2b-e**). Current-clamp experiments confirmed that HT-GluA1/myc-GluA2 expression also did not significantly alter membrane resistance, membrane capacitance, resting potential, rheobase, or excitability (**Figure**

2.7h, i). The expression of HT-GluA1/myc-GluA2 also did not change the density of spines on dendrites (**Figure 2.7j, k**) or the total GluA1 expression level as assessed by anti-GluA1 antibody staining (**Figure 2.7l, m**).

To quantify basal turnover of AMPARs (i.e. replacement of surface-exposed molecules with fresh ones from vesicles), we performed pulse-chase labeling of surface HT-GluA1 in the barrel cortex *in vivo* (**Figure 2.2f** and **2.8a, b**, Methods). We first verified by GFAP staining that repeated dye injections did not activate an inflammatory response (**Figure 2.8c**). We then saturated preexisting surface HT-GluA1 by intracortical injection of Dye 1 (1.4 mL of 1 mM AF_{647}, Extended Data **Figure 2.8d, e**). After 20 min—enough time for Dye 1 to react—we injected Dye 2 (1.4 mL of 10 mM JF_{549i}) at the same sites with ten-fold higher concentration to ensure that most new HT-GluA1 was labeled with Dye 2 and not residual Dye 1. The mice were returned to their home cage, except for those with an inter-injection delay of 0.3 hours, and after a variable delay, we injected Dye 2 again to ensure complete labeling of newly surface-exposed HT-GluA1. Confocal images of fixed brain sections mapped both dyes throughout $1.2 – 4.6 \times 10^5$ spines in 3 mice at each time-point (**Figure 2.2g**), and the fluorescence intensities were quantified for each spine (**Figure 2.2h**). The half-life for surface HT-GluA1 on spines *in vivo* was approximately 50 hours (**Figure 2.2i**). The disparity in surface lifetime between culture (30 min) and *in vivo* (50 h) is consistent with prior reports which showed an

Figure 2.2 ***(following page)*****: EPSILON reports sensory-induced AMPAR exocytosis** ***in vivo*****. (a)** HT-GluA1 expression in mouse barrel cortex layer 2/3 pyramidal neurons (fixed slice). Top left: coronal section. Arrowheads: barrel cortex. Bottom left: HT-GluA1-expressing neurons. Right: dendrite co-expressing eGFP (cyan) and HT-GluA1 (AF_{647}-HTL, magenta). Scale bars: 500 μm (top left), 200 μm (bottom left), 10 μm (right). **(b)** AMPAR and NMDAR components of EPSCs in layer 2/3 pyramidal neurons. **(c)** AMPAR-mediated EPSCs with varying stimulus intensities. **(d)** AMPAR/NMDAR ratio in HT-GluA1-expressing and control neurons (n = 10 neurons/group). Box plot shows extrema, 25th and 75th percentiles and median. Two-sided Wilcoxon rank-sum test. **(e)** AMPAR EPSC amplitude vs. electric field stimulus strength (n = 10 neurons/group). Error bars: mean ± s.e.m. **(f)** EPSILON pulse-chase scheme for mapping turnover of surface AMPARs *in vivo*. **(g)** HT-GluA1 in layer 2/3 barrel cortex at 0.3, 48, and 168 hours after the first chase. Green: Dye 1 (AF_{647}), magenta: Dye 2 (JF_{549i}). Scale bar: 200 μm. **(h)** Spine fluorescence scatterplots at intervals after the first chase (n = 3 mice/interval; total spines: 0.3 h = 312,246, 3 h = 164,403, 24 h = 458,181, 48 h = 340,927, 96 h = 26,765, 168 h = 121,503). **(i)** Slopes from **(h)** via least-squares regression. Red-shaded error band: mean slope ± 95% confidence interval. **(j)** EPSILON scheme for sensory-evoked AMPAR exocytosis. **(k)** Spines labeled during whisker stimulation. Left: preexisting (Dye 1, JF_{549i}); Middle: newly exocytosed (Dye 2, AF_{488}); Right: merge. Scale bar: 5 μm. **(l)** Density plot of spine fluorescence in control mice (n = 117,829 spines, 3 mice) and **(m)** in whisker-stimulated mice (n = 203,787 spines, 4 mice). Dashed lines: thresholds (see Methods). **(n)** Fraction of spines above Dye 2 intensity threshold (control: n = 3 mice; stimulated: 4 mice). Each data point indicates one mouse. Error bars: mean ± s.e.m. Parts of (f) and (j) were created using Biorender and are used with permission.

Figure 2.3: (Continued)

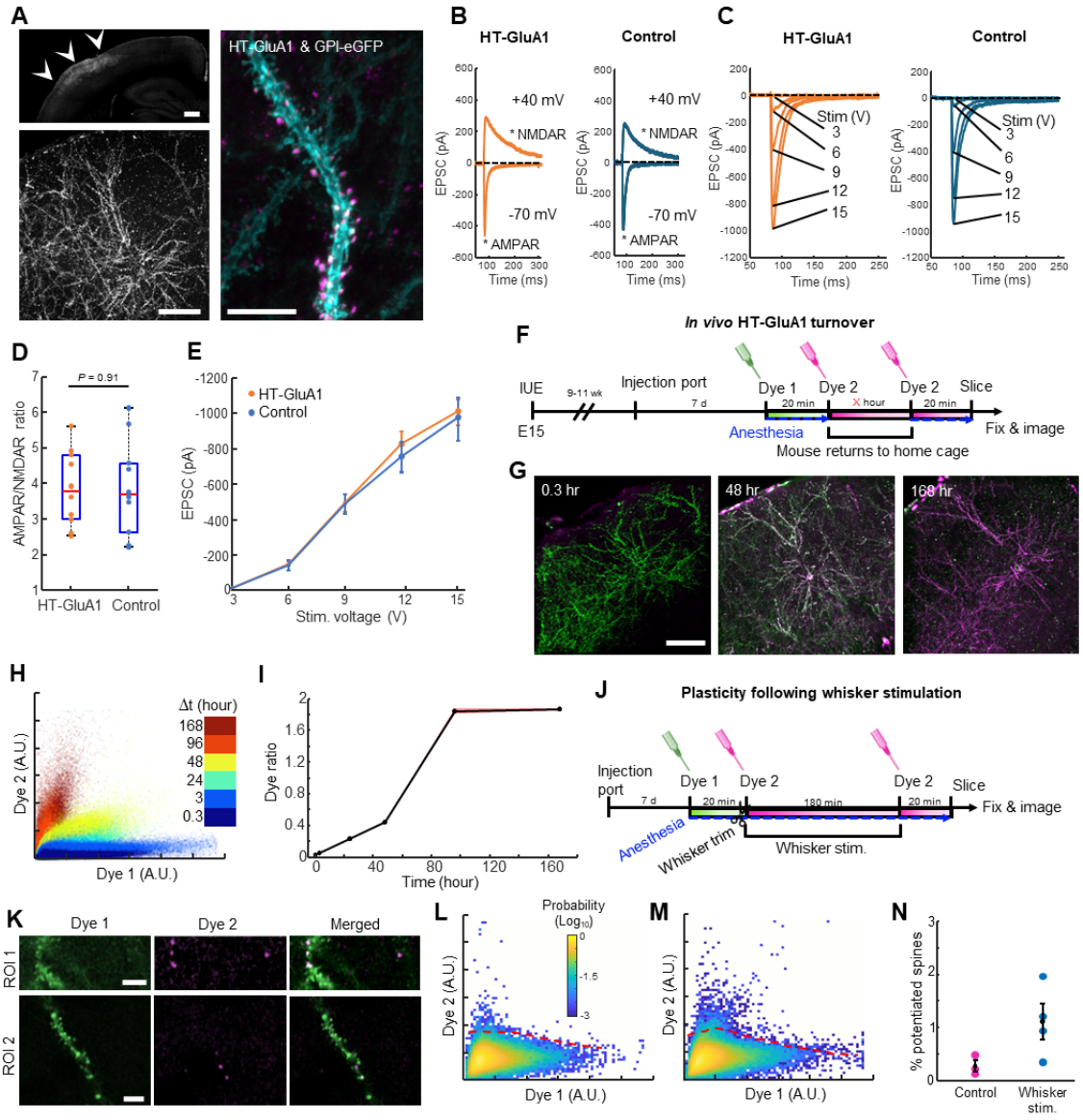

acceleration of GluA1 protein turnover in slice cultures vs. *in vivo*[87,88]. Pulse-chase experiments on timescales shorter than ~50 h could thus identify spines with accelerated AMPAR exocytosis. We also validated that the background autofluorescence and residual dyes contributed negligible fluorescence signal (**Figure 2.8f, g**, Methods).

The adult barrel cortex exhibits synaptic plasticity in response to changes in sensory experience, such as stimulation or deprivation of a subset of whiskers[24,89]. To tag spines with elevated GluA1 exocytosis upon acute sensory stimulation, we performed EPSILON labeling while stimulating a subset of whiskers in an anesthetized mouse (**Figure 2.2j** and **2.8b**, Methods). Confocal images of L2/3 pyramidal neurons in fixed brain sections from the contralateral barrel cortex displayed spines with elevated Dye 2 (AF_{488}), indicative of newly surface-exposed HT-GluA1 (**Figure 2.2k**). Mice subjected to whisker stimulation had a larger fraction of spines with elevated Dye 2 compared to controls (whisker stimulated: 1.1 ± 0.34%, mean ± s.e.m. over 4 mice [n = 203,787 spines]; control: 0.27 ± 0.11%, over 3 mice [n = 117,829 spines]; **Figure 2.2l-n**, Methods). These findings demonstrate that pulse-chase HT-GluA1 AMPAR labeling can tag individual spines that undergo elevated AMPAR exocytosis *in vivo*.

2.3.3 Hippocampal plasticity and cFos in fear conditioning

The CA1 region of the hippocampus is involved in formation and storage of context-

related memories[90], but the physical nature of the hippocampal engram, or memory trace, remains unclear. On one hand, activation of subsets of hippocampal cells, termed engram neurons, is necessary and sufficient to recreate simple conditioned responses (e.g., freezing after contextual fear conditioning)[91]. These cells are often identified using expression of immediate early genes (e.g., *FOS*)[92]. On the other hand, modulation of synaptic strength is also necessary for memory formation[93]. The relation between synapse-level and cell-level memory encodings is unclear[94].

We used HT-GluA1 to investigate the relation between AMPAR exocytosis and cFos expression in hippocampal CA1 pyramidal cells upon contextual fear conditioning (CFC). We expressed HT-GluA1/myc-GluA2 via IUE in hippocampal CA1 pyramidal neurons (Methods). As in the cortex, HT-GluA1 localized to dendritic spines (**Figure 2.3a**). We then used EPSILON tagging followed by fixed slice imaging to map newly exocytosed AMPARs in mice that underwent CFC, home cage control mice, and mice that were exposed to the context but not the conditioned stimulus (foot shock) (**Figure 2.3b**, **2.8b**, and **2.9a**)[95]. For each pyramidal neuron expressing HT-GluA1, we located every spine and quantified the fluorescence of Dye 1 and Dye 2 (Methods). We also quantified endogenous cFos in the nucleus via immunofluorescence in a third spectral channel (**Figure 2.9b-e**).

As in the barrel cortex, a subset of spines had elevated Dye 2 (JF_{549i}) fluorescence, indicative of AMPAR exocytosis (**Figure 2.3c, d**). We quantified the fraction of spines with elevated Dye 2 for each neuron (**Figure 2.3e-h**). The mean

fractions of potentiated spines per neuron were not significantly different between the CFC and context-only groups, but both groups were significantly higher than in the home cage control group (CFC: 1.6 ± 0.27%, mean ± s.e.m., n = 75,200 spines, 19 cells, 4 mice; context-only: 0.94 ± 0.09%, n = 100,534 spines, 23 cells, 6 mice; home cage control: 0.36 ± 0.06%, n = 43,659 spines, 12 cells, 3 mice; **Figure 2.3i**). In the CFC mice, a subset of neurons had an elevated fraction of potentiated spines compared to context-only controls (7 of 19 neurons in CFC mice had a higher fraction of potentiated spines than all 23 neurons from context-only controls, **Figure 2.3i**). Furthermore, the Dye 2 fluorescence in potentiated spines in the CFC group was brighter than in either the home cage control or the context-only group (CFC: 1,000 ± 35 counts, mean ± s.e.m., *n* = 1,016 spines from 19 cells, 4 mice; context-only: 906 ± 35 counts, *n* = 811 spines from 22 cells, 4 mice, *P* = 0.0075; home cage control: 789 ± 36 counts, *n* = 215 spines from 12 cells, 3 mice, *P* = 0.002; **Figure 2.3j**). Finally, within the CFC group, the level of Dye 2 in potentiated spines correlated with the fraction of potentiated spines on a cell-by-cell basis (*R* = 0.48, *P* = 0.04; **Figure 2.10a**). These results imply that the conditioned stimulus elevated the percentage of potentiated spines and the degree of AMPAR exocytosis in a subset of neurons.

We next compared AMPAR exocytosis and cFos expression at the level of individual cells (**Figure 2.3k-o** and **2.10b**). Mice exposed to CFC had more cFos expression compared to either context-only or home cage controls (CFC: cFos level

Figure 2.3 ***(following page)*****: Contextual fear conditioning evokes correlated changes in AMPAR exocytosis and cFos expression. (a)** HT-GluA1 expression in mouse hippocampus CA1 pyramidal neurons (fixed slice). Top left: coronal section. Bottom left: HT-GluA1-expressing single neuron. Right: dendrites co-expressing membrane-localized eGFP (cyan) and HT-GluA1 (AF_{647}-HTL, magenta). Scale bars: 200 μm (top left, bottom left), 5 μm (right). **(b)** EPSILON scheme for tagging spines potentiated during CFC. IHC, immunohistochemistry. **(c)** CA1 neuron after EPSILON tagging, CFC, and cFos immunostaining. Preexisting HT-GluA1 (green) and cFos (cyan). Scale bar: 200 μm. **(d)** Insets from **(c)** showing preexisting HT-GluA1 (Dye 1, AF_{647}) and newly exposed HT-GluA1 (Dye 2, JF_{549i}). Scale bar: 10 μm. **(e-g)** Density plots of spine fluorescence in **(e)** home cage control, **(f)** context-only, and **(g)** CFC animals. Thresholds indicated with dashed lines (Methods). Home cage control: n = 43,659 spines, 3 mice; context-only: 100,534 spines, 6 mice; CFC: 75,200 spines, 4 mice. **(h)** Map of spines with Dye 2/Dye 1 above threshold. Scale bar: 200 μm. **(i)** Percentage of spines above Dye 2 threshold. Home cage: n = 12 cells, 3 mice; context-only: 23 cells, 6 mice; CFC: 19 cells, 4 mice. Error bars: mean ± s.e.m.; two-sided Wilcoxon rank-sum test. Distinct mice indicated by different shape symbols. **(j)** Dye 2 intensity in potentiated spines. Home cage: n = 215 potentiated spines, 12 cells, 3 mice; context-only: 811 potentiated spines, 22 cells, 6 mice, CFC: 1,016 potentiated spines, 19 cells, 4 mice. Box plot shows extrema, 25th and 75th percentiles and median. Distinct mice indicated with marker shape and distinct cells by marker color. **(k, l)** CA1 neurons expressing HT-GluA1 (green) with **(k)** high or **(l)** low cFos expression (cyan). Scale bars: 10 μm. **(m)** cFos intensity distributions: no exposure (2,285 cells, 3 mice), home cage (1,922 cells, 3 mice), context-only (6,407 cells, 6 mice), CFC (7,208 cells, 4 mice). **(n, o)** Cell-by-cell correlation between cFos intensity and fraction of spines with high HT-GluA1 exocytosis: **(n)** home cage (12 cells, 3 mice), context-only (23 cells, 6 mice); **(o)** CFC (19 cells, 4 mice). R, Pearson correlation; P, two-sided Student's t-test. Part of (b) was created using Biorender and is used with permission.

Figure 2.3: (Continued)

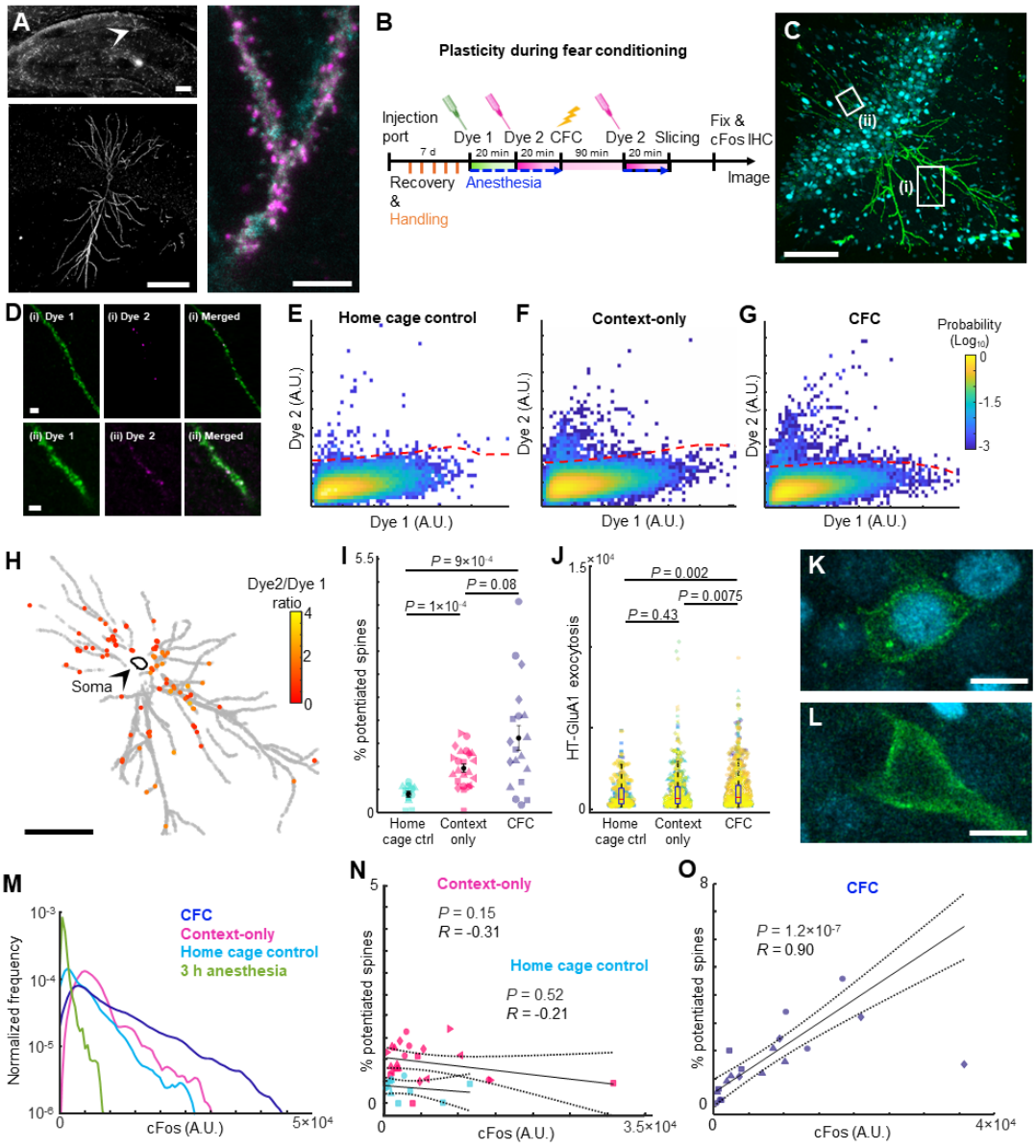

$1.1\times10^4 \pm 1.1\times10^2$ A.U., mean ± s.e.m., n = 7,208 cells, 4 mice; context-only: $6.7\times10^3 \pm 94$ A.U., n = 6,407 cells, 6 mice; home cage control: $5.8\times10^3 \pm 1.3\times10^2$ A.U., n = 1,922 cells, 3 mice; **Figure 2.3m** and **2.9b-e**), consistent with previous reports[96]. We plotted the fraction of spines with high AMPAR exocytosis as a function of the cFos expression, cell by cell. These two quantities were highly correlated within the CFC group (R = 0.90, P < 0.0001), but not in the context-only group, nor in the home cage control group (**Figure 2.3n, o**). To rule out imaging artifacts, we verified that the fraction of potentiated spines, the cFos intensity, and the total number of detected spines were independent of the imaging depth below the slice surface in either the CFC or context-only groups (**Figure 2.10c-e**). Moreover, the total number of spines (labeled with Dye 1) did not correlate with cFos intensity (**Figure 2.10f**). Together, these results establish that during the formation of associative memory, CA1 neurons with higher activity (as reported by cFos) exhibited higher AMPAR exocytosis compared to low-cFos neurons from the same animal.

2.3.4 Mapping sub-cellular patterns of plasticity

We then analyzed the sub-cellular distributions of spines with high AMPAR exocytosis. We segmented the dendrites and registered all spines to their corresponding dendrites (**Figure 2.11a, b**). AMPAR exocytosis was more prevalent in perisomatic than in distal spines (**Figure 2.4a** and **2.11c-i**), with a bias toward

basal over apical dendrites (**Figure 2.4b** and **2.12a-d**). We did not observe any difference in the spatial distribution of AMPAR exocytosis between CFC vs control mice, nor between high and low cFos expressing cells within each experimental group (**Figure 2.12e-g**).

We next sought to assess whether individual dendritic segments had either an excess or deficit in number of potentiated spines. To remove the overall dependence of exocytosis on distance from the soma, we compared dendrites of equal branch order. Within each neuron and each branch order, we quantified the number of potentiated spines, n_i, and the total number of spines, a_i, in each dendritic segment i. We also calculated the total number of potentiated spines, N, and all spines, A, at the corresponding branch order. If potentiated spines were allocated randomly, one would expect $n_i/N \approx a_i/A$. We performed a stochastic simulation to estimate the distribution of expected $\hat{n}_i$, $P(\hat{n}_i)$, under the random allocation hypothesis for each segment and compared to our data. Compared to the simulated random allocation, the data contained an excess of segments with zero potentiated spines, and an excess of segments with more-than-expected potentiated spines (**Figure 2.4c**). These findings point to the presence of "silent" segments (with respect to plasticity), as well as a dendrite-level clustering of plasticity.

Finally, we examined whether potentiated spines showed fine-scale clustering within individual dendritic segments. For each neuron, we calculated the inter-spine contour distance between all pairs of spines. The pairwise distance distribution

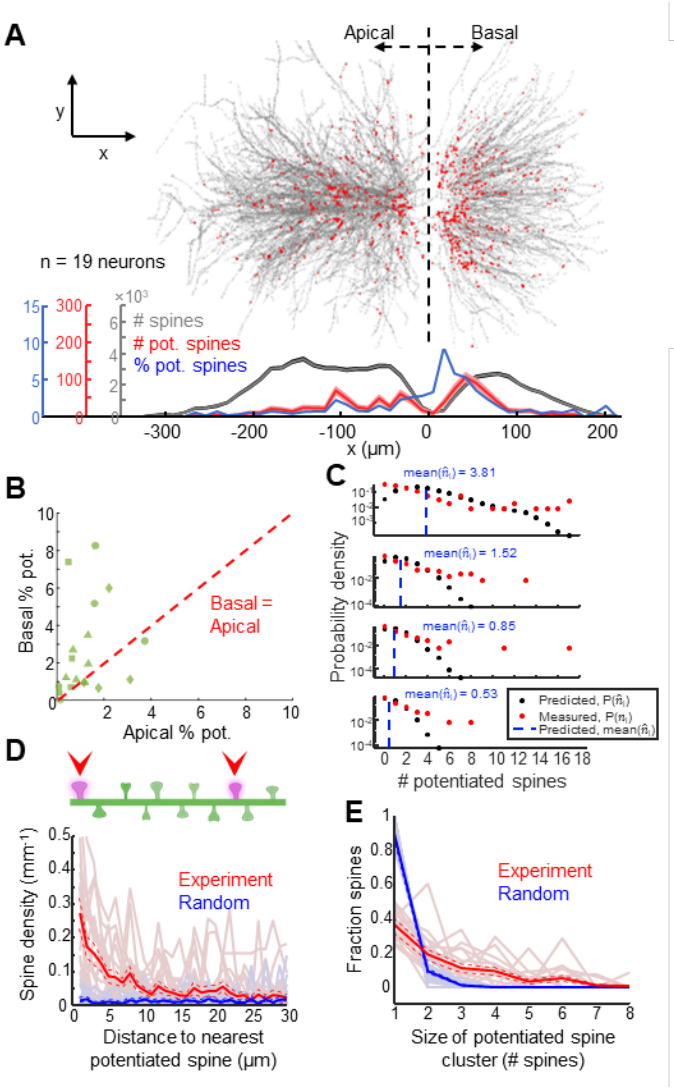

Figure 2.4: Sub-cellular distribution of AMPAR exocytosis after CFC in CA1 pyramidal neurons. (a) Distribution of spines with high HT-GluA1 exocytosis as a function of distance from the *stratum pyramidale*. (Top) Overlapped images of all identified spines (grey) and spines with high HT-GluA1 exocytosis (red). (Bottom) Density profiles of all spines (grey), potentiated spines (red), and fraction of potentiated spines (blue). Shading represents count ± sqrt(count). **(b)** Fraction of potentiated spines in basal vs. apical dendrites in neurons. **(c)** Distributions of the measured (n_i) and predicted ($\hat{n}_i$) number of potentiated spines in individual dendrite segments from the CFC group (n = 1476 dendrite segments, 19 neurons). $P(\hat{n}_i)$ was evaluated from 500 random allocations of potentiated spines among dendrites of a given branch order within each cell. The plots show distributions for groups of dendritic segments with similar $\langle \hat{n}_i \rangle$ (regardless of branch order) and sorted by decreasing mean $\hat{n}_i$ from top to bottom. **(d)** Density profile of potentiated spines as a function of distance from the nearest potentiated spine. The single-cell profiles are plotted with light colors. Bold and dashed lines represent mean ± s.e.m. Random: simulation where the same number of potentiated spines were distributed randomly and independently among all detected spines. **(e)** Fraction of potentiated spine clusters of different sizes. The single-cell profiles are plotted with light colors. Bold and dashed lines represent mean ± s.e.m. Random defined as in **(d)**. All data from n = 19 neurons, 4 mice, subjected to CFC. Part of (d) was created using Biorender and is used with permission.

between potentiated spines showed a decay with a length constant of 8.0 mm (95% confidence interval [6.5 10]). In a simulation where we took the same number of potentiated spines and distributed them randomly and independently among all spines, the corresponding distribution for randomly selected spines was flat (**Figure 2.4d** and **2.13a**). We then quantified the distribution of cluster size, i.e. the number of potentiated spines within each cluster (**Figure 2.4e** and **2.13b**, Methods). In CFC-treated mice, potentiated spines were more likely to be in clusters of ≥ 2 spines compared to the simulated random allocation (potentiated: 57 ± 4.3% of spines were in clusters, mean ± s.e.m.; randomly allocated: 7.2 ± 1.5% clustered; $P = 2.0\times10^{-4}$ by Wilcoxon signed-rank test). Clustering of potentiated spines was similar in context-only control mice (context-only: 62 ± 5.0%, mean ± s.e.m.; $P = 0.20$ by two-sided Wilcoxon rank-sum test, **Figure 2.4e** and **2.13b**). These analyses illustrate how pulse-chase HT labeling can map sub-cellular details of synaptic potentiation.

2.4 Discussion

We developed EPSILON, a method to map AMPAR exocytosis with single-synapse resolution during defined time windows *in vitro* and *in vivo*. Pulse-chase HaloTag labeling with membrane-impermeable dyes tags AMPAR exocytosis across large brain regions and in deep brain structures. We validated EPSILON in cultured neurons and demonstrated that AMPAR exocytosis is a robust proxy for synaptic potentiation. During fear conditioning experiments in mice, AMPAR exocytosis

correlated tightly with cFos expression on a cell-by-cell basis in CA1 pyramidal neurons. We observed preferential plasticity in the perisomatic region in these cells, and clustered plasticity at the level of branches and sub-branch regions. These experiments connected synapse-level plasticity to cell-level engram formation.

A longstanding question in the engram field has been to identify the biophysical mechanisms by which cFos-positive engram cells modulate circuit dynamics to encode a memory[94]. Our work shows that cFos expression can serve as a surrogate for total synaptic plasticity. This finding connects the seemingly disparate bodies of work on engram cells and on synaptic encoding of memories. Mice exposed to the same context without aversive stimulus exhibited less AMPAR exocytosis and lower cFos expression. We did not observe a correlation between AMPAR exocytosis and cFos expression in these mice, but this may be a consequence of the low overall cFos expression: there might be a correlation in the subpopulation of neurons with high cFos expression (**Figure 2.3m**), but these neurons were too rare for us to analyze. The differences between the CFC vs. context-only measurements suggest an important role for reinforcement signals in mediating both AMPAR exocytosis and cFos expression.

Building on these observations, we examined the subcellular distributions of synaptic plasticity in engram neurons. Dendrites of CA1 pyramidal neurons receive synaptic inputs from multiple pathways arranged in a laminar distribution. It has been proposed that distal input onto apical dendrites from entorhinal cortex act as an

instructive signal, which modulates plasticity that primarily occurs at the proximal inputs from CA3[97]. Our results are consistent with this picture and further show that under our experimental paradigms there was little potentiation of the distal inputs. Choi *et al.* showed that in CFC-treated mice, synapses between CA3 engram cells and CA1 engram cells were enlarged relative to non-engram neurons,[66] but it was not clear whether this enlargement preceded the CFC treatment or was a consequence of the treatment. We also observed that the distribution of potentiated spines approximately matched the previously reported distribution of CA3 inputs[98], consistent with the observations of Choi *et al.*. Our work further showed that the increase in AMPAR density occurred after the CFC treatment, implying that the CFC treatment induced the synaptic plasticity.

We also observed clustering of synaptic plasticity at the segment level, aligning with previous theoretical predictions and *in vivo* observations[99]. This finding supports the possibility that individual dendrites can serve as units for memory allocation. This dendritic segment-level plasticity may arise from compartmentalized calcium influx, which can initiate post-synaptic signaling pathways associated with LTP[100]. Finally we observed short-range (< 10 mm) clustering of potentiated spines, consistent with prior observations in cultured neurons and in superficial cortex *in vivo*[24,101]. This clustering may originate from either co-activated synapses[102] or from diffusion of small GTPases between nearby spines[103]. Clustered plasticity has been proposed to facilitate local dendritic spike generation[81].

There are several possible extensions of the EPSILON technique. First, one could use three or more dyes to map AMPAR exocytosis patterns over two or more epochs (e.g. during distinct memory encodings). This approach could highlight overlap in synaptic-level memory networks; or reveal temporal correlations in AMPAR exocytosis rates. Second, one could use *in vivo* real-time imaging (**Figure 2.14a, b**) to track independently the synaptic concentrations of AMPARs labeled with Dye 1 and Dye 2 (**Figure 2.1h** and **2.6d**). This would reveal the relative timing and importance of lateral AMPAR recruitment vs exocytosis in synaptic plasticity. For this application, use of a fluorogenic Dye 2 would minimize background from unreacted dye. Third, one could analyze the data to locate spines containing only Dye 2, and not Dye 1, as a marker of new spine formation (**Figure 2.14c**). Fourth, one could use a membrane-permeable Dye 2 or Dye 3. This would relate the population of surface AMPARs to the reservoir of intracellular AMPARs.

AMPAR exocytosis is only one of many biological mechanisms involved in synaptic plasticity, and the relative contributions of different mechanisms across cell types and across stages of plasticity is not fully understood. For example, synaptic weight changes can occur through lateral capture of extrasynaptic AMPARs[50], through post-translational modifications[104], and through changes of subunit stoichiometry[105]. Several experiments have used knockouts of postsynaptic vesicle fusion machinery to block plasticity-related AMPAR exocytosis, but there has been controversy over which types of memory formation require AMPAR exocytosis.[106–

[108] To address this issue, it will be useful to monitor AMPAR exocytosis and postsynaptic voltage or calcium concurrently, during learning tasks.

A further limitation of EPSILON is that under basal conditions, AMPARs turn over in the synapse with a half-life of ~50 h (**Figure 2.2h, i**). EPSILON experiments can only reliably probe plasticity-related exocytosis on shorter timescales. We restricted plasticity-related pulse-chase intervals to < 4 h. It is not known whether there are synapses in which elevated AMPAR exocytosis is counterbalanced by elevated endocytosis; such synapses would bind Dye 2 in an EPSILON assay but may not be potentiated. It will be beneficial to develop techniques to monitor AMPAR endocytosis at the same time as exocytosis. For example, labeling with a membrane-impermeable pH-sensitive Dye 1 could reveal internalization of AMPARs into acidic vesicles.

Our decision to express HT-GluA1 rather than knocking HT into the endogenous *Gria1* locus was motivated by prior reports on SEP-GluA1. Overexpression of SEP-GluA1 in both cultured neurons and *in vivo* did not perturb the neuron's intrinsic or synaptic properties[24] while SEP-GluA1 knock-in decreased GluA1 mRNA and protein expression[109]. Indeed our control measurements found no significant effects of HT-GluA1 expression on intrinsic excitability (**Figure 2.7h, i**), spine density (**Figure 2.7j, k**), total AMPAR level (**Figure 2.5e** and **2.7l, m**), synaptic AMPAR:NMDA current ratio (**Figure 2.2b-e**), or uncaging-induced spine growth (**Figure 2.6a, b**). Nonetheless, future uses of EPSILON may benefit from insertion

of small and readily labeled tags into the endogenous locus via transgenic[109] or CRISPR-based knock-in[80] approaches. A transgenic approach was successfully used to fuse the biotin acceptor peptide (AP) to GluA2, though the reliance on multiple exogenously delivered proteins presented an obstacle for *in vivo* pulse-chase experiments[80].

The EPSILON technique provides complementary information compared to other approaches to monitoring AMPAR dynamics *in vivo*. *In vivo* two-photon microscopy of SEP-GluA1 has been used to observe AMPAR insertion at individual synapses during memory formation[24]. However, despite progress in machine learning-based image analysis,[110] the requirement for high resolution imaging *in vivo* restricts application of SEP-GluA1 to optically accessible brain regions[111]. Further, the requirement for head-fixed real-time imaging constrains the possible behavioral paradigms[112]. The dual-eGRASP technique maps synaptic connections between defined neuronal populations, including under control of activity dependent promoters[66]. This technique separates the *in vivo* recording from the *ex vivo* measurement and so is applicable to deep brain regions, but does not directly probe the strength or timing of plasticity events. The eGRASP technique also requires targeted expression of distinct components in pre- and post-synaptic neurons, and thus does not capture all synapses in a given postsynaptic cell. The SYNPLA technique maps AMPAR density in synapses of genetically defined neurons, but it also lacks the capability to probe changes in synaptic strength during a defined time

window[79]. EPSILON maps AMPAR exocytosis synaptic resolution and within a user-defined time window, and is not constrained by optical access *in vivo*. EPSILON provides a powerful tool for studying synaptic plasticity and has the potential to be extended to other transmembrane proteins.

2.5 Methods

2.5.1 Animals

All experiments were performed on 8-12 week-old male and female C57BL/6 or CD-1 mice purchased from Charles River Laboratories. All animal procedures were in accordance with the US National Institutes of Health *Guide for the Care and Use of Laboratory Animals* and were approved by the Institutional Animal Care and Use Committee (IACUC) at Harvard University.

2.5.2 DNA constructs

Standard methods of molecular cloning were used to create the constructs. The myc-GluA2 plasmid was provided by the Richard Huganir lab at Johns Hopkins University[24]. Plasmids and sequences created for this project are on Addgene or available upon request.

pTL024 (Addgene 192517): Signal sequence-HaloTag-GluA1 (abbreviated HT-GluA1), driven by human synapsin 1 gene (hSynI) promoter.

Plasmid pTL024 was assembled from three fragments: the N terminal signal sequence,

the HaloTag protein, and GluA1. The N terminal signal sequence was amplified from pCI-SEP-GluR1, Addgene 24000. The HaloTag protein was amplified from Voltron, Addgene 119033. GluA1, along with a 15 amino acid linker, was amplified from CAG::SEP-GluA1, a gift of Prof. Richard Huganir[24]. The fragments were assembled together with Gibson Assembly[113] and cloned into pLenti hSynI vector (HT075 from[114]).

pDK034: Tetanus toxin light chain (abbreviated TeTX-LC)-IRES-eGFP, driven by cytomegalovirus (CMV) promoter.

Plasmid pDK034 was assembled from three fragments: TeTX-LC, IRES sequences, and eGFP. TeTX-LC was amplified from pFsynW-TeTx-LC, Addgene 197284. IRES sequences were amplified from FCK_KCC2_IRES_mOrange plasmid (lab stock). eGFP was amplified from CamKII::PSD95.FingR-eGFP-CCR5TC, Addgene 126218. The fragments were assembled together with Gibson Assembly and cloned into pLenti CMV vector (lab stock).

pTL028 (Addgene 192520): Cre-on AAV expression vector of HaloTag fused to the N terminus of GluA1, driven by human synapsin 1 gene (SYN1, usually called hSyn) promoter. The open reading frame of pTL024 was flipped and cloned into a pAAV_hSyn-DIO vector (Addgene 107704).

2.5.3 Synthesis of Alexa Fluor 647-HaloTag ligand (AF_{647}-HTL)

Alexa Fluor 647 NHS ester (5 mg, 4.0 μmol) and HaloTag amine (O2) ligand (1.3 mg, 6.0 μmol, 1.5 eq) were combined in DMF (1 mL), and DIEA (3.5 μL, 20.0 μmol, 5 eq) was

added. The reaction was stirred at room temperature for 18 h while shielded from light. It was subsequently purified by reverse phase HPLC (5–30% MeCN/H_2O, linear gradient, with constant 0.1% v/v TFA additive; 20 min run; 42 mL/min flow; Gemini-NX 5 μm, 30 × 150 mm) to provide 3.2 mg (68%) of the title compound as a blue solid. Analytical HPLC: t_R = 13.9 min, >99% purity (10–50% MeCN/H_2O, linear gradient, with constant 0.1% v/v TFA additive; 20 min run; 1 mL/min flow; Eclipse XDB 5 μm, 4.6 × 150 mm; detection at 650 nm; ESI, positive ion mode); MS (ESI) calculated for $C_{46}H_{67}ClN_3O_{15}S_4$ $[M]^+$ 1064.3, found 1064.1; MS (ESI) calculated for $C_{46}H_{68}ClN_3O_{15}S_4$ $[M+H]^{2+}$ 532.7, found 532.6.

2.5.4 Primary neuron culture

Neuron culture was as previously described[71].

2.5.5 Virus packaging

In-house preparations of lentivirus used a second-generation lentivirus packaging system using HEK293T cells (ATCC, CRL-3216), following the protocol previously described[71]. High-titer HT-GluA1 AAV2/9 virus was generated at the Janelia Vector Core.

2.5.6 Lentiviral transduction of cultured neurons

The hSyn::HT-GluA1 vectors were introduced to the neurons via lentiviral transduction at DIV7 or DIV14. The lentiviral vectors were added directly to the neuronal cultures in

fresh BPNM/SM1 medium. The neuronal cultures were then incubated with the lentivirus-containing medium for 12 hours at 37 °C and 5% CO_2, followed by a medium replacement with lentivirus-free medium. Experiments were conducted after 7 days. Lentiviruses were produced using the same protocol for both CamKII::PSD95.FingR-eGFP-CCR5TC and CMV::TeTX-LC-IRES-eGFP vectors, and the transduction was conducted 3 days after the transduction of hSyn::HT-GluA1.

2.5.7 Manders' overlap coefficients

The Manders' coefficients (M1 and M2) were calculated between two-channels (HT-GluA1 and PSD95) for each neuron as previously described[115] using MATLAB. Briefly, the images in each color channel were binarized with a threshold set by the Otsu algorithm. M1 and M2 were calculated via:

$$M1 = \mathrm{sum}(B_{HT\text{-}GluA1}.*I_{HT\text{-}GluA1}.*B_{PSD\text{-}95})/\mathrm{sum}(B_{HT\text{-}GluA1}.*I_{HT\text{-}GluA1})$$

$$M2 = \mathrm{sum}(B_{PSD\text{-}95}.*I_{PSD\text{-}95}.*B_{HT\text{-}GluA1})/\mathrm{sum}(B_{PSD\text{-}95}.*I_{PSD\text{-}95})$$

where I denotes the original image, B denotes a binary mask obtained with a threshold set by the Otsu algorithm. '.*' is elementwise multiplication.

2.5.8 *In vitro* labeling kinetics

Cultured neurons expressing HT-GluA1 at DIV14 were incubated with 100 nM AF_{488}-HTL or 1μM JF_{549i}-HTL or 1μM AF_{647}-HTL in fresh BPNM/SM1 medium for different

time durations (5 seconds, 30 seconds, 5 minutes, and 30 minutes for 100 nM AF_{488}-HTL; 5 seconds, 10 seconds, 30 seconds, 2 minutes, 5 minutes, and 10 minutes for 1μM JF_{549i}-HTL and 1μM AF_{647}-HTL) at 37°C and 5% CO_2. The neurons were then washed twice with PBS for 1 minute each and fixed with 4% paraformaldehyde. The fixed neuron cultures were then washed in PBS for 24 hours. All media were heated to 37 °C before use.

2.5.9 *In vitro* turnover rate

Cultured neurons expressing HT-GluA1 at DIV14 were incubated with 100 nM AF_{488}-HTL in fresh BPNM/SM1 medium for 5 minutes at 37 °C and 5% CO_2. The neurons were then washed twice with PBS for 1 minute each and the medium was replaced with dye-free medium. To label new surface HT-GluA1, the medium was replaced with 1 μM JF_{549i}-HTL in fresh BPNM/SM1 medium at different time points. After incubating for 5 minutes at 37 °C and 5% CO_2, neurons were washed twice with PBS for 1 minute each and fixed with 4% paraformaldehyde. The fixed neuron cultures were then washed in PBS for 24 hours. All media were heated to 37 °C before use.

2.5.10 MNI-glutamate uncaging

MNI-glutamate uncaging was conducted as previously described[85]. Briefly, live cell imaging of cultured neurons was carried out on an LSM 980 (operated with Zeiss Zen (blue edition)) with 63× oil immersion objective at 34 °C. Neurons were incubated with an

imaging buffer containing 10 mM HEPES, 130 mM NaCl, 5 mM KCl, 30 mM D-glucose, 2 mM CaCl2, 1 mM $MgCl_2$, supplemented with 1 μM TTX for 5 minutes, and then stained with 1 μM Dye 1 (AF_{647}-HTL) for 1 minute in the same buffer. After neurons were washed three times with the imaging buffer without dye, the buffer was changed to the same one without TTX or Mg^{2+}, and supplemented with 1 μM Glycine and 2 mM MNI-glutamate. Z-stack images were acquired in eGFP and Dye 1 channels 1 minute before uncaging pulses were delivered. Spines were focally stimulated to a diffraction-limited spot at 405 nm with 60 uncaging pulses delivered at 1 Hz. To monitor spine growth, z-stack images in the eGFP channel were acquired every 3 minutes starting 1 minute post-uncaging. After 25 minutes post-uncaging, the Mg^{2+}-free buffer was replaced with the standard imaging buffer containing 1 μM Dye 2 (JF_{549i}-HTL), and the neurons were stained for 1 minute. After washing the neurons twice, z-stack images were acquired in eGFP, Dye 1, and Dye 2 channels.

2.5.11 Pulse-chase labeling in cultured neurons during chemical LTP

Cultured neurons expressing HT-GluA1 at DIV21 were washed twice with a stimulation buffer containing 150 mM NaCl, 2 mM $CaCl_2$, 5 mM KCl, 10 mM HEPES, 30 mM D-glucose, 0.5 μM TTX, 20 mM bicuculline, and 1 μM strychnine. The neurons were then exposed to 1 μM Dye 1 (AF_{647}-HTL) in the stimulation buffer at 37°C and 5% CO_2 for 1 minute. The neurons were then washed twice with the stimulation buffer and then incubated in the stimulation buffer supplemented with 0.2 mM glycine and 1 μM Dye 2

(JF_{549i}-HTL) for 10 minutes. The neurons were then washed twice with a washing buffer with the same composition but supplemented with an additional 2 mM $MgCl_2$ and then stained with 1 μM Dye 2 again in the washing buffer for 5 minutes. The neurons were washed twice with the washing buffer and fixed with 4% paraformaldehyde. The fixed neuron cultures were washed in PBS for 24 hours. TeTx-LC co-expressing neurons underwent the same experimental conditions. The negative control cultures were exposed to the stimulation buffer without glycine. All media were pre-incubated with 5% CO_2 for 30 minutes and heated to 37 °C before use.

2.5.12 GluA1 immunohistochemistry in cultured neurons

After the neurons were fixed and washed as described above, the fixed neurons were permeabilized with PBST1 (0.1% Triton-X in PBS) for 10 minutes at room temperature on a shaker. The neurons were then blocked with 1% bovine serum albumin (BSA) in PBST2 (0.1% Tween 20 in PBS) for 30 minutes on a shaker. The neurons were incubated with a mouse anti-GluA1-CTD (c-terminal domain) primary antibody (1:500 dilution in 1% BSA in PBST2, Synaptic Systems, 182 011) for 1 h at room temperature on a shaker. Neurons were then washed in PBST2 for 5 min (x3), followed by 1 h incubation with secondary antibody (1:500 in 1% BSA in PBST2; AF_{647} goat anti-mouse, Abcam, A-150115) at room temperature. After two additional 5-minute washes and one 24 h wash in PBS at room temperature, the neurons were imaged on a confocal microscope.

2.5.13 *In utero* electroporation

Progenitor cells in layer 2/3 of the embryonic mouse brain were transfected using *in utero* electroporation. Pregnant CD-1 mice were used and DNA solution containing Fast Green was injected into the lateral ventricle of each embryo through a pulled-glass pipette. Electric pulses were applied using 5-mm Pt electrodes. The angle of electrodes was adjusted to target the specified brain region (barrel cortex or hippocampal CA1). The electroporation protocol comprised five pulses of 35 V, with a frequency of 1 Hz and a duration of 50 ms. The DNA solution used contained HT-GluA1, myc-GluA2 at a ratio of 1:1 (final concentration: 2 μg/μL each). For the co-expression with GPI-eGFP or PSD95.FingR-eGFP, the DNA solution contained HT-GluA1, myc-GluA2, and GPI-eGFP or PSD95.FingR-eGFP at a ratio of 2:2:1 (final concentration: 2 μg/μL for HT-GluA1 and myc-GluA2; 1 μg/μL for GPI-GFP or PSD95.FingR-eGFP).

2.5.14 Patch-clamp electrophysiology

Coronal brain slices (300 μm) were prepared from CD-1 mice of either sex between postnatal days P14 and P16. IUE was used for HT-GluA1 expression in cortical layer 2/3 neurons. Standard whole-cell recording was performed at 34 °C during a continuous perfusion at 2 ml min^{-1}. The perfusion buffer contained 124 mM NaCl, 3 mM KCl, 26 mM $NaHCO_3$, 1.25 mM NaH_2PO_4, 2 mM $MgCl_2$, 15 mM D-glucose, and 2 mM $CaCl_2$ (saturated with 95% O_2 and 5% CO_2). Cortical layer 2/3 neurons were visualized using a

custom-built upright microscope. The whole-cell internal solution contained 8 mM NaCl, 130 mM $KMeSO_3$, 10 mM HEPES, 5 mM KCl, 0.5 mM EGTA, 4 mM Mg-ATP, 0.3 mM Na_3-GTP. The pH was adjusted to 7.2–7.3 with KOH and osmolarity was set to 290–295 mOsm l^{-1}. Borosilicate glass pipettes were used with a resistance of 3-5 MΩ (1B150F-4; WPI). Patch clamp recordings were acquired and filtered at 10 kHz with the internal Bessel filter using a Multiclamp 700B (Molecular Devices) and digitized with PCIe-6323 (National Instruments) at 100 kHz. Following the whole-cell configuration, membrane capacitance (C_m), and membrane resistance (R_m) were estimated under voltage clamp mode. Resting membrane potential, rheobase, and spike rates were measured under current clamp mode. Rheobase was defined as the minimum current step (in 500 ms duration) required to trigger at least one spike. Whole-cell recordings were monitored and analyzed in MATLAB.

To measure evoked EPSCs, voltage-clamp experiments were performed with a stimulating electrode (CBAPB50, FHC) placed 100-200 μm laterally to activate layer 2/3 inputs. Holding potential was -70 mV. The whole-cell internal solution contained (in mM) 8 NaCl, 130 $CsMeSO_3$, 10 HEPES, 0.5 EGTA, 4 Mg-ATP, 0.3 Na_3-GTP, 5 QX-314, 0.1 spermine. The pH was adjusted to 7.2-7.3 with CsOH and osmolarity was set to 290-295 mOsm l^{-1}. The perfusion buffer contained 50 μM picrotoxin (Thermo Scientific) and 10 μM (+)-bicuculline (Enzo Life Sciences) to prevent $GABA_A$ receptor-mediated transmission. After a stable baseline of at least 5 min, the input-output relationships were estimated by varying the stimulus intensity from 3 to 15 V in 3 V increments (0.1 ms

duration). Stimulation frequency was 0.1 Hz. For measuring the AMPAR/NMDAR ratio, cells were clamped at a holding potential of -70 mV to measure the peak of AMPAR-mediated synaptic transmission. NMDAR-mediated currents were estimated at 75 ms after the stimulus onset at a holding potential of +40 mV. Example traces were an average of 5 consecutive responses, collected from typical experiments (stimulus artifacts were blanked for clarity). Experiments were accepted for analysis if series resistance values were < 20 MΩ and varied by <15% throughout the experiment.

2.5.15 Cranial window surgery and stereotaxic intracranial AAV injection

CD-1 mice aged 8-10 weeks were given a ketamine/dexmedetomidine (77 mg/kg and 0.33 mg/kg, respectively) solution for anesthesia and were positioned in a stereotaxic apparatus. A craniotomy of approximately 3 mm was created on the left barrel cortex of the exposed skull (AP: 3.3-3.4 mm lateral, 1.6 mm anterior of lambda) with a dental drill. The HT-GluA1 and CamKII-Cre AAV2/9 viruses were diluted to a final titer of $1x10^{13}$ and $1x10^{11}$ GC/ml, respectively. The diluted virus was injected at 5 sites across the craniotomy (80 and 160 μm beneath the dura; 40-60 nL at each depth; 30-60 nL/min). Following the virus injection, a glass window was placed over the craniotomy and fixed to the skull using silicone gel (KWIK-CAST silicone sealant, WPI). Then, a titanium headplate was attached to the exposed skull using dental cement (C&B metabond, Parkell, No. 242-3200). After the mice recovered from anesthesia, they were returned to their home cages, and carprofen (5 mg/kg) and buprenorphine (0.1 mg/kg) were administered

on post-surgery Day 0, 1, and 2. The designs of the cranial window and the titanium headplate used in this experiment were based on previously published protocols[114,116].

2.5.16 Intracortical dye injection for two-photon imaging

One week after the cranial window surgery, the mice were brought back to the surgical stage and put under <2% isoflurane anesthesia. The anesthesia was maintained at 1% isoflurane throughout the surgery. The window was removed carefully along with the silicone gel, and the dura was carefully removed based on previously published protocols[116]. Then, 1 mM of AF_{488}-HTL was injected at three different sites across the craniotomy, with a rate of 100 nL/min (80 nL at each depth, with 0.1 mm increments from 0.5 mm to 0 mm beneath the cortical surface). After dye injection, a new window was placed over the craniotomy and attached to the skull with silicone gel. The animals were then moved to the *in vivo* imaging setup, and the two-photon imaging session was started 20 minutes after the dye injection had ended.

2.5.17 *In vivo* two-photon imaging

Live images were obtained from mice that had undergone cranial window surgery and intracortical dye injection while under anesthesia with isoflurane (1% vol isoflurane/vol O_2) using a custom two-photon laser-scanning microscope controlled by custom LabView code described previously[117]. Throughout the imaging session, the animal was kept anesthetized with a dose of 1-1.5% isoflurane, adjusted to maintain a stable breathing rate.

The mouse was kept warm using a heating pad (WPI, ATC2000) to maintain a stable body temperature of 37 °C, and ophthalmic eye ointment was applied to both eyes to keep them moist. HT-GluA1 stained with AF_{488}-HTL was excited at 910 nm using a Ti:sapphire laser (Coherent) beam delivered to the back-aperture of the objective. AF_{488} fluorescence was filtered by a band-pass emission filter (Unice, FF-3-525/50-25) and delivered onto a photomultiplier tube (Hamamatsu). Image stacks were acquired with a voxel size of 0.18 µm in x and y and a dwell time of 200 µs. The z-step was 1 µm. Images shown in figures were gaussian filtered to remove speckle noise. The imaging session lasted < 1 h.

2.5.18 Installation of dye injection port

Male or female CD-1 mice expressing HT-GluA1 via *in utero* electroporation were selected at age 9-11 weeks and anesthetized using a ketamine/dexmedetomidine solution. To maintain body temperature at 36-37 °C, a heating pad (WPI, ATC2000) was placed under the mouse, and ophthalmic eye ointment was applied to the mouse's eyes to keep them moist. Surgical coordinates were identified as indicated in **Figure 2.8a, b**, and a hollow titanium ring with an outer diameter of 5 mm, an inner diameter of 2.1 mm, and a thickness of 0.35 mm was attached to the skull surrounding the target coordinates with dental cement (C&B metabond, Parkell, No. 242-3200). Holes were drilled through the skull until only a very thin layer of the skull (~20 mm) remained and the titanium ring was filled with silicone gel which was removed before dye injection and refilled after injection. The mice were returned to their home cages after recovering from anesthesia.

2.5.19 *In vivo* turnover rate measurement

One week after installation of the injection port at the barrel cortex, mice (age 10-12 weeks) were anesthetized with isoflurane and placed on a surgical platform. At every indicated injection point in **Figure2.8a**, 80 nL of AF_{647}-HTL (1 μM) was injected at a rate of 100 nL/min. Then, 80 nL of JF_{549i}-HTL (10 μM) was injected at the same points 20 minutes after the AF_{647}-HTL injection, also at the same rate. After 20 minutes from the end of the dye injection, the mice were returned to their home cages. Later, at different timepoints, the mice underwent the second JF_{549i}-HTL injection. At the same injection points as previously described, 80 nL of JF_{549i}-HTL (10 μM) was injected at the same rate. After 20 minutes from the end of the dye injection, the mice were euthanized and prepared for brain slicing.

2.5.20 Acute whisker stimulation with pulse-chase labeling

Whisker stimulation sessions were conducted one week after injection port installation. On the day of stimulation, 2.7 mg/kg of chlorprothixene hydrochloride dissolved in PBS was intraperitoneally injected before anesthetic induction. Mice (10-12 weeks) were anesthetized with isoflurane on the surgical platform and injected at each point shown in **Figure2.8a** with JF_{549i}-HTL (80 nL, 1 μM) at a rate of 100 nL/min. After 20 minutes, AF_{488}-HTL (80 nL, 10 μM) was injected at the same points. After another 20 minutes from the end of dye injection, the contralateral whiskers were trimmed in a chessboard

pattern[89,118,119]. Spared whiskers were deflected at 10 Hz for 180 minutes with a rotary whisker stimulator. Mice in the control group were placed under the same experimental conditions, but all contralateral whiskers were trimmed. During whisker stimulation, isoflurane level was kept at ~0.5% to maintain shallow anesthesia. After whisker stimulation, the mice underwent the second injection of AF_{488}-HTL (80 nL, 10 μM) as previously described. After 20 minutes from the end of the dye injection, the mice were euthanized and prepared for brain slicing.

2.5.21 Slice preparation for confocal imaging

Mice were overdosed with isoflurane until their breathing ceased. Their brains were then promptly extracted. The brains were sliced into 300 μm coronal sections using a vibratome (Leica, VT1200S) and then fixed in 4% paraformaldehyde for 24 hours at 4 °C. The fixed slices were additionally washed in PBS for 48 hours on a shaker at room temperature. The slices were mounted (VECTASHIELD PLUS Antifade Mounting Medium, Vectorlabs, H-1900-10) to be imaged on confocal imaging systems.

2.5.22 Contextual fear conditioning with pulse-chase labeling

In the five days prior to CFC treatment, each mouse was housed alone and habituated to the investigator and anesthesia chamber without isoflurane. On the day of conditioning, the mouse (age 10-12 weeks) was anesthetized for 3 hours with 1.0% isoflurane on the surgical platform and injected with AF_{647}-HTL (80 nL, 1 μM) at a rate of 100 nL/min at

every injection point shown in **Figure2.8b**. After 20 min, JF_{549i}-HTL (80 nL, 10 μM) was injected at the same points. The mouse was then returned to its home cage to recover from anesthesia. After 20 minutes, the mouse underwent conditioning sessions that lasted 300 s. For the first 150 s, the mouse was allowed to explore the conditioning chamber freely. Starting at 150 s and repeating every 30 s for a total of five shocks, the mouse was given 0.7 mA foot shocks of 2-second duration. Mice in the context-only group were placed in the same chamber for 300 seconds without any shocks. Mice in the home cage control group remained in their home cage. After 90 minutes from the end of the conditioning session, the mouse was anesthetized with isoflurane on the surgical platform for the second JF_{549i}-HTL injection. 80 nL of JF_{549i}-HTL (10 μM) was injected into the injection points at the same points and rate as previously described. After 20 minutes from the end of the dye injection, the mouse was euthanized and prepared for brain slicing.

For the experiments in **Figure2.9a**, the same conditioning sessions (with and without shocks) were conducted, except the dye injection steps were skipped. 1 day after conditioning, mice were exposed to the same context and their freezing (absence of movement except for respiration[95]) levels were measured via video analysis of the first 180 seconds from re-exposure. Animal motion was tracked using MATLAB code. Briefly, the center of mass of the mouse was tracked for every frame using the regionprops function. Then, the mouse's speed was calculated between each frame, and the time duration during which the speed was slower than 0.03 m/s was counted as freezing time, taking into account the movement of the center of mass during breathing

and system vibrations.

2.5.23 Immunohistochemistry for fixed brain tissue

After the brain was sliced, fixed, and washed as described above (slice thickness = 150 μm), the fixed slices were permeabilized with PBST (1% Triton-X in PBS) for 24 hours at room temperature on a shaker. The slices were then blocked with 5% bovine serum albumin (BSA) in PBST for 1 hour on a shaker. For cFos immunostaining, the slices were incubated with a rat anti-cFos primary antibody (1:1000 dilution in 1% BSA in PBST, Synaptic Systems, 226 017) for 24 hours at room temperature on a shaker. Slices were then washed in PBST for 20-min (x3), followed by 2-hour incubation with secondary antibody (1:500 in 1% BSA in PBST; AF_{488} anti-rat, Invitrogen, A-11006) at room temperature. After two additional 20-minute washes and one 24-hour wash in PBST at room temperature, the mounted slices were imaged on a confocal microscope. For GluA1-CTD immunostaining, the same experimental conditions were used, except different antibodies and their respective dilution factors were used (primary antibody: 1:500 diluted mouse anti-GluA1-CTD, Synaptic Systems 182 011; secondary antibody: 1:500 diluted AF_{647} goat anti-mouse, Abcam 150115). For GFAP immunostaining, the following antibodies were used; primary antibody: 1:500 diluted rabbit anti-GFAP, Abcam 7260; secondary antibody: 1:500 diluted AF_{488} goat anti-rabbit, Invitrogen A11008.

2.5.24 Confocal imaging of HT-GluA1 expressed in cultured rat hippocampal

neuron

Confocal images of fixed neuron cultures were acquired using LSM 980 (operated with Zeiss Zen (blue edition)) with 20× water immersion objective. AF_{488}, JF_{549i}, AF_{647} were excited with 488-nm, 561-nm, and 633-nm lasers, respectively. Pixel size was 0.052 μm by 0.052 μm and the size of each region of interest (ROI) was 424.27 μm by 424.27 μm (8192 pixels by 8192 pixels). Pixel time was 0.51 μs. The same imaging conditions were used throughout all experiments.

2.5.25 Confocal imaging of HT-GluA1 expressed in brain slice

Confocal images of fixed brain slices were acquired using LSM 980 (operated with Zeiss Zen (blue edition)) with 20× water immersion objective in z-stack. Images in **Figure 2.2a** (right), **2.3a** (right), and **2.3d** were acquired with 63× oil immersion objective. DAPI, eGFP, AF_{488}, JF_{549}, JF_{549i}, and AF_{647} were excited with 405-nm, 488-nm, 488-nm, 561-nm, 561-nm, 633-nm lasers, respectively. Non-specific autofluorescent artifacts were excited with 488-nm for **Figure 2.2** and 561-nm for **Figure 2.3** and the detection ranges were from 500-nm to 553-nm for **Figure 2.2f-i**, from 651-nm to 695-nm for **Figure 2.2j-n**, and from 500-nm to 553-nm for **Figure 2.3**. Voxel sizes were 0.052 μm by 0.052 μm by 2 μm for **Figure 2.2** (except for **Figure 2.2a**(right)) and 0.052 μm by 0.052 μm by 1 μm for **Figure 2.3** (except for **Figure 2.3a**(right)). For **Figure 2.2a**(right) and **2.3a**(right), the voxel size was 0.016 μm by 0.016 μm by 0.23 μm. Pixel time was 0.51 μs for all

experiments. The same imaging conditions were used for all samples within each set of experiments.

2.5.26 Image processing and data analysis

MATLAB (2019-2021), Fiji (1.54k), and Imaris (9-10) were used for image processing. All images were denoised with 2D gaussian filter before analysis. The same kernel sizes were applied to all data within each set of experiments.

Spine detection: The Imaris background subtraction function was applied to each image. The locations and fluorescence intensity values of spines were then determined by analyzing the intensity of the Dye 1 channel using the Imaris spot detection function (threshold: 'quality' above 130 for **Figure 2.1**, 600 for **Figure 2.2**, and 400 for **Figure 2.3**). Autofluorescent artifacts were identified by their intensities in the 'autofluorescence detection channel' (threshold: 'quality' above 300 for **Figure 2.1** and **2.2f-i**, 150 for **Figure 2.2j-n** and 1300 for **Figure 2.3**). Spots within 1 mm of the center of an autofluorescent artifact were excluded from analysis. To further reduce noise, spots whose average distance to 10 nearby spots was greater than 10 μm were filtered out. The same parameters were used throughout all experiments that required spine detection. For **Figure 2.3** and **2.4**, spines from different neurons in the same ROI were separated manually. The spines which showed labeling with Dye 2 only (i.e. synaptogenesis or AMPAR exocytosis from silent spines) were identified with the same criteria applied to the Dye 2 channel. Spots located within 4 μm from the nearest spine from Dye 1 were selected. However,

since the number of newly formed spines per cell was very small, further analysis was not pursued (**Figure 2.14c**). For background fluorescence analysis in **Figure 2.4f, g**, 1 μm diameter spherical regions were randomly placed, with the constraints that they were at least 3 μm away from the nearest dendrite and from each other and at least 1 mm from the center of any autofluorescent puncta. The fluorescence intensities in both dye channels of these spherical regions were calculated following the same procedure as for spines.

Threshold for defining potentiated spines: For each experimental condition, all spines from all ROIs were sorted into 300 bins based on their Dye 1 intensity. For each bin, we estimated the mean, m, and standard deviation, s, in the Dye 2 intensity of the non-potentiated spines from the bottom 95% of the Dye 2 distribution in that bin. A threshold was then set for each bin as m + 5 s, and spines with a Dye 2 intensity higher than the threshold were identified as 'potentiated'.

cFos segmentation: Z-stack images were segmented based on the cFos channel (AF_{488}) using Imaris and custom MATLAB code. The center coordinates of the nuclei were identified using Imaris (threshold: 'quality' above 1200), and a 20 μm by 20 μm image subset was defined around each center coordinate on the x-y plane. A binary mask was obtained from each image subset using the Otsu algorithm. Each binary mask underwent Euclidean distance transform followed by an extended minima transform. MATLAB function imextendedmin was used to filter out small local minima, and the remaining minima were imposed on the original binary mask. The resulting binary masks were segmented using the Watershed algorithm. Any masked area smaller than 45 μm^2 was

excluded from analysis. Background autofluorescence was calculated as the mean intensity of each non-masked area from the first Otsu thresholding. Background was subtracted from the mean intensity value within each masked area.

Dendrite classification by branch order and spine assignment to dendrites: In Imaris, the coordinates of each dendrite were manually identified and extracted from each z-stack image. For all dendrites, their branch orders were manually identified, and they were numbered according to their relative positions. For instance, #1340000 represents the fourth dendrite from the third second-ordered dendritic segment of the first first-ordered dendritic segment and its branch order is 3. The first digit of basal dendrite numbers ranged from 1 to 7, while the first digit of apical dendrite numbers ranged from 8 to 9. Custom MATLAB code was used to smooth these coordinates with the smoothdata function. Next, each dendrite was converted into 1000 equally spaced points using linear interpolation. The x, y, and z coordinates were imported from Imaris to MATLAB. For each spine, the dendrite closest to the spine was identified by determining the dendritic point with the shortest Euclidean distance to the spine. This dendrite was registered as the spine's dendrite.

Distribution of spines as a function of projected and contour distances from soma: The coordinates of all spines were transformed to match the dorsal-ventral (DV) axis of the neuron they belonged to. The centers of rotation for each neuron were manually determined by referring to the original confocal images and defined as the origin. In **Figure 2.4a** and **2.11c**, each spine point was orthogonally projected onto the

corresponding DV axis crossing at the origin. The distance from the projected point to the origin was calculated and displayed. The distance values were binned into 50 groups, and the total number of spines, number of spines above threshold, and the fraction of spines above threshold were calculated for each bin. In **Figure 2.11d-f**, the contour distance from the soma to each spine was calculated by adding the distance from the spine to one of the dendritic endpoints closer to the soma and the lengths of all dendrites between the endpoint and the soma.

Calculation of pairwise distance distribution between potentiated spines: For each potentiated spine, the distances to all other potentiated spines within 30 mm dendrite contour distance were tabulated. The histogram of these values gave the pairwise distance distribution. For the random allocation, the same number of spines on each dendrite were randomly and independently selected and assigned as "pseudo potentiated spines". The fraction of "pseudo potentiated spines" was calculated using the same method as above.

Distribution of the expected number of potentiated spines per dendrite segment: Within each neuron and each branch order, we quantified the number of potentiated spines, n_i, and the total number of spines, a_i, in each dendritic segment i, and the total number of potentiated spines, N, and all spines, A, across all dendrite segments at the corresponding branch order. Next, we performed 500 simulations where we randomly distributed the N potentiated spines across the dendritic segments, with probability a_i/A of landing in segment i. We calculated the theoretical distribution of number of potentiated spines for each dendritic segment, $P(\hat{n}_i)$, under the assumption of random and

independent allocation within each branch order.

We then compiled all dendrite segments from all branch orders and all neurons and sorted them based on the expected mean number of potentiated spines derived from the simulations, $\langle \hat{n}_i \rangle$. The sorted data were then divided into 10 groups of 130 dendrites each, and for each group, we computed the probability distribution of both the expected and measured number of potentiated spines. The four groups with the highest mean number of potentiated spines showed the most distinct differences between experiment and random allocation model, so these were selected to plot in **Figure 2.4c**.

Fraction of spine clusters with different sizes: We identified clusters of potentiated spines, first identifying clusters with the largest number of potentiated spines ($N = 14$ in our analysis) and then proceeding iteratively to analyze the remaining spines for clusters of size $N - 1$, $N - 2$, and so on. A cluster was defined as having N potentiated spines within a region containing $2N$ total spines on the dendrite. Once a cluster was identified and counted, its constituent spines were excluded from further counting to avoid duplication.

2.5.27 Statistics and reproducibility

All statistical tests performed are specified in the figure legends. Differences with values of $P < 0.05$ were considered statistically significant. Sample sizes were determined by the technical requirements of the experiments. No data was excluded from the analyses. Individual animals were indistinguishable in terms of HT-GluA1 expression status at the

time of the experiments and were therefore randomly selected. Data collection was not conducted blinded to experimental conditions.

Statistical analyses were performed using MATLAB. Normality of datasets was assessed with the Shapiro–Wilk test ($P > 0.05$ indicates normal distribution). For paired datasets, a two-tailed paired t-test was used for normally distributed data, and a Wilcoxon signed-rank test was used for non-normally distributed data. For unpaired datasets, a two-tailed unpaired t-test was used for normally distributed data, and a Mann–Whitney U test was used for non-normally distributed data.

2.6 Supplemental figures

Figure 2.5 ***(following page)*****:** ***In vitro*** **characterization of EPSILON. (a)** Selective labeling of surface HT-GluA1 with membrane-impermeable HTL dye. Left: Cultured neuron expressing HT-GluA1 stained with membrane-impermeable AF_{488}-HTL while alive. Right: Another HT-GluA1 expressing cultured neuron stained with the same dye after fixation to permeabilize the cell membrane. Scale bars 10 μm. **(b)** Manders' overlap coefficient between HT-GluA1 and PSD95 (PSD95.FingR-eGFP). n = 13 dendritic segments from 7 neurons. Error bars show mean ± s.e.m. **(c)** Confocal images of a fixed cultured neuron expressing (top) JF_{549}-labeled HT-GluA1 stained with (middle) anti-GluA1-CTD (c-terminal domain) antibody. (Bottom) Merge. Scale bar, 1 μm. **(d)** Relationship between HT-GluA1 intensity and GluA1 antibody intensity among spines. n = 32 spines from 5 neurons. R, Pearson's linear correlation coefficient, P value from two-sided Student's t-test. **(e)** GluA1 expression level in HT-GluA1 +/- neurons stained with anti-GluA1-CTD antibody (n = 11 dendritic segments from 5 neurons for each group). Two-sided Wilcoxon rank-sum test. Error bars show mean ± s.e.m. **(f)** Confocal images of fixed cultured neurons showing labeling of HT-GluA1 with AF_{488}-HTL (100 nM, cyan) or JF_{549i}-HTL (1 μM, orange) or AF_{647}-HTL (1 μM, red) at different times after dye addition. Scale bars: 100 μm. **(g-i)** Fluorescence vs. dye incubation time for cultured neurons expressing HT-GluA1 and treated with **(g)** AF_{488}-HTL (100 nM) or **(h)** JF_{549i}-HTL (1 μM) or **(I)** AF_{647}-HTL (1 μM). (n = 5 cells for each timepoint). Data are represented as mean ± SD. Red: fitted curve. **(j)** Surface GluA1 was saturated by labeling with 100 nM AF_{488}-HTL for 5 minutes, followed immediately by chase-dye labeling (1 μM of JF_{549i}-HTL for 30 s). **(k)** Confocal images of fixed cultured neurons after saturation with AF_{488}-HTL (left) with and (middle) without JF_{549i}-HTL chase. (Right) JF_{549i}-HTL only without AF_{488}-HTL. Scale bars: 50 μm. **(l)** JF_{549i}-to-AF_{488} intensity ratios (n = 16 cells from 3 cultures for Dye 2 +; n = 16 cells from 3 cultures for Dye 2 -; n = 12 cells from 3 cultures for Dye 2 only). Error bars show mean ± s.e.m. Two-sided Student's t-test. **(m)** Surface GluA1 was saturated by labeling with 1 μM AF_{647}-HTL for 1 minute, followed immediately by chase-dye labeling (1 μM of JF_{549i}-HTL for 30 s). **(n)** Confocal images of fixed cultured neurons (left) with and (middle) without JF_{549i}-HTL after saturation with AF_{647}-HTL. (Right) JF_{549i}-HTL only without AF_{647}-HTL. Scale bars: 50 μm. **(o)** JF_{549i}-to-AF_{647} intensity ratios (n = 5 cells from 2 cultures for each group). Error bars show mean ± s.e.m. Two-sided Student's t-test. **(p)** Experimental timeline of surface HT-GluA1 turnover measurement with multi-color labeling. **(q)** Confocal images of fixed cultured neurons showing replacement of old (AF_{488}, cyan) with new (JF_{549i}, orange) AMPARs. Scale bars: 200 μm. Turnover occurred faster in soma and perisomatic neurites than in distal neurites. **(r)** Normalized dye intensity ratio at 5, 20, 30, 60, and 120-min (n = 5 cells for each timepoint). Normalized dye intensity ratio: 2^{nd} dye intensity / (1^{st} dye intensity + 2^{nd} dye intensity). Data are represented as mean ± SD. Parts of (j), (m), and (p) were created using Biorender and are used with permission.

Figure 2.5: (Continued)

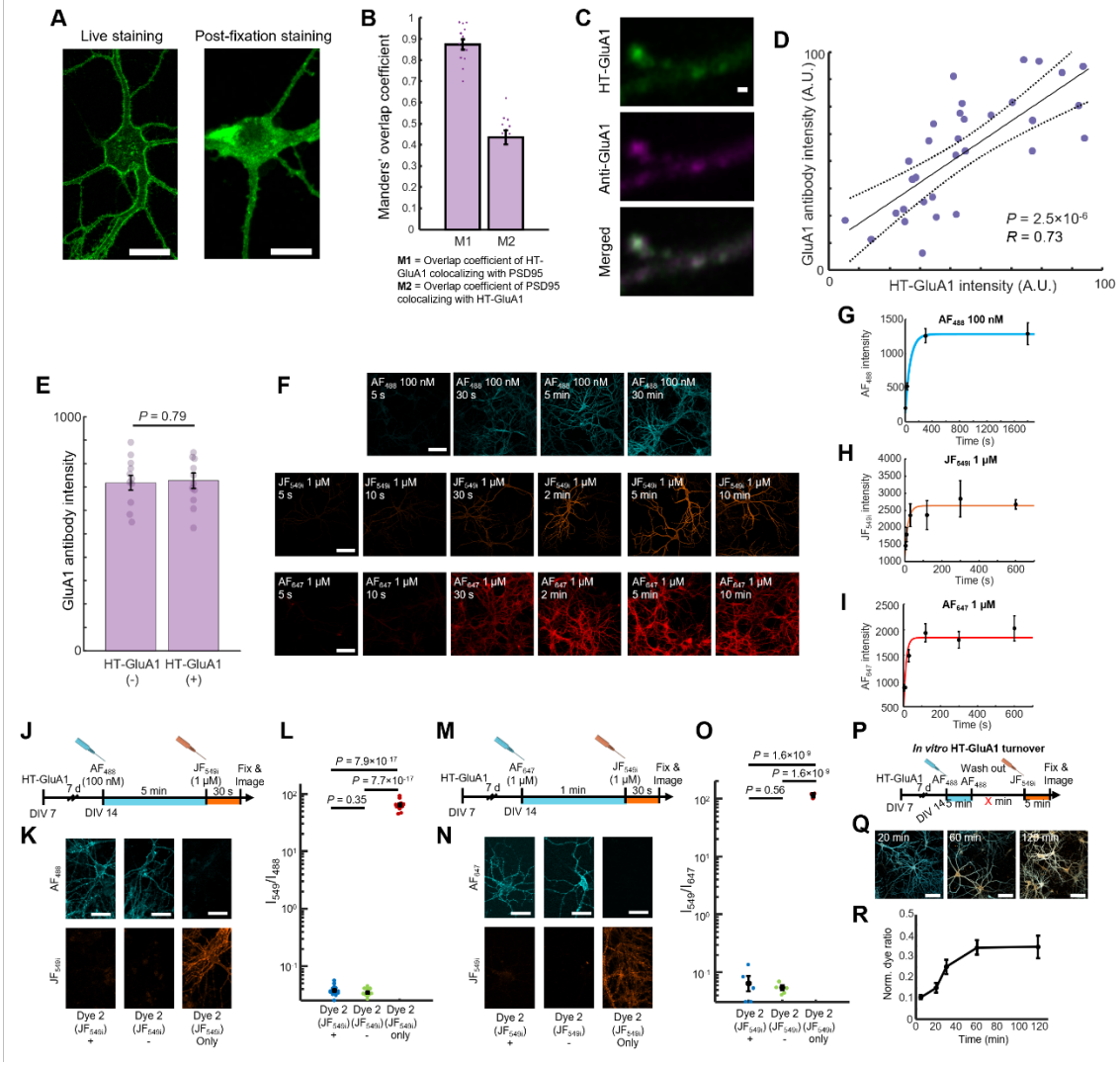

Figure 2.6 ***(following page)*****: Effects of MNI-glutamate uncaging and cLTP on AMPAR exocytosis. (a)** Time-lapse images of the stimulated spines expressing GPI-eGFP +/- HT-GluA1 expression. Scale bars, 10 µm. **(b)** Time course for spine size increases +/- HT-GluA1 expression (HT-GluA1 (+): n = 13 spines from 3 neurons; HT-GluA1 (-): n = 14 spines from 3 neurons). Error bars show mean ± s.e.m. **(c)** Confocal images of spines expressing GPI-eGFP (green) and HT-GluA1 labeled with Dye 1 (cyan, AF_{647}) and Dye 2 (orange, JF_{549i}), before and after glutamate photo-uncaging. Controls had no glutamate uncaging. Scale bars, 1 µm. **(d)** Dye 1 intensity change for control and uncaged spine groups. Control: n = 10 spines; Uncaged: n = 20 spines. Two-sided Wilcoxon rank-sum test. Error bars show mean ± s.e.m. **(e)** Correlation between the change in Dye 1 intensity and the change in spine size for spines from **(d)**. R, Pearson's linear correlation coefficient, P value from two-sided Student's t-test. **(f)** Scatterplots of spine fluorescence intensities in the two color channels for (left) control, (middle) cTLP-treated, and (right) TeTX-LC co-expressing neurons. Same data as in **Figure 2.1m**, with vertical scale adjusted to include all spines. Control: n = 32,828 spines from 6 cultures; cLTP: n = 47,090 spines from 6 cultures; TeTX-LC: n = 17,231 spines from 6 cultures. Dye 2 intensity thresholds indicated with dashed lines (see Methods for calculation of threshold). Replicate dishes represented by different shape symbols. **(g)** The extent of AMPAR exocytosis in each spine measured by the fluorescence of Dye 2 above threshold. Spines with Dye 2 intensity higher than the threshold were included for analysis (control: 1,563 ± 112 counts, mean ± s.e.m., n = 195 spines, 54 neurons, 6 cultures, cLTP: 2,398 ± 74.9 counts, mean ± s.e.m., n = 1,024 spines, 44 neurons, 6 cultures; TeTX-LC: 868.7 ± 147 counts, mean ± s.e.m., n = 35 spines, 45 neurons, 6 cultures). Replicate dishes represented by different symbols. Box plot shows extrema, 25th and 75th percentiles and median. Two-sided Wilcoxon rank-sum test.

Figure 2.6: (Continued)

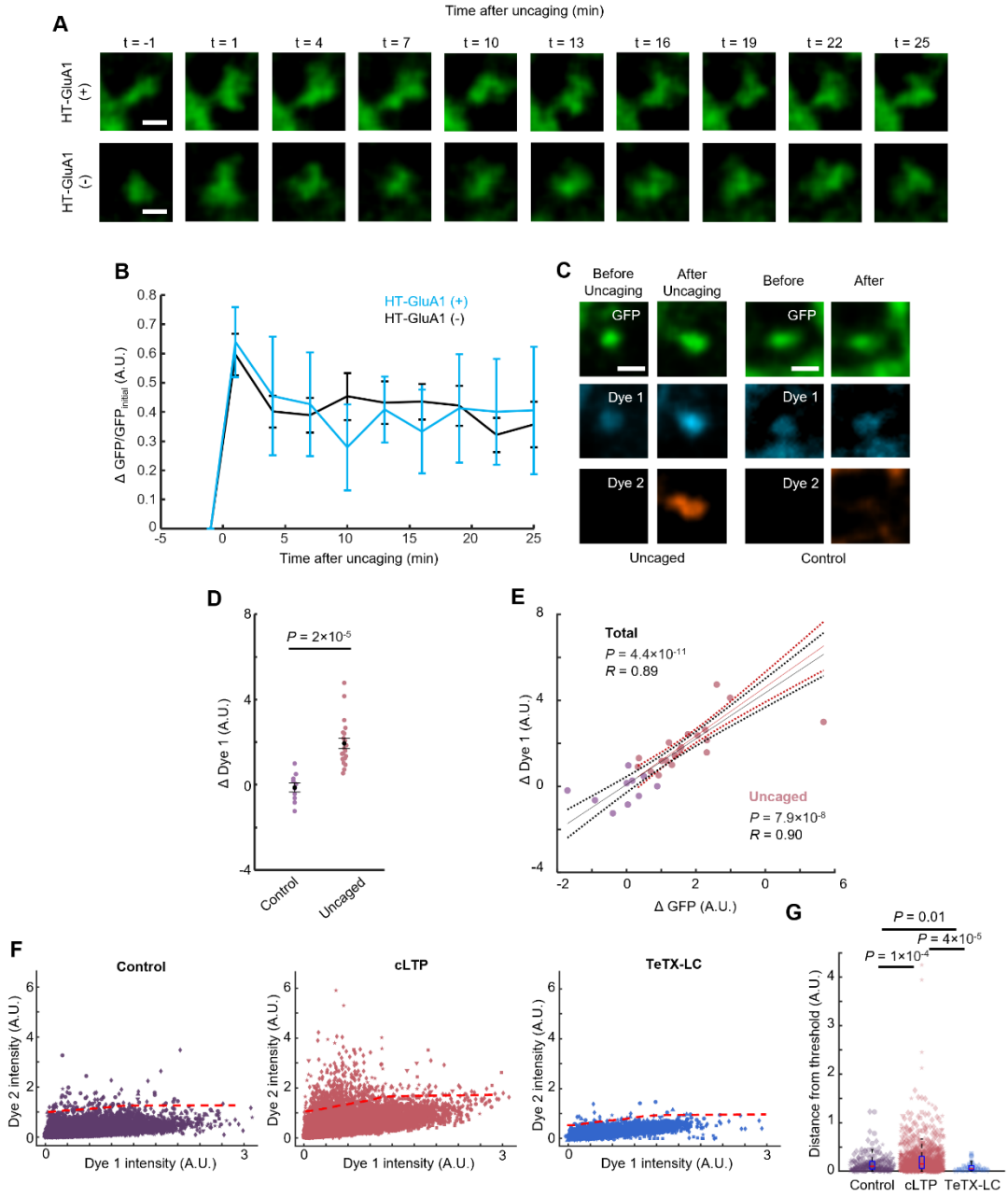

Figure 2.7 ***(following page)*****: Validation of EPSILON in mouse brain.** HT-GluA1 stained with AF_{647}-HTL in **(a)** barrel cortex **(b)** CA1 pyramidal cells. Each set of micrographs represents a single experiment. Scale bars 50 mm. **(c)** Postsynaptic trafficking of HT-GluA1 in layer 2/3 pyramidal neurons in barrel cortex. (Left) HT-GluA1 stained with JF_{549i}-HTL. (Middle) PSD95 (PSD95.FingR-eGFP) from same region of interest. (Right) Merge. Scale bars, 5 μm. **(d), (e)** Dendritic segments expressing **(d)** HT-GluA1 only or **(e)** PSD95.FingR-eGFP only. Scale bars, 2 μm. **(f)** Manders' overlap coefficient between HT-GluA1 and PSD95 (PSD95.FingR-eGFP). n = 9 dendritic segments from 5 neurons. Error bars show mean ± s.e.m. **(g)** Correlation between PSD95.FingR-eGFP intensity and HT-GluA1 intensity on individual spines (n = 112 spines from 8 dendritic segments from 8 neurons). R, Pearson's linear correlation coefficient, P value from two-sided Student's t-test. HT-GluA1 expressing layer 2/3 pyramidal neurons in barrel cortex in acute brain slices were identified by staining with 1uM JFX_{608}-HTL. **(h)** Representative patch-clamp recordings in acute brain slice. **(i)** Measurements of electrophysiological properties of neurons with or without HT-GluA1 expression. Membrane resistance: 204 ± 16 MΩ vs. 212 ± 12 MΩ, P = 0.69; membrane capacitance: 47 ± 5 pF vs. 43 ± 3 pF, P = 0.50; resting potential: −68.1 ± 1.4 mV vs. −69.2 ± 1.1 mV, P = 0.53; and rheobase 97 ± 9.8 pA vs. 94 ± 15 pA, P = 0.86 (n = 13 neurons for each group). Error bars show mean ± s.e.m. n.s. not significant, two-sided Student's t-test. Spine density on dendritic segments from neurons +/- HT-GluA1 in **(j)** layer 2/3 pyramidal neurons in barrel cortex and **(k)** pyramidal neurons in CA1 (HT-GluA1 (+) in barrel cortex: n = 11 dendritic segments from 10 neurons; HT-GluA1 (-) in barrel cortex: n = 11 dendritic segments from 11 neurons; HT-GluA1 (+) in CA1: n = 8 dendritic segments from 5 neurons; HT-GluA1 (-) in CA1: n = 8 dendritic segments from 4 neurons). Two-sided Wilcoxon rank-sum test. Error bars show mean ± s.e.m. **(l)** Confocal images of HT-GluA1 stained with JF_{549}-HTL (orange), co-expressed GPI-eGFP (green), and immunostained for GluA1 (red). Selected regions for quantifying GluA1 expression levels in neurons with HT-GluA1 (red) or without HT-GluA1 (yellow) are indicated on the GPI-eGFP panels. HT-GluA1 (+) and (-) regions were selected to be within 100 μm of each other, considering possible heterogenous immunostaining. Scale bars, 10 μm. **(m)** GluA1 expression level in HT-GluA1 +/- neurons (n = 10 neurons from 3 animals for each group). Two-sided Wilcoxon rank-sum test. Error bars show mean ± s.e.m.

Figure 2.7: (Continued)

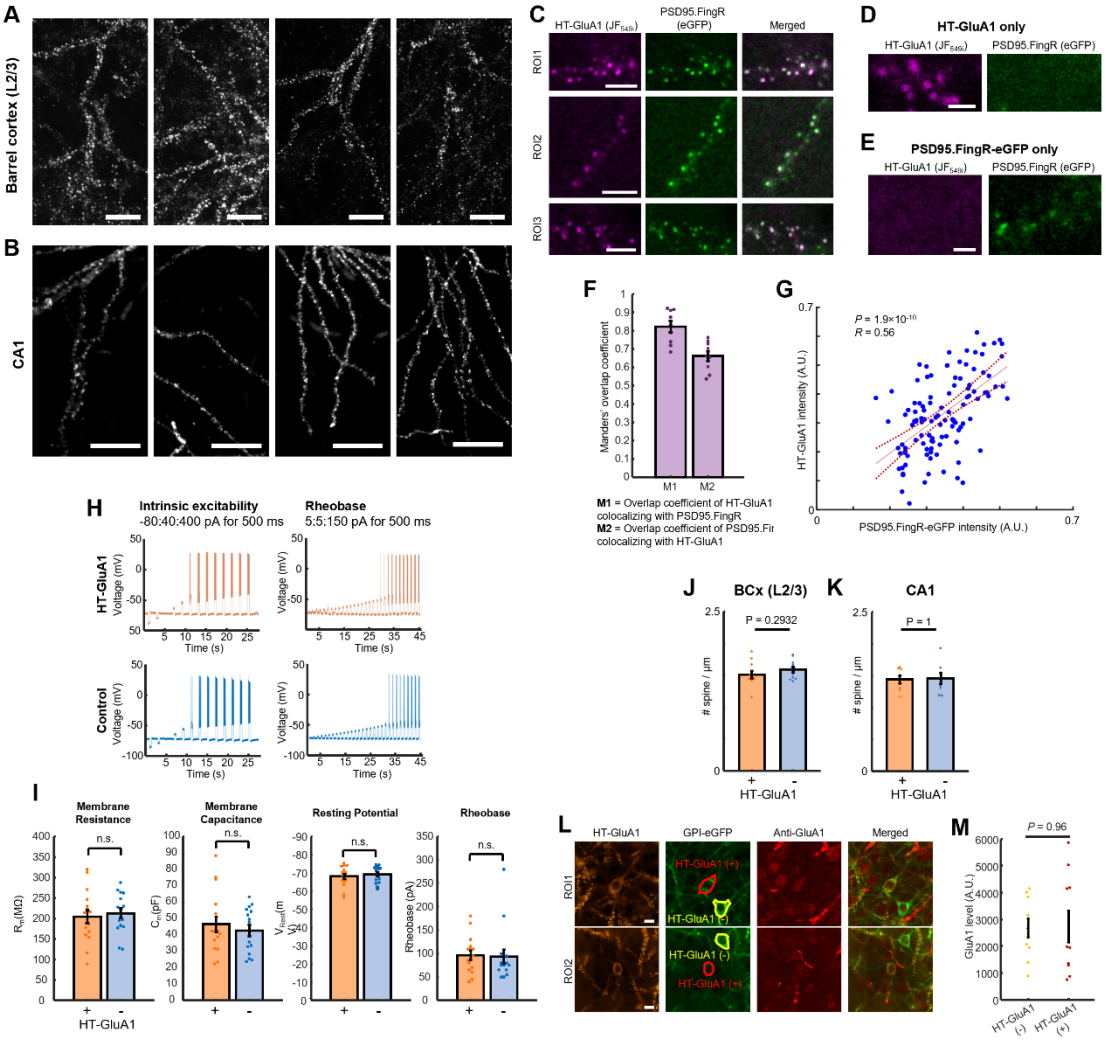

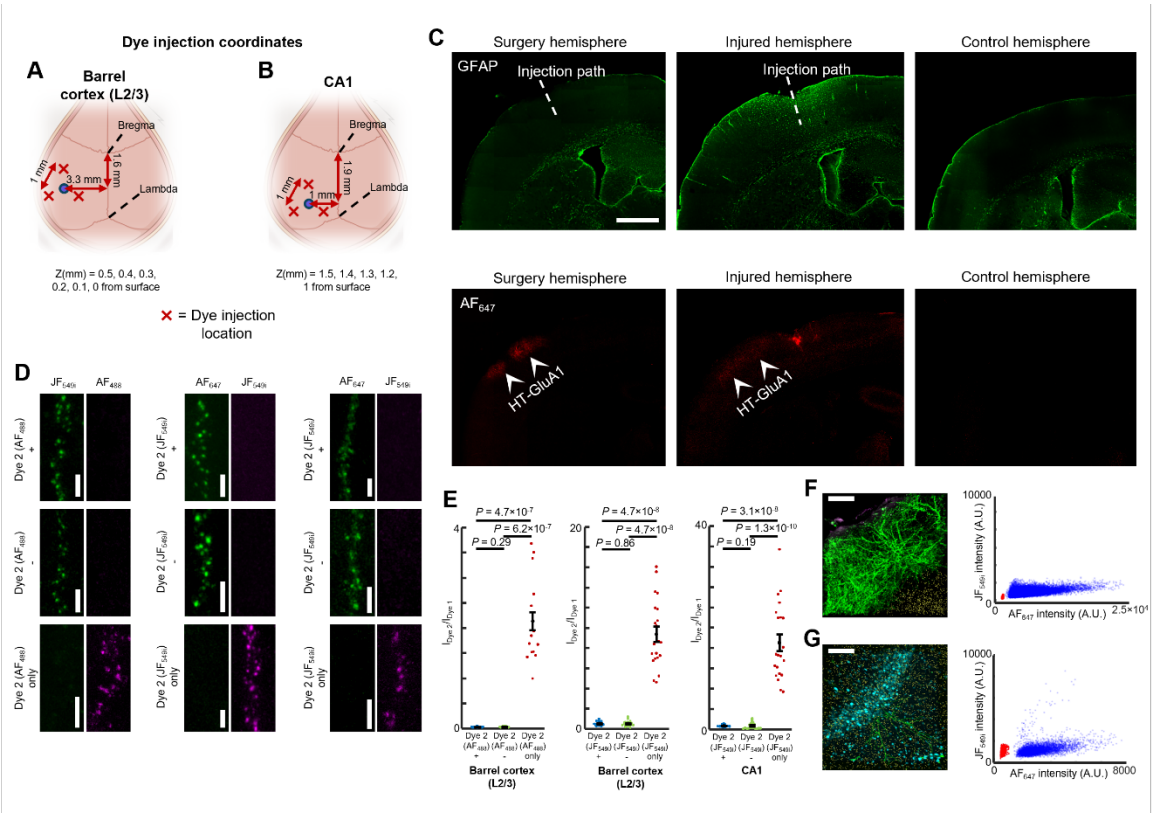

Figure 2.8: HaloTag dye labeling in live mouse brain. (a) Relative coordinates from bregma and lambda for intracortical dye injections to cover layer 2/3 pyramidal neurons in left barrel cortex. **(b)** Relative coordinates from bregma and lambda for intrahippocampal dye injections to cover CA1 pyramidal neurons in left hippocampus. **(c)** Immunostaining of the astrocyte marker GFAP after dye injections. (Top) GFAP expression in the (top left) surgery hemisphere, (top middle) intentionally injured hemisphere, and (top right) control hemisphere without dye injection. (Bottom) HT-GluA1 stained with AF_{647}-HTL in the same regions of interest as the upper panels. 1 µM of AF_{647}-HTL was injected at three different sites as shown in **(a)** (80 nL at each depth) three times (20 minutes between the 1st and 2nd injections; 90 minutes between the 2nd and 3rd injections). Some of the injection paths are indicated by white dashed lines on the GFAP panels. These injections were performed 7 days after the installation of the injection port (see Methods). Each set of micrographs represents a single experiment from at least three repeated experiments. Scale bar, 1 mm. **(d)** Saturated labeling of surface GluA1 with Dye 1 blocked chase-dye labeling with Dye 2. Surface GluA1 was saturated by labeling with (left) 1 µM JF_{549i}-HTL for 20 minutes in layer 2/3 barrel cortex, (middle) 1 µM AF_{647}-HTL for 20 minutes in layer 2/3 barrel cortex, (right) 1 µM AF_{647}-HTL for 20 minutes in CA1. After Dye 1 labeling, 10 µM of Dye 2 was immediately injected to the same injection sites (Methods). Confocal images show Dye 1 (green) and Dye 2 (magenta) labeled dendrites (top) with Dye 2, (middle) without Dye 2, and (bottom) Dye 2 only. Scale bars, 5 µm. **(e)** Dye 2-to-Dye 1 intensity ratios for the injection conditions from **(d)**. $n = 21$ dendritic segments from 3 neurons, 20 dendritic segments from 3 neurons, 15 dendritic segments from 3 neurons for Dye 2 (+), Dye 2 (-), Dye 1 only groups in JF_{549i}/AF_{488} in barrel cortex, respectively; $n = 21$ dendritic segments from 3 neurons for each group in AF_{647}/JF_{549i} in barrel cortex; $n = 21$ dendritic segments from 3 neurons for each group in CA1. Error bars show mean ± s.e.m. Two-sided Student's t-test. **(f)** Background fluorescence analysis in mouse barrel cortex layer 2/3. Left: Spherical regions of interest (yellow) used for background fluorescence measurement on top of **Figure 2.2g**. Right: Scatterplots of spine (blue) and background (red) fluorescence intensities ($n =$ 53,457 spines and 747 background regions). **(g)** Background fluorescence analysis in mouse CA1. Left: Spherical regions of interest (yellow) used for background fluorescence measurement on top of Figure 2.3c. Right: Scatterplots of spine (blue) and background (red) fluorescence intensities ($n = 5,314$ spines and 2,836 background regions). Scale bars: 200 µm. Parts of (a) and (b) were created using Biorender and are used with permission.

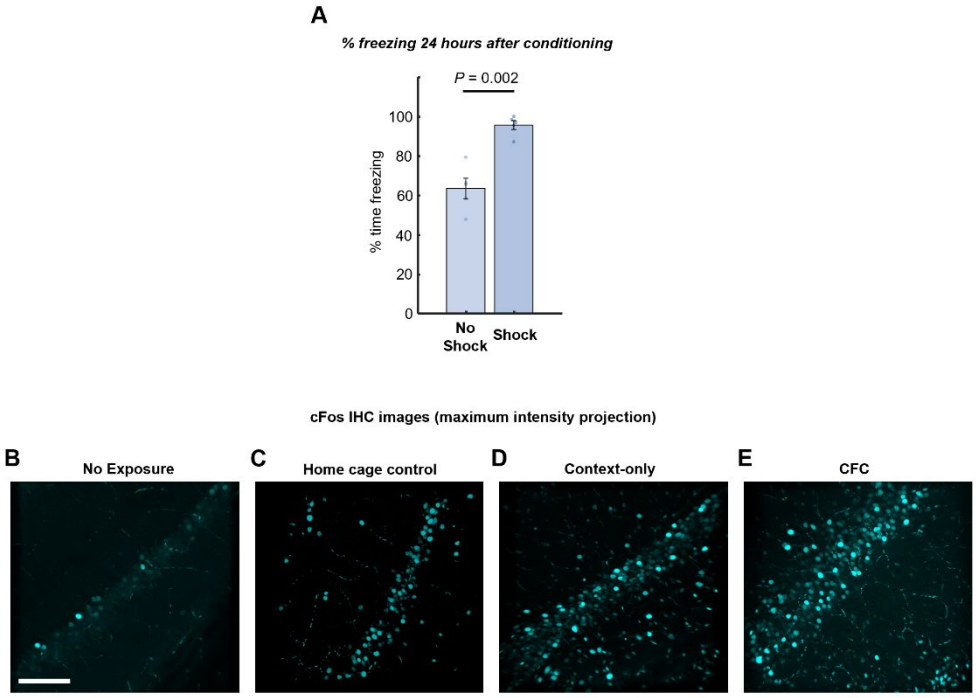

Figure 2.9: Validation of contextual fear conditioning protocol. (a) The CFC system was validated by measuring the percent of time mouse spent freezing (i.e. immobile) 24 hours after conditioning. The percentage of freezing was measured for the mice that underwent full conditioning (shock) and for the mice exposed to the identical context but that did not receive an aversive stimulus (no shock). Error bars represent mean ± s.e.m. (n = 5 mice for each group). Two-sided Wilcoxon rank-sum test. Representative images from CA1 from mice that **(b)** were not exposed to any context (i.e. euthanized after 3 hours of anesthesia), **(c)** were not exposed to the novel context (stayed in their home cages, home cage control), **(d)** were exposed to the novel context but did not receive an aversive foot shock (context-only), and **(e)** underwent CFC. The images are shown in the same contrast scale and are maximum-intensity projections of z-stacks. These images are representative of the dataset used in **Figure 2.3m**. Scale bars: 200 μm.

Figure 2.10 ***(following page)*****: Relationships among cFos expression, AMPAR exocytosis levels, and percentage of potentiated spines. (a)** Relation of the percentage of potentiated spines to the mean HT-GluA1 exocytosis among potentiated spines (distance of Dye 2 signal above threshold, averaged over above-threshold spines), for (left) CFC and (right) context-only control. **(b)** Relation between the mean HT-GluA1 exocytosis among potentiated spines and the corresponding cFos intensity. CFC: n = 19 cells from 4 animals; context-only: n = 22 cells from 6 animals. R, Pearson's linear correlation coefficient, P value from two-sided Student's t-test. Distinct animals represented by different shape symbols. **(c)** Relation between the percentage of potentiated spine and the z-coordinate of the center of soma of the corresponding neuron for (left) CFC, (middle) context-only control, and (right) home cage control. **(d)** Relation between cFos intensity and the z-coordinate of the center of soma of the corresponding neuron for (left) CFC, (middle) context-only control, and (right) home cage control. **(e)** Relation between the total number of identified spines and the z-coordinate of the center of soma of the corresponding neuron for (left) CFC, (middle) context-only control, and (right) home cage control. CFC: n = 19 cells from 4 animals; context-only: n = 23 cells from 6 animals; home cage control: n = 12 cells from 3 animals. R, Pearson's linear correlation coefficient, P value from two-sided Student's t-test. Distinct animals represented by different shape symbols. **(f)** Relation between the total number of identified spines and the cFos intensity of the corresponding neuron for (left) CFC, (middle) context-only control, and (right) home cage control. CFC: n = 19 cells from 4 animals; context-only: n = 23 cells from 6 animals; home cage control: n = 12 cells from 3 animals. R, Pearson's linear correlation coefficient, P value from two-sided Student's t-test. Distinct animals represented by different shape symbols. Relation between the total number of identified spines and the cFos intensity of the corresponding neuron for (left) CFC, (middle) context-only control, and (right) home cage control. CFC: n = 19 cells from 4 animals; context-only: n = 23 cells from 6 animals; home cage control: n = 12 cells from 3 animals. R, Pearson's linear correlation coefficient, P value from two-sided Student's t-test. Distinct animals represented by different shape symbols.

Figure 2.10: (Continued)

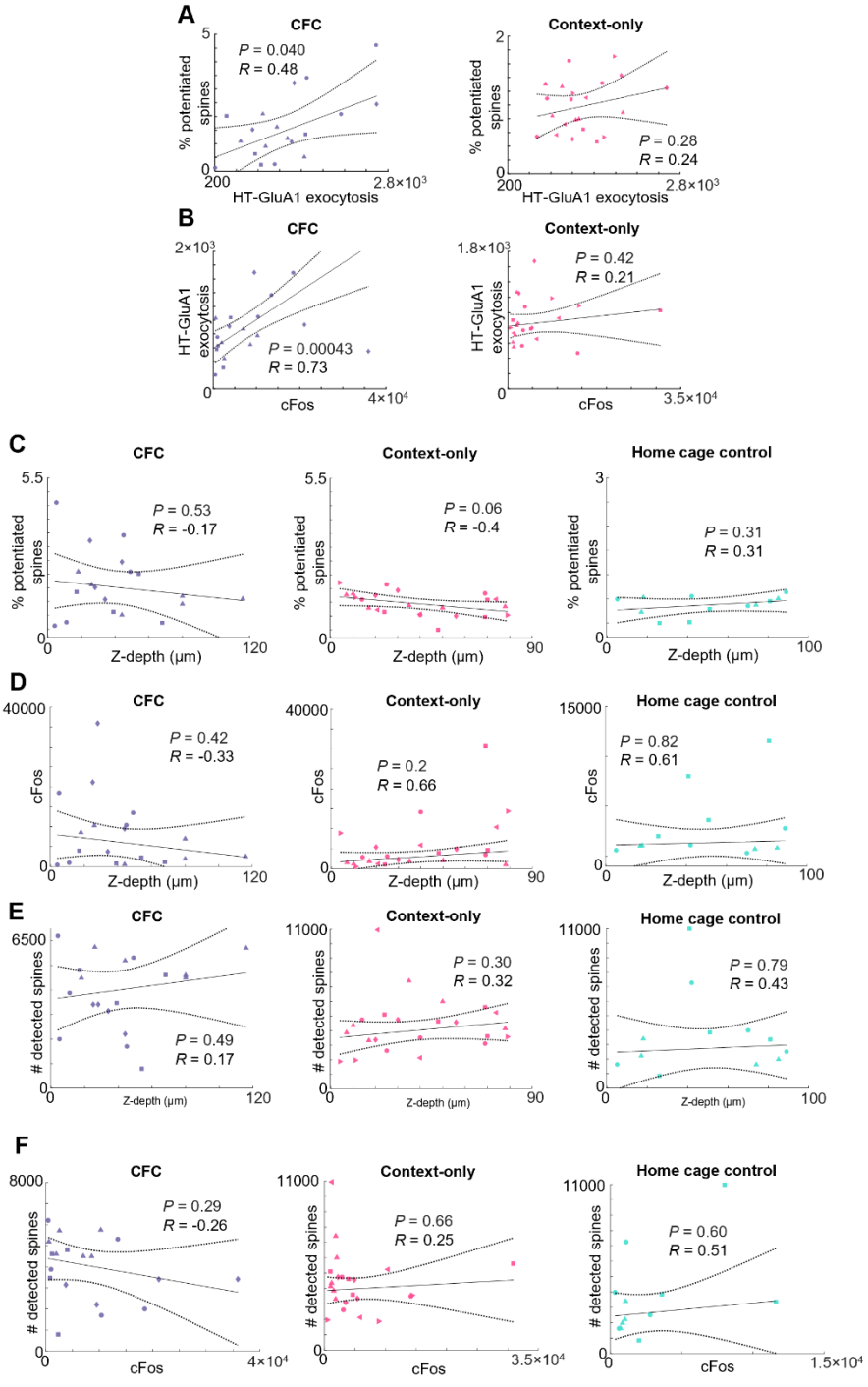

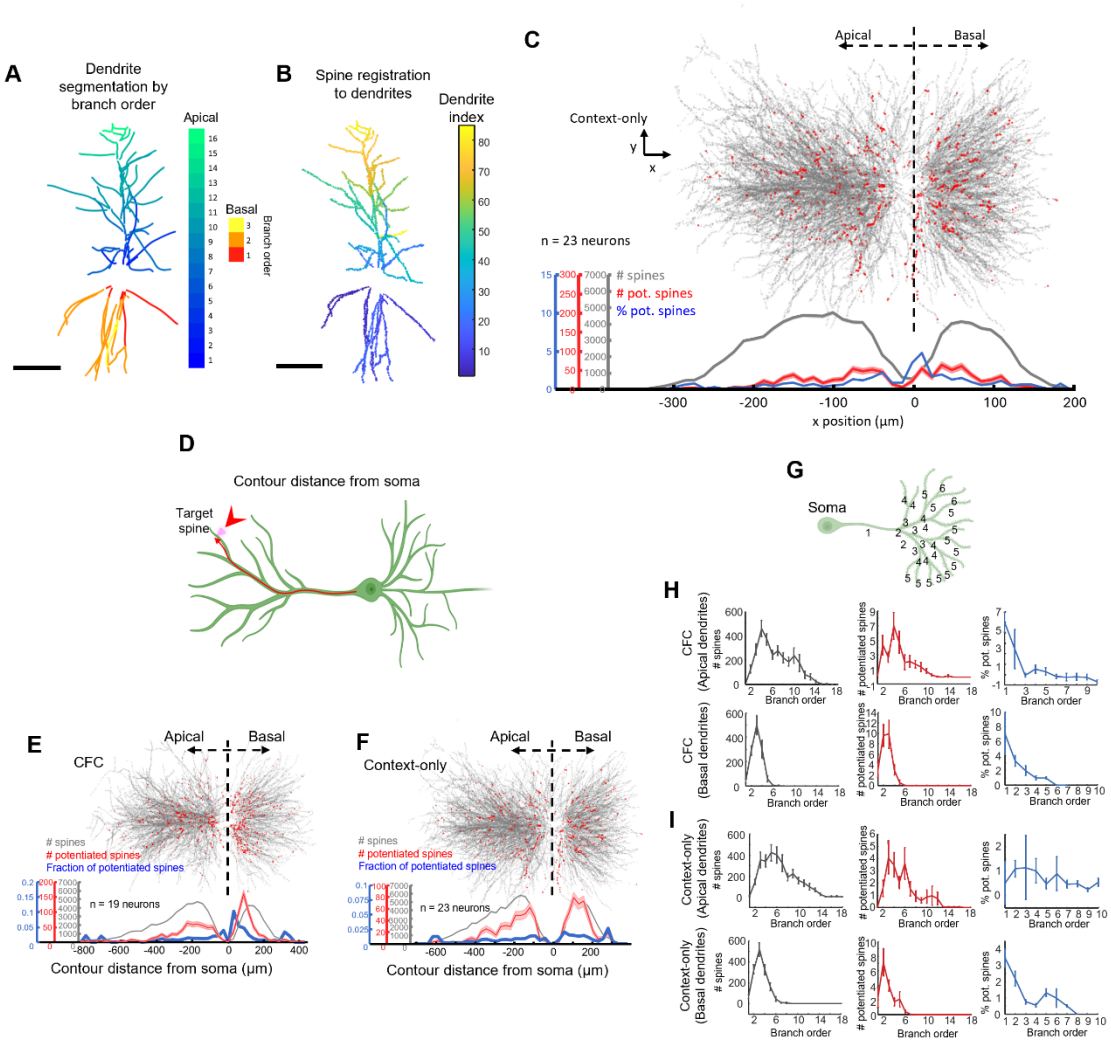

Figure 2.11: Subcellular distribution of potentiated spines. (a) Representative neuron with dendrites segmented and colored by their branch order. **(b)** Same neuron with spines registered to the nearest segmented dendrites. Scale bars: 100 μm. **(c)** Distribution of potentiated spines as a function of projected distance from the *stratum pyramidale*. (Top) Overlapped images of all identified spines (grey) and spines with high HT-GluA1 exocytosis (red) from the context-only control group. (Bottom) Total number of identified spines (grey), number of spines with high HT-GluA1 exocytosis (red), and fraction of potentiated spines (blue) plotted against the projected distance from the *stratum pyramidale* (x-axis from the top panel). Error bars represent count ± sqrt(count). **(d)** Schematic diagram showing the contour distance of a neuron's spine from its soma. This is the distance along the dendrite backbone. **(e, f)** Same data as in **Figure 2.4a** and **(c)**, but plotted vs. contour distance instead of *x*. **(g)** Schematic drawing of a neuron with dendrites numbered by their branch order. **(h), (i)** Total number of identified spines (left), number of potentiated spines (middle), fraction of potentiated spines (right) vs. corresponding dendrites' branch order from (top) apical dendrites or (bottom) basal dendrites in **(h)** CFC group and **(i)** context-only controls. CFC: $n = 19$ neurons; context-only: $n = 23$ neurons. Data are represented as mean ± s.e.m. The right panels are truncated due to the division by small numbers of spines on branch orders greater than 10. Parts of (d) and (g) were created using Biorender and are used with permission.

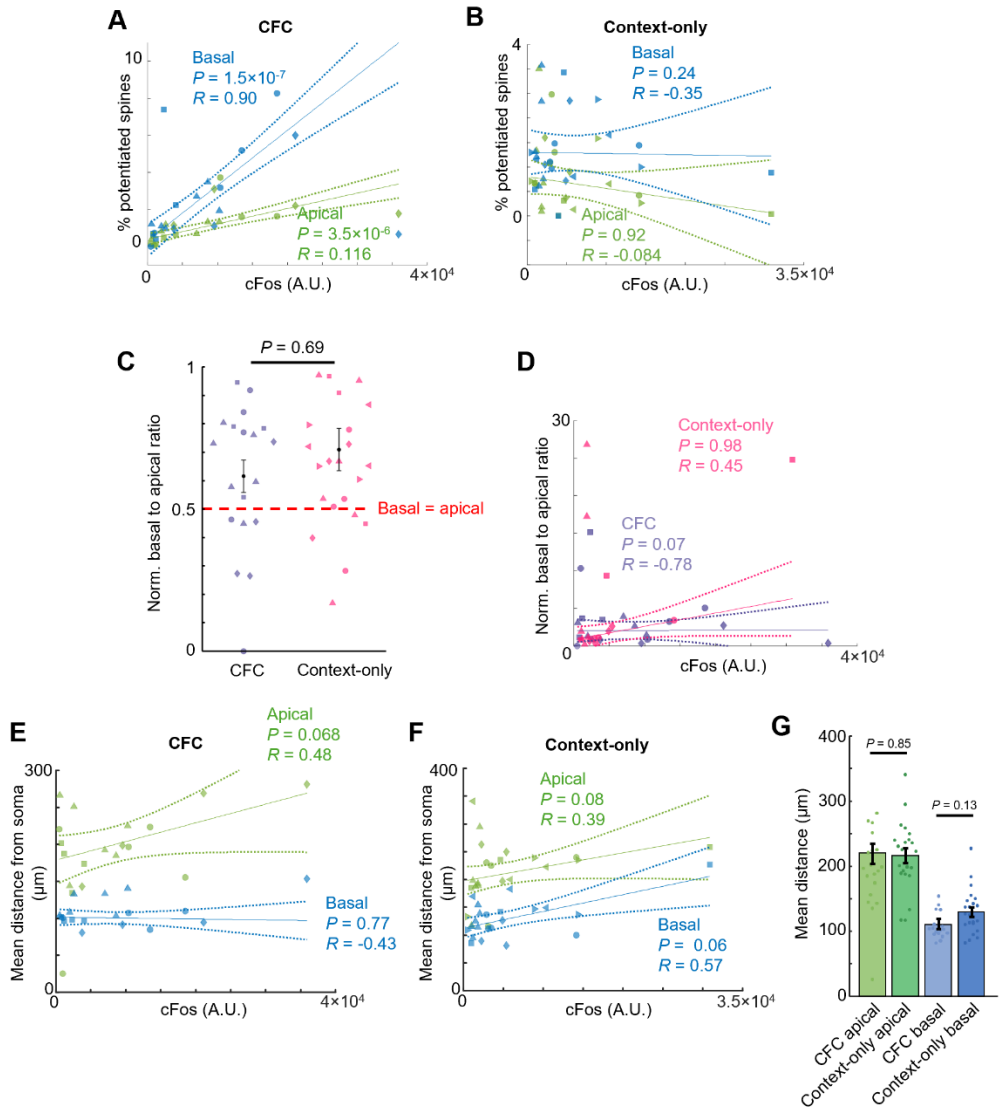

Figure 2.12: Comparison of AMPAR exocytosis in basal vs. apical dendrites. Fraction of potentiated spines for each neuron vs. cFos intensity for **(a)** CFC (n = 19 neurons) and **(b)** context-only control (n = 23 neurons). Spine fraction was separately evaluated for basal and apical dendrites. **(c)** Normalized basal to apical ratio of percent potentiated spines. Normalized ratio: basal percent potentiated spines / (basal percent potentiated spines + apical percent potentiated spines). 13 of 19 neurons in the CFC group and 17 of 23 neurons in the context-only group had higher basal than apical fraction of potentiated spines. There was no significant difference between the CFC and context-only groups in the ratio of basal to apical potentiated spines (CFC: 0.61 ± 0.06, mean ± s.e.m.; context-only: 0.70 ± 0.07, mean ± s.e.m.). Two-sided Wilcoxon rank-sum test. **(d)** Basal to apical ratio of percent potentiated spines vs. cFos intensity. The basal to apical ratio was not correlated with the corresponding cFos levels. R, Pearson's linear correlation coefficient, P value from two-sided Student's t-test. Distinct mice represented by different shape symbols. Mean contour distance from soma to potentiated spines vs. corresponding cFos intensity for **(e)** CFC group and **(f)** context-only control. The mean distance was separately evaluated for spines in basal and apical dendrites. R, Pearson's linear correlation coefficient, P value from two-sided Student's t-test. Distinct mice represented by different shape symbols. **(g)** Mean contour distance from soma to potentiated spines in CFC and context-only group. Data are represented as mean ± s.e.m. Two-sided Wilcoxon rank-sum test. CFC: n = 19 neurons; context-only: n = 22 neurons.

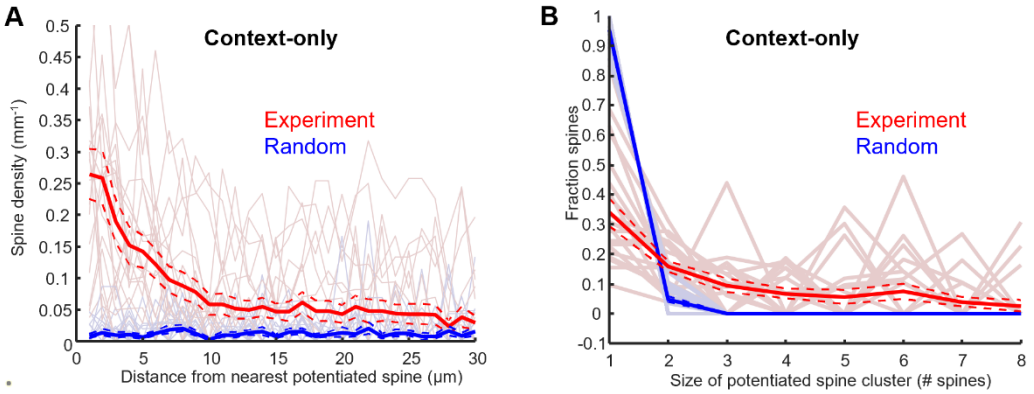

Figure 2.13: Clustering of potentiated spines in context-only control. (a) Density profile of potentiated spines as a function of distance from the nearest potentiated spine. The single-cell profiles are plotted with light colors. Random: simulation where the same number of potentiated spines are distributed randomly and independently among all detected spines. Bold and dashed lines represent mean ± s.e.m. **(b)** Fraction of potentiated spine clusters of different sizes from the context-only group (n = 22 neurons). The single-cell profiles are plotted with light colors. Bold and dashed lines represent mean ± s.e.m. Random defined as in **(a)**.

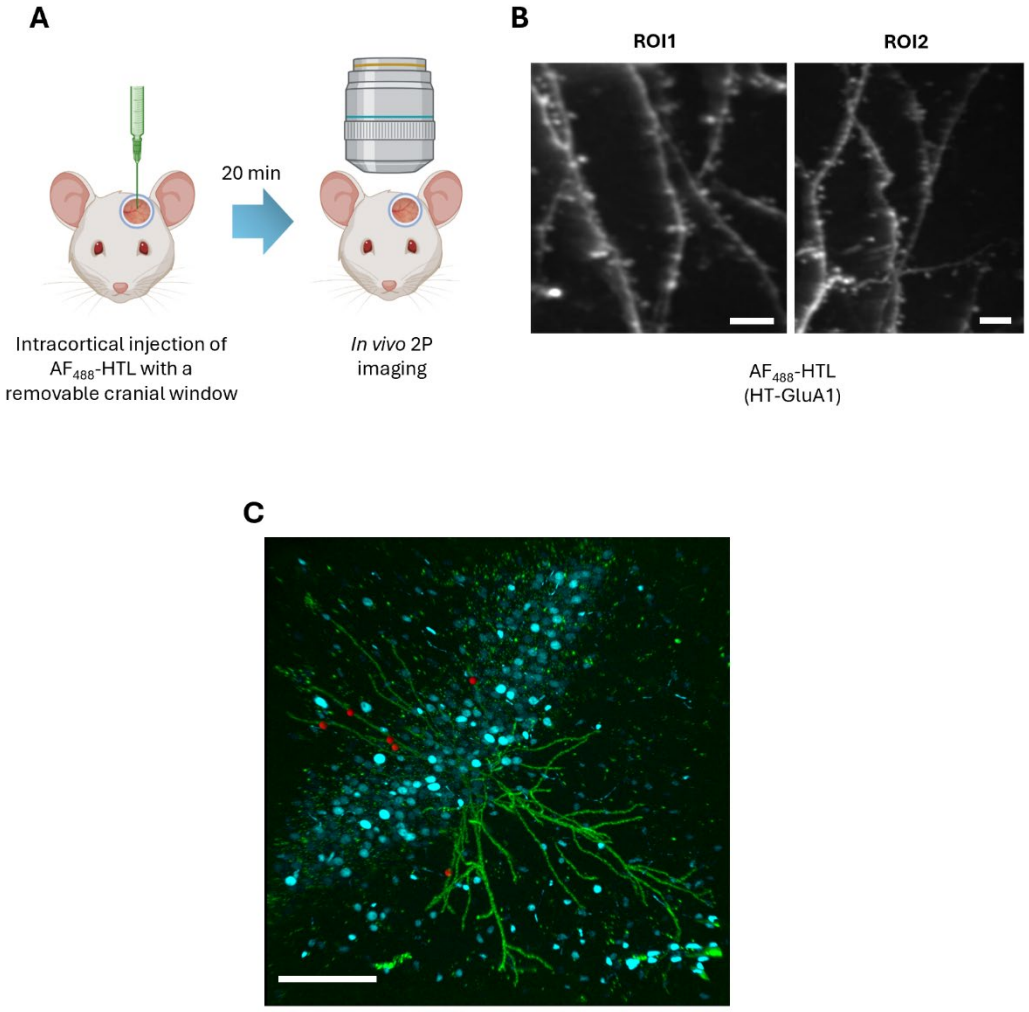

Figure 2.14: Possible extensions of the EPSILON technique. (a,b) Monitoring spine dynamics *in vivo*. **(a)** Experimental setup for intracortical injection of membrane-impermeable AF_{488}-HTL dye into mouse barrel cortex expressing HT-GluA1, followed by *in vivo* 2-photon imaging. **(b)** Representative *in vivo* 2-photon images of layer 2/3 pyramidal neuron apical tuft dendrites and spines stained with AF_{488}-HTL. This set of micrographs represents a single experiment. Scale bars, 5 µm. **(c)** Detecting new spine formation. New spines are expected to be labeled only with Dye 2, not Dye 1. Locations of the spines labeled with Dye 2 only are indicated with red dots. Neuron from **Figure 2.3c**. This micrograph represents a single experiment. See Methods for the detection of Dye 2 only spines. Scale bar, 200 µm. Part of (a) was created using Biorender and is used with permission.

2.7 Manuscript information

2.7.1 Previously published as

A version of this chapter appeared in [120]:

Kim, D., Park, P., Li, X., Campos, J. D. W., Tian, H., Moult, E. Grimm, J. B., Lavis, L., Cohen, A. E. Mapping memories: pulse-chase labeling reveals AMPA receptor dynamics during memory formation. Preprint at https://doi.org/10.1101/2023.05.26.541296 (2023).

This work is in press at *Nature Neuroscience*.

2.7.2 Acknowledgements

We thank Andrew Preecha and Shahinoor Begum for technical assistance. We thank Richard Huganir for sharing plasmids. We thank Michael Tadross, Ryohei Yasuda, Seth Grant, Boaz Mohar, Nelson Spruston, Karel Svoboda, and Bernardo Sabatini for helpful discussions. This work was supported by grants from Schmidt Futures, the Gordon and Betty Moore Foundation, and NIH grant 1-R21-EY033669. J. David Wong Campos is a Merck Awardee of the Life Sciences Research Foundation. Luke Lavis and Jonathan B. Grimm are supported by the Howard Hughes Medical Institute. The funders had no role in study design, data collection and analysis, decision to publish or preparation of the manuscript.

2.7.3 The author's contribution

Adam E. Cohen and Doyeon Kim conceived the project and designed the experiments. Doyeon Kim conducted the experiments and analyzed the data. Pojeong Park performed acute brain slice patch-clamp measurements. Xiuyuan Li contributed to molecular cloning. J. David Wong Campos, He Tian, and Eric M. Moult provided advice and technical support. Luke Lavis and Jonathan B. Grimm synthesized and provided the dyes used in this study. Doyeon Kim and Adam E. Cohen wrote the manuscript with input from all authors. Adam E. Cohen supervised the project.

3

Multicolor HaloTag labeling for mapping presynaptic dynamics

3.1 Abstract

Chemical synaptic transmission is essential for neuronal communication, yet tracking active synapses and their dynamics remains challenging. Here, we introduce a multicolor HaloTag labeling method that enables time-resolved tagging of activated presynaptic terminals both *in vitro* and *in vivo*. We developed Synaptophysin-HaloTag (Syp-HT) and vGluT1-HaloTag constructs that are selectively labeled with membrane-impermeable dyes upon presynaptic vesicle exocytosis. In cultured rat hippocampal neurons, optogenetic stimulation and chemical depolarization significantly increased labeling with a membrane-impermeable HaloTag dye, reflecting enhanced presynaptic vesicle release. In live mice, both optogenetic stimulation in anesthetized animals and sensory deprivation in awake, freely moving animals yielded clear and distinct labeling patterns in active presynaptic boutons. Moreover, sequential labeling with two different dyes exhibited a strong correlation between signals, suggesting low experimental variability and potential for further time-resolved studies. This method overcomes the limitations of traditional imaging by decoupling temporal resolution from spatial coverage, enabling synaptic dynamics mapping under natural conditions.

3.2 Introduction

Among the various ways neurons communicate, chemical synaptic transmission is one of the most thoroughly studied and remains a central focus in neuroscience[3]. In a

chemical synapse, an electrical signal is converted into a chemical message that is transmitted to another neuron, enabling flexible and precise communication. Neurotransmitters are stored within small vesicles at the presynaptic terminal and are released from specialized regions known as active zones[2]. This release can occur spontaneously or be triggered by action potentials, which open voltage-gated calcium channels[32]. The resulting influx of Ca^{2+} facilitates vesicle fusion and the release of neurotransmitters into the synaptic cleft, where they diffuse and bind to receptors on the postsynaptic neuron. The integration of these signals generates postsynaptic responses that underlie complex neuronal computations and ultimately drive behavior[3].

Mapping activated synapses is crucial for deciphering how neural circuits process information. To address this need, researchers have developed various techniques to monitor synaptic activity[121]. Real-time imaging of synaptic calcium, glutamate release, or vesicle fusion has been pursued using genetically encoded sensors such as GCaMP[122], iGluSnFR[15], or Synapto-pHluorin[123], respectively. However, the rapid kinetics of vesicle release and recycling—which occur on a millisecond timescale—require fast imaging[32]. Achieving this high speed often compromises the field of view and spatial resolution. In addition, most synaptic activity imaging has been performed in head-fixed animals, because the low numerical aperture of head-free miniscopes limits the study of neural processes in a naturalistic state[26]. Finally, the scattering properties of brain tissue make imaging synaptic dynamics in deep brain

areas challenging unless invasive techniques, such as the use of cannulas, are employed[22].

Another approach to mapping synaptic dynamics involves capturing neuronal signals *in situ* as fluorescent markers that can later be read *ex vivo*[27]. FM dyes, which incorporate into the plasma membrane, have been used to visualize presynaptic vesicle release and recycling[124]. However, their use is largely limited to cultured cells because of high background fluorescence, and they lack genetic specificity due to nonspecific binding to membranes[124]. To overcome these limitations, genetically engineered protein tags have been developed to label activated presynaptic terminals. For example, SynaptoZip[65] tags the C terminus of vesicle-associated membrane protein 2 with one part of a velcro coiled-coil heterodimer (the Zip module). Upon presynaptic vesicle exocytosis, a synthetic peptide called Synbond—the complementary component of the heterodimer—conjugated with a synthetic dye binds to the Zip module in the vesicle lumen, thereby labeling activated synapses with high specificity. However, due to its large size, the synthetic peptide used in SynaptoZip diffuses slowly through brain tissue and does not travel far from the injection site.

The HaloTag (HT) system offers an effective alternative because of its smaller ligand size, covalent binding nature, and the extensive library of commercially available ligands[69]. Consequently, a similar method using a HaloTag-fused vesicular gamma-aminobutyric acid (GABA) transporter has been developed[125]. Although HT

labeling of activated synapses holds the potential for multi-color sequential labeling[27]—which could reveal presynaptic dynamics at different time points—this approach has not yet been explored, to the best of our knowledge.

We recently developed a technique called EPSILON[120], a pulse-chase HT labeling method for potentiated spines, and used it to explore the *in vivo* sequential labeling of surface-exposed synaptic proteins with two different membrane-impermeable HaloTag-ligand (HTL) dyes. In this study, we generated Synaptophysin-HT and vesicular glutamate transporter 1 (vGluT1)-HT constructs and employed pulse-chase labeling with impermeable dyes to label activated presynaptic terminals. We confirmed that induced neuronal activity results in higher dye labeling at presynaptic boutons both *in vitro* and *in vivo*. Furthermore, we sequentially labeled the same presynaptic boutons with different colored dyes injected at distinct time points and found that the two dye signals are highly correlated under the same environmental conditions. This work represents the first proof-of-concept demonstrating the potential of this technique for labeling synaptic dynamics across multiple time points.

3.3 Results

3.3.1 Development and validation of HT labeling for presynaptic activity

We replaced the pH-sensitive GFP (SEP) domain in Synaptophysin-SEP[17] or vGluT1-SEP[18] with HT to generate Synaptophysin-HT (Syp-HT) and vGluT1-HT,

respectively (**Figure 3.1a**, see Methods for the detailed cloning process). In this design, HT resides in the vesicle lumen and can be labeled only by the membrane-impermeable HTL dye when it is exposed to the extracellular space during presynaptic vesicle release (**Figure 3.1b**). We initially tested the presynaptic dynamics labeling scheme in cultured rat hippocampal neurons to determine whether the pulse-chase labeled HT signal can serve as a proxy for presynaptic vesicle release.

We first tested whether optogenetically induced neuronal activity can induce HT dye labeling on axons. In cultured neurons co-transduced with a blue-shifted channelrhodopsin, CheRiff-eGFP[126] and either Syp-HT or vGluT1-HT, we first saturated the preexisting surface HT with Dye 1 (AF_{647}) in the presence of the blocker of excitatory transmission, 2,3-Dioxo-6-nitro-1,2,3,4-tetrahydrobenzo[f]quinoxaline-7-sulfonamide disodium salt (NBQX), and the sodium channel blocker TTX. Together, these compounds ensured minimal spontaneous activity during the pulse phase. After washing away the unreacted dye, NBQX, and TTX, we induced neuronal firing with pulsed 470-nm illumination while labeling with Dye 2 (JF_{549i}) (**Figure 3.1c**, Methods). We observed that a significantly larger fraction of presynaptic boutons were labeled with Dye 2 following 470-nm stimulation compared to the NBQX/TTX control without optogenetic stimulation, indicating that more HT molecules were exposed to the extracellular space during vesicle release and labeled with Dye 2 (**Figure 3.1d-f**, Syp-HT stimulated: 76 ± 19

bouton counts per cell, mean ± s.e.m., n = 37 neurons, 4 dishes; Syp-HT control: 7 ± 3 bouton counts per cell, mean ± s.e.m., n = 40 neurons, 4 dishes; P = 0.029; vGluT1-HT stimulated: 143 ± 26 bouton counts per cell, mean ± s.e.m., n = 27 neurons, 5 dishes; vGluT1-HT control: 12 ± 4 bouton counts per cell, mean ± s.e.m., n = 45 neurons, 3 dishes; P = 0.036, two-sided Wilcoxon rank-sum test). On the other hand, Dye 1 signal did not differ significantly among the groups (**Figure 3.1d-f**, Syp-HT stimulated: 29 ± 5 bouton counts per cell, mean ± s.e.m., n = 37 neurons, 4 dishes; Syp-HT control: 25 ± 6 bouton counts per cell, mean ± s.e.m., n = 40 neurons, 4 dishes; P = 0.89; vGluT1-HT stimulated: 10 ± 4 bouton counts per cell, mean ± s.e.m., n = 27 neurons, 5 dishes; vGluT1-HT control: 3 ± 1 bouton counts per cell, mean ± s.e.m., n = 45 neurons, 3 dishes; P = 0.57, two-sided Wilcoxon rank-sum test).

We further validated our technique by counting dye-labeled presynaptic boutons following extracellular potassium chloride (KCl) stimulation, which induces neuronal depolarization[127]. In neurons expressing either Syp-HT or vGluT1-HT, we first labeled the preexisting surface HT with Dye 1 (AF_{647}) in the presence of NBQX and TTX, then washed away the unreacted dye. Next, we induced presynaptic vesicle release by bath-applying KCl (100 mM, osmotically balanced) while labeling with Dye 2 (JF_{549i}) (**Figure 3.1f**, Methods). Upon KCl depolarization, we observed a robust increase in Dye 2-labeled presynaptic bouton counts (**Figure 3.1h-j**, Syp-HT stimulated: 85 ± 9 bouton counts per cell, mean ± s.e.m., n = 40 neurons, 5 dishes;

Figure 3.1 ***(following page)*****: Induced synaptic activity increases the dye-labeling levels of Syp-HT and vGluT1-HT *in vitro*. (a)** Composition of Syp-HT (Up) and vGluT1-HT (Bottom). Syp: Synaptophysin, HT: HaloTag receptor. **(b)** Experimental scheme for sequential labeling of surface-exposed presynaptic vesicular HaloTag using membrane-impermeable HTL dyes. Preexisting surface HaloTags are labeled with the first dye, followed by injection of a second dye to label newly exocytosed luminal HaloTags. The two populations are then analyzed using *ex vivo* multi-color imaging. **(c)** Timeline for presynaptic activity labeling during optogenetic stimulation. DIV: days *in vitro*. **(d)** Dye 1 and Dye 2 stained Syp-HT or vGluT1-HT expressing axons in cultured neurons under both optogenetic stimulation and control conditions. **(e-f)** Optogenetic stimulation does not change the number of puncta detected in the Dye 1 channel per neuron (e), but it increases the number in the Dye 2 channel **(f)**. Each data point represents a single culture dish. Lower and upper bounds of the box plot: 25th and 75th percentiles; lower and upper whiskers: minimum and maximum; and center lines: median. Two-sided Wilcoxon rank-sum test. **(g)** Timeline for presynaptic activity labeling during KCl stimulation. **(h)** Dye 1 and Dye 2 stained Syp-HT or vGluT1-HT expressing axons in cultured neurons under both KCl stimulation and control conditions. **(i-j)** KCl stimulation does not change the number of puncta detected in the Dye 1 channel per neuron **(i)**, but it increases the number in the Dye 2 channel **(j)**. Each data point represents a single culture dish. Lower and upper bounds of the box plot: 25th and 75th percentiles; lower and upper whiskers: minimum and maximum; and center lines: median. Two-sided Wilcoxon rank-sum test.

Figure 3.1: (Continued)

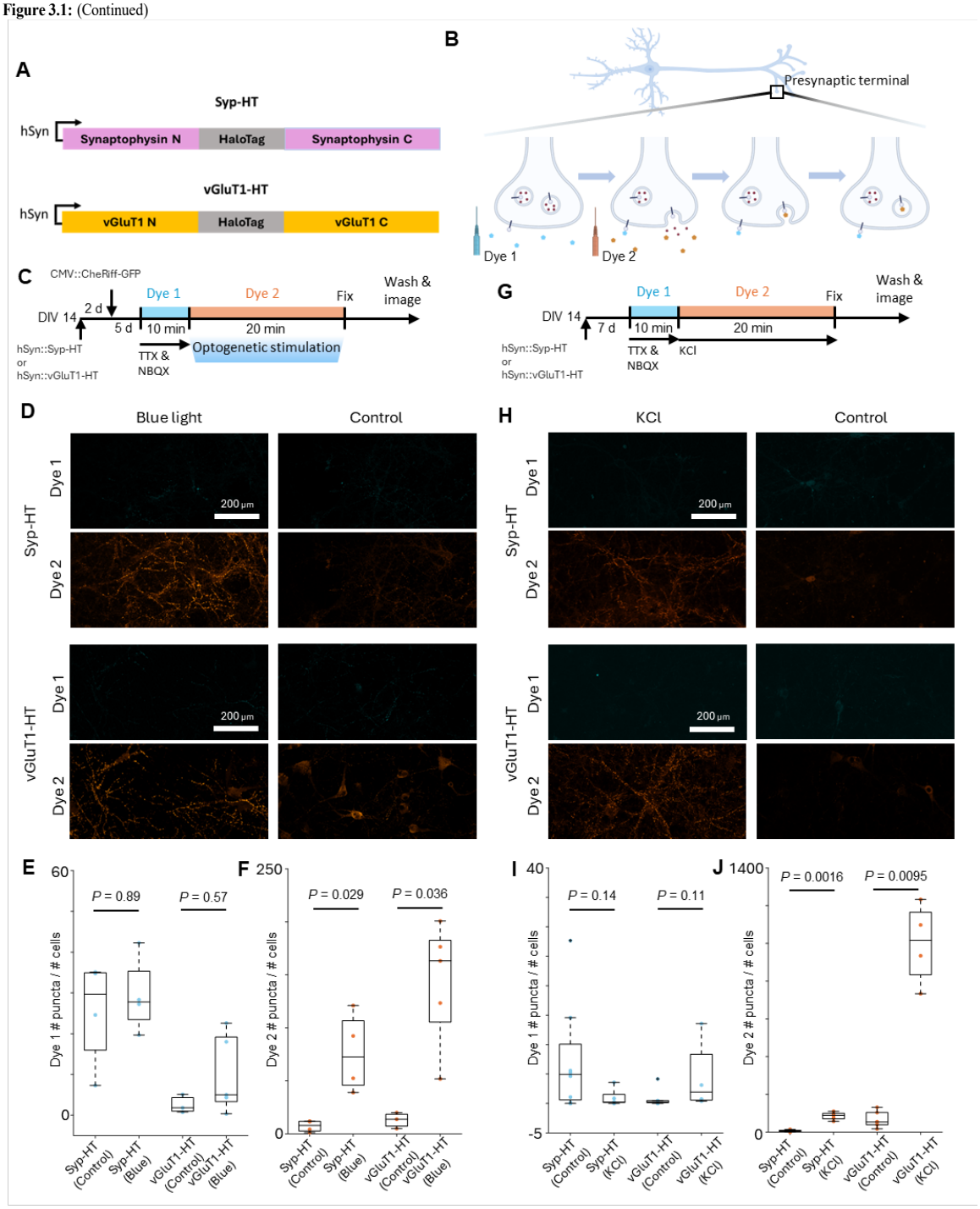

Syp-HT control: 7 ± 1 bouton counts per cell, mean ± s.e.m., n = 68 neurons, 8 dishes; P = 0.0016; vGluT1-HT stimulated: 1000 ± 108 bouton counts per cell, mean ± s.e.m., n = 24 neurons, 4 dishes; vGluT1-HT control: 66 ± 17 bouton counts per cell, mean ± s.e.m., n = 83 neurons, 6 dishes; P = 0.0095, two-sided Wilcoxon rank-sum test), while Dye 1-labeled bouton counts remained similar to those in the control group (Syp-HT stimulated: 1 ± 1 bouton counts per cell, mean ± s.e.m., n = 40 neurons, 5 dishes; Syp-HT control: 7 ± 3 bouton counts per cell, mean ± s.e.m., n = 68 neurons, 8 dishes; P = 0.14; vGluT1-HT stimulated: 4 ± 3 bouton counts per cell, mean ± s.e.m., n = 24 neurons, 4 dishes; vGluT1-HT control: 1 ± 1 bouton counts per cell, mean ± s.e.m., n = 83 neurons, 6 dishes; P = 0.11, two-sided Wilcoxon rank-sum test). Together, these results confirm that the HTL dye signal can reliably report the amount of presynaptic vesicle release at the single bouton level in cultured neurons.

3.3.2 *In vivo* characterization of presynaptic activity labeling at barrel cortex

To test our labeling scheme for presynaptic vesicle release in the live mouse brain, we cloned Syp-HT-P2A-LR-CheRiff-TS-EGFP-ER2 and expressed in layer 2/3 neurons of the mouse barrel cortex via *in utero* electroporation (IUE) (**Figure 3.2a**, see Methods for detailed cloning). We chose synaptophysin over vGluT1 to ensure broader applicability across neuronal types. EGFP, which serves as an axonal morphology marker, was modified with CheRiff, a Lucy-Rho tag, and an ER export motif to enhance membrane

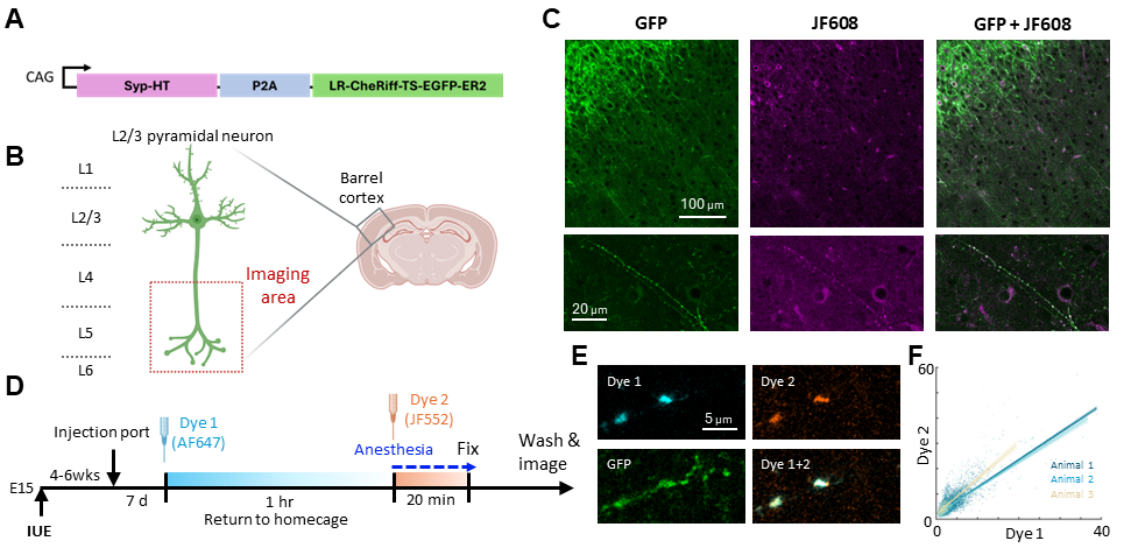

Figure 3.2: Multi-color HaloTag labeling of presynaptic synaptophysin pools in mouse barrel cortex. (a) Composition of Syp-HaloTag-P2A-LR-CheRiff-TS-EGFP-ER2. Syp: Synaptophysin, HT: HaloTag receptor, LR: a membrane localization signal from Lucy-Rho, TS: a trafficking sequence from $K_{ir}2.1$, ER2: endoplasmic reticulum export signal FCYENEV. **(b)** Ipsilateral axons of barrel cortex layer 2/3 pyramidal neurons in mice were imaged in the lower cortical layers, including layers 4, 5, and 6 on the fixed brain tissue. **(c)** Construct expression was checked in fixed tissue following intracranial JF_{608} injection. (Top) A coronal section shows the overall expression and trafficking pattern from layer 2/3 somata to downstream axons. (Bottom) An axon segment in layer 5 demonstrates CheRiff and HaloTag trafficking at presynaptic boutons. **(d)** Timeline for sequential labeling of activity-induced released and intracellular synaptophysin pools using a membrane-impermeable dye (AF_{647}) and a membrane-permeable dye (JF_{552}). E denotes embryonic age in days. **(e)** Axonal segment stained with membrane-impermeable Dye 1 (AF_{647}, cyan) and subsequently with membrane-permeable Dye 2 (JF_{552}, orange), coexpressing Syp-HT and membrane-trafficked EGFP (green). **(f)** Scatterplots of presynaptic bouton fluorescence intensities for membrane-impermeable (Dye 1) and membrane-permeable (Dye 2) dyes. Each data point represents a single presynaptic bouton, with different animals indicated by different colors. Least-squares linear regression was used to generate the fits, and dashed lines represent the 95% confidence intervals.

trafficking as previously described[12]. We confirmed that Syp-HT traffics to morphologically defined axonal boutons extending from layer 2/3 to deeper cortical layers (**Figure 3.2b, c**) in the ipsilateral hemisphere.

Next, we examined the relationship between activity-induced surface-exposed and internal synaptophysin pools *in vivo* (**Figure 3.2d**). We intracortically injected a membrane-impermeable dye (AF_{647}) into the barrel cortex and returned the animals to their home cages for 1 hour to label Syp-HT released during basal presynaptic activity. Subsequently, we injected a membrane-permeable dye (JF_{552}) into the same brain region to label the remaining Syp-HT (Methods). In fixed brain tissues, axonal boutons on ipsilaterally projecting axons from layer 2/3 to layer 6 were identified via the GFP channel, and the intensities of the impermeable and permeable dyes were quantified separately (Methods). The impermeable (released synaptophysin pool) and permeable (residing synaptophysin pool) dye intensities were highly correlated to each other for all animals (**Figure 3.2e, f**, animal 1: $R = 0.86$, $P = 0$, $n = 6{,}608$ boutons; animal 2: $R = 0.88$, $P = 0$, $n = 1{,}420$ boutons; animal 3: $R = 0.90$, $P = 1.7 \times 10^{-128}$, $n = 353$ boutons, R, Pearson's linear correlation coefficient, P value from two-sided Student's t-test). This correlation aligns with previous studies that suggest a relationship between presynaptic vesicle release and the total vesicle pool size at individual presynaptic terminals[2,128].

3.3.3 Presynaptic HaloTag labeling tags released vesicles *in vivo*

We triggered *in vivo* presynaptic vesicle release via optogenetic stimulation to determine

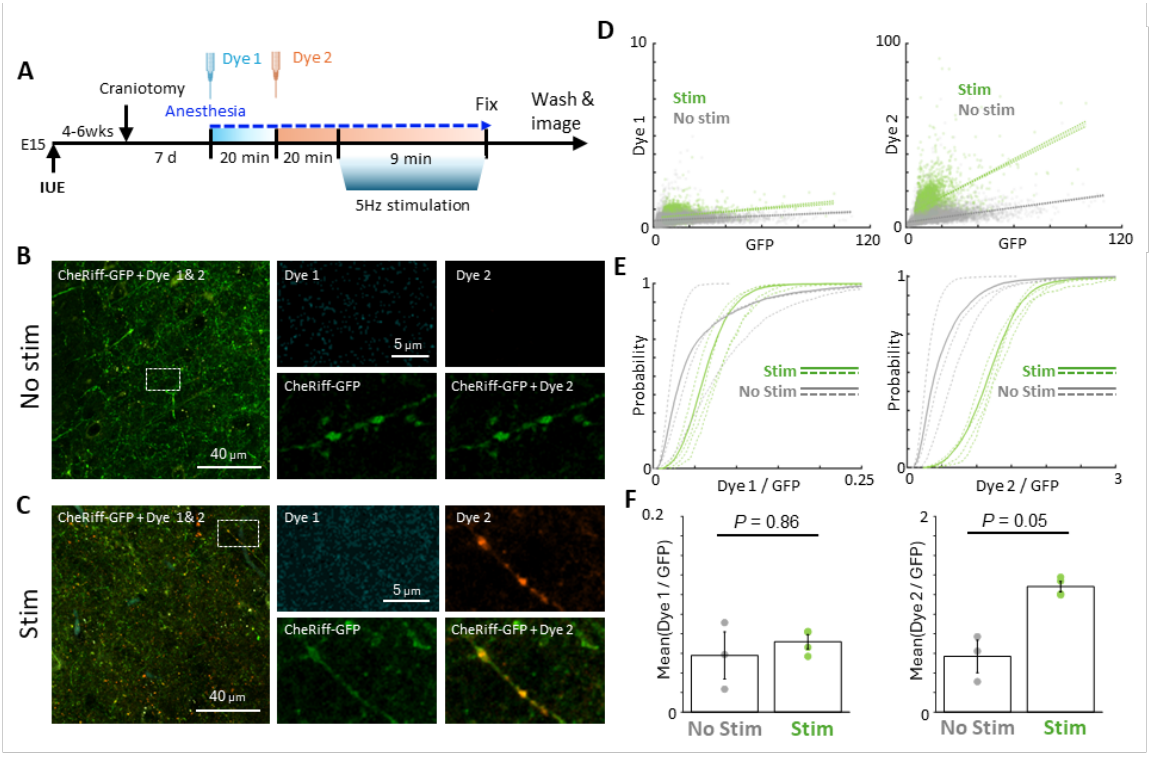

Figure 3.3: Optogenetically induced synaptic activity increases the dye-labeling levels of Syp-HT *in vivo*. **(a)** Timeline for labeling of released synaptophysin following optogenetic stimulation. **(b-c)** Layer 2/3 pyramidal neuronal axons were stained with membrane-impermeable Dye 1 (AF_{647}, cyan) under anesthesia and subsequently with another membrane-impermeable Dye 2 (JF_{549i}, orange) during optogenetic stimulation, while coexpressing Syp-HT and membrane-trafficked CheRiff-EGFP (green). **(b)** Control. **(c)** Stimulated. **(d)** Scatterplots showing the presynaptic bouton Dye 1 to GFP ratio (left) and Dye 2 to GFP ratio (right). Each data point represents a single presynaptic bouton. Least-squares linear regression was used to generate the fits, and dashed lines represent the 95% confidence intervals. **(e)** Cumulative distribution function (CDF) curves show the ratios of Dye 1 to GFP (left) and Dye 2 to GFP (right) for both the stimulated (green) and control (gray) groups. Dashed lines represent individual animals, while solid lines indicate the group averages. **(f)** Optogenetic stimulation does not change the mean Dye 1 to GFP ratio (left), but it increases the Dye 2 to GFP ratio (right). Each data point represents a single animal. In the box plots, the lower and upper bounds indicate the 25th and 75th percentiles, the whiskers show the minimum and maximum values, and the center lines mark the median. A two-sided Wilcoxon rank-sum test was used for statistical analysis.

whether our labeling scheme can tag active presynaptic boutons (**Figure 3.3a**). In mice expressing Syp-HaloTag-P2A-LR-CheRiff-TS-EGFP-ER2 in layer 2/3 of the barrel cortex, we installed a cranial window with an access port for intracortical dye injection and performed presynaptic vesicle labeling under light anesthesia (see Methods). 20 minutes after the Dye 1 (AF_{647}) injection, the animals received an intracortical injection of Dye 2 (JF_{548i}) along with an intraperitoneal injection of chlorprothixene to maintain the animals in a calm state while isoflurane levels were reduced for the subsequent procedure[120]. 20 minutes later, under light anesthesia, optogenetic stimulation was administered through the cranial window (470 nm, 5 Hz, 1800 repeats, see Methods for detailed stimulation parameters), and the animals were immediately sacrificed for fixed tissue preparation. Confocal imaging of ipsilateral axons from L2/3 pyramidal neurons in fixed brain sections revealed axonal boutons with an elevated Dye 2 signal upon optogenetic stimulation (**Figure 3.3b, c**). Analysis of individual boutons revealed an elevated Dye 2 to GFP ratio upon stimulation (**Figure 3.3d-f**, stimulated: mean Dye 2 to GFP ratio 1.3 ± 0.045, mean ± s.e.m., n = 7,077 boutons, 4 animals; control: mean Dye 2 to GFP ratio 0.57 ± 0.14, mean ± s.e.m., n = 7,035 neurons, 3 animals; P = 0.05, two-sided Wilcoxon rank-sum test), whereas the Dye 1 to GFP ratio did not differ statistically between the stimulated and control groups (stimulated: mean Dye 1 to GFP ratio 0.072 ± 0.0062, mean ± s.e.m.; control: mean Dye 1 to GFP ratio 0.058 ± 0.020, mean ± s.e.m.; P = 0.86, two-sided Wilcoxon rank-sum test). Together, these experiments and analyses illustrate how presynaptic vesicle labeling can map

presynaptic activity in individual boutons within a defined time window *in vivo*.

Next, we investigated whether sensory deprivation reduces presynaptic vesicle release and if this effect can be quantified using presynaptic vesicle labeling in awake, freely moving mice. We performed presynaptic vesicle tagging in mice expressing Syp-HaloTag-P2A-LR-CheRiff-TS-EGFP-ER2 in layer 2/3 of the barrel cortex while all contralateral whiskers were trimmed (**Figure 3.4a**). 20 minutes after the Dye 1 (AF_{647}) injection, the animals received an additional injection of Dye 2 (JF_{549i}). The mice were then returned to their home cages for 1 hour before being sacrificed for fixed tissue preparation. Confocal imaging of ipsilateral axons from layer 2/3 pyramidal neurons in fixed brain sections revealed that axonal boutons exhibited a reduced Dye 2 signal following whisker deprivation compared to the control group with intact whiskers (**Figure 3.4b, c**). Compared to mice with intact whiskers, the whisker-trimmed group exhibited a decreased Dye 2 to GFP ratio (**Figure 3.4d-f**, intact: mean Dye 2 to GFP ratio 0.88 ± 0.094, mean ± s.e.m., n = 26,050 boutons, 5 animals; trimmed: mean Dye 2 to GFP ratio 0.49 ± 0.11, mean ± s.e.m., n = 29,205 neurons, 5 animals; P = 0.05, two-sided Wilcoxon rank-sum test), whereas the Dye 1 to GFP ratio did not differ statistically between the two groups (intact: mean Dye 1 to GFP ratio 0.058 ± 0.0087, mean ± s.e.m.; trimmed: mean Dye 1 to GFP ratio 0.038 ± 0.0083, mean ± s.e.m.; P = 0.15, two-sided Wilcoxon rank-sum test). These results indicate that whisker deprivation reduces presynaptic activity in L2/3 pyramidal neurons, which can be observed and quantified using presynaptic vesicle tagging of synaptophysin in awake, freely moving

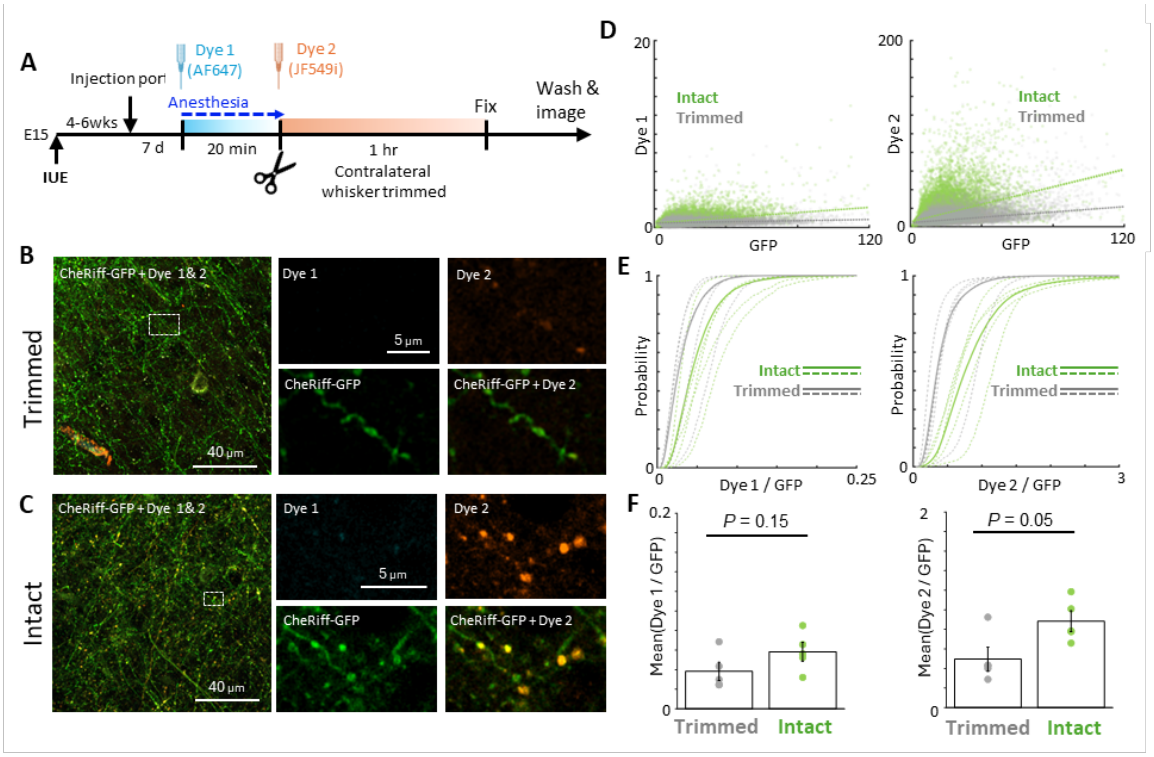

Figure 3.4: Sensory deprivation decreases the *in vivo* dye-labeling levels of Syp-HT in the barrel cortex. (a) Timeline for labeling of released synaptophysins following contralateral whisker deprivation. **(b-c)** Layer 2/3 pyramidal neuronal axons were stained with membrane-impermeable Dye 1 (AF_{647}, cyan) under anesthesia and subsequently with another membrane-impermeable Dye 2 (JF_{549i}, orange) during whisker deprivation, while coexpressing Syp-HT and membrane-trafficked CheRiff-EGFP (green). **(b)** Trimmed. **(c)** Intact. **(d)** Scatterplots showing the presynaptic bouton Dye 1 to GFP ratio (left) and Dye 2 to GFP ratio (right). Each data point represents a single presynaptic bouton. Least-squares linear regression was used to generate the fits, and dashed lines represent the 95% confidence intervals. **(e)** Cumulative distribution function (CDF) curves show the ratios of Dye 1 to GFP (left) and Dye 2 to GFP (right) for both the intact (green) and trimmed (gray) groups. Dashed lines represent individual animals, while solid lines indicate the group averages. **(f)** Whisker deprivation does not change the mean Dye 1 to GFP ratio (left), but it decreases the Dye 2 to GFP ratio (right). Each data point represents a single animal. In the box plots, the lower and upper bounds indicate the 25th and 75th percentiles, the whiskers show the minimum and maximum values, and the center lines mark the median. A two-sided Wilcoxon rank-sum test was used for statistical analysis.

animals. Together, these experiments and analysis illustrate how presynaptic vesicle labeling can map the presynaptic activities in individual boutons in a defined time window *in vivo*.

3.3.4 Repeated injections of membrane-impermeable dyes ensure that released vesicles are marked consistently, with no saturation observed

To assess whether the injected membrane-impermeable dye saturates the readily releasable pool (and thereby prevents subsequent labeling with a different colored dye), we performed a sequential labeling experiment. First, we intracortically injected impermeable Dye 1 (AF_{647}) into the barrel cortex and returned the animals to their home cages for 1 hour. Next, we injected impermeable Dye 2 (JF_{549i}) at a tenfold higher concentration into the same brain region to suppress the remaining Dye 1 labeling, and the animals were returned to their home cages for an additional hour (**Figure 3.5a**). Confocal imaging and the following dye intensity quantification at individual axonal boutons revealed a high correlation between Dye 1 and Dye 2 signals for all animals (**Figure 3.5b, c**, animal 1: $R = 0.94$, $P = 0$, $n = 736$ boutons; animal 2: $R = 0.95$, $P = 0$, $n = 3{,}078$ boutons; animal 3: $R = 0.88$, $P = 0$, $n = 2{,}357$ boutons; animal 4: R = 0.94, P = 0, $n = 2{,}547$ boutons, R, Pearson's linear correlation coefficient, P value from two-sided Student's t-test) indicating that Dye 1 did not saturate the entire readily releasable pool under these conditions. This result suggests that additional dyes can be employed to label active presynaptic boutons at multiple time points.

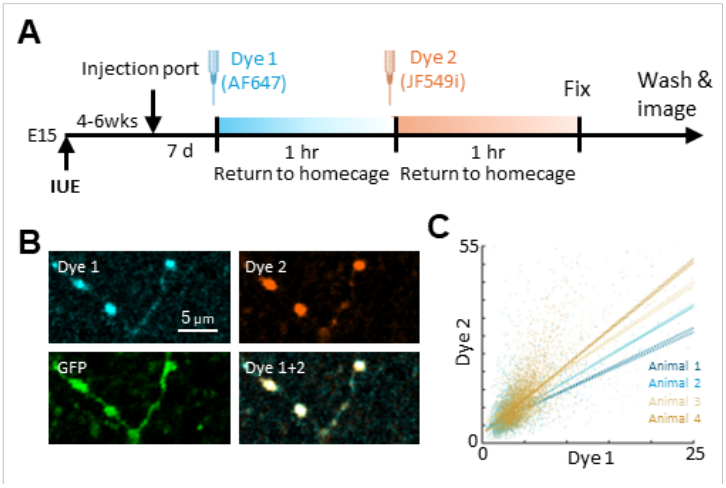

Figure 3.5: Sequential injections of membrane-impermeable dyes consistently label released vesicles without saturation. (a) Timeline for the sequential labeling of released synaptophysins using two membrane-impermeable dyes. **(b)** Layer 2/3 pyramidal neuronal axons were stained with the membrane-impermeable Dye 1 (AF647, cyan) and Dye 2 (JF549i, orange), while presynaptic boutons were identified using coexpressed, membrane-trafficked CheRiff-EGFP (green). Images were acquired from fixed tissue. **(c)** Scatterplots showing the presynaptic bouton Dye 1 and Dye 2 intensities. Each data point represents a single presynaptic bouton. Each solid line represents an individual animal. Least-squares linear regression was used to generate the fits, and dashed lines represent the 95% confidence intervals.

3.4 Discussion

Brain circuit identification is crucial for understanding how sensory information is processed and how higher cognitive functions, such as decision-making, occur[129]. Since neurons connect and communicate via chemical synapses and operate as part of networks, grasping both their structural and functional connections is key to identifying brain circuits[130]. Despite recent advances in mapping structural connectomes at the whole-brain level, functional connectomics is still emerging, with most studies focusing on the whole-cell level rather than on individual synapses[27].

Here, we demonstrate that HaloTag labeling enables mapping of activated synapses from different stimuli at various time points. We established the optimal conditions and parameters for implementing this labeling scheme in live mice. We observed increased dye-labeling signals from synaptophysin-HaloTag–expressing presynaptic boutons following optogenetic stimulation in anesthetized animals, and decreased signals following sensory deprivation in awake, freely moving animals. This demonstrates that the technique can be widely adopted to map activated synapses under various stimulus conditions. Additionally, we obtained reliable two-time-point labels in all animals, as the signals from the two sequentially injected dyes were highly correlated, indicating that potential experimental errors from dye injection and diffusion conditions are minimal.

There is still room for improvement with this technique. Although only two time points were tested in this study, the vast library of membrane-impermeable HaloTag ligands allows for the use of additional dyes—such as Alexa Fluor 488[131], which is spectrally

resolvable from AF_{647} and JF_{549i} used in this study. The intracranial cannula[132] can be used to deliver membrane-impermeable dyes across the whole brain without the need to anesthetize animals for injection. When combined with whole-brain transduction techniques[133] or transgenic mouse lines[134], this approach offers a way to map functional circuit dynamics at the whole-brain level.

There are several potential applications for this technique beyond mapping active synaptic circuits and their dynamics. For instance, when combined with various optogenetic stimulation patterns that elicit different neuronal outputs, one can study the spatial distribution of axonal outcomes from simple and complex spikes by tracking entire axons in fixed slices after inducing distinct spike patterns[12]. Another promising approach is to combine this technique with postsynaptic labeling methods, such as EPSILON for potentiated spines[120]. By labeling both presynaptic activity and postsynaptic plasticity, one can thoroughly investigate the relationship between these two processes—for example, determining whether grouped potentiation arises from spatially clustered presynaptic inputs[102] or from the diffusion of postsynaptic second messengers[103].

Overall, the multi-point labeling approach for presynaptic vesicle release presented here expands the toolbox of functional synaptic circuit mapping techniques. Combined with state-of-the-art optogenetic[135] and chemigenetic[13] methods for neuronal activity mapping and modulation, this approach could provide insights into the fundamental rules of neuronal networks as well as the neurodegenerative diseases associated with synaptic dysfunction.

3.5 Methods

3.5.1 Animals

All experiments were performed on 8-12 week-old male and female CD-1 mice purchased from Charles River Laboratories. All animal procedures were in accordance with the US National Institutes of Health *Guide for the Care and Use of Laboratory Animals* and were approved by the Institutional Animal Care and Use Committee at Harvard University.

3.5.2 DNA constructs

Standard methods of molecular cloning were used to create the constructs. Plasmids and sequences created for this project are available upon request.

pAV001: Synaptophysin-HaloTag (abbreviated Syp-HT), driven by human synapsin 1 gene (hSynI) promoter.

Plasmid pAV001 was assembled from three fragments: synaptophysin fragment 1 (N terminus to the third transmembrane region), the HaloTag protein, and synaptophysin fragment 2 (fourth transmembrane region to C terminus). Synaptophysin fragment 1 and 2 were amplified from CMV::SypHy A4[17] (Addgene 24478). HaloTag was amplified from hSynI::HaloTag-GluA1 (Addgene 192517). The fragments were assembled together with Gibson Assembly[113] and cloned into pLenti hSynI vector (HT075 from[114]). As a result, HaloTag replaced pHluorin of SypHy and is inserted at an intralumenal loop.

pAV002: vGluT1-HaloTag (abbreviated vGluT1-HT), driven by human hSynI promoter.

Plasmid pAV001 was assembled from three fragments: vGluT1 fragment 1 (N terminus to the first intralumenal loop), the HaloTag protein, and vGluT1 fragment 2 (first intralumenal loop to C terminus). vGluT1 fragment 1 and 2 were amplified from CAG::vGluT1-pHluorin[18], a gift from Susan Voglmaier. HaloTag was amplified from hSynI::HaloTag-GluA1 (Addgene 192517). The fragments were assembled together with Gibson Assembly[113] and cloned into pLenti hSynI vector (HT075 from[114]). As a result, HaloTag replaced pHluorin of vGluT1-pHluorin and is inserted at an intraluminal loop.

pDK039: Synaptophysin-HaloTag-P2A-LR-CheRiff-TS-EGFP-ER2, driven by CAG promoter to coexpress Synaptophysin-HT with a blue-shifted channelrhodopsin, CheRiff by a self-cleaving p2a linker. To optimize expression and dendritic membrane trafficking, LR, a membrane localization signal from Lucy-Rho[136], TS, a trafficking sequence from $K_{ir}2.1$[137], and ER2, endoplasmic reticulum export signal FCYENEV[137], were included as previously described[12].

Plasmid pDK039 was assembled from three fragments: Synaptophysin-HT, p2a-LR-CheRiff-TS, and eGFP-ER2. Synaptophysin-HT was amplified from pAV001. p2a-LR-CheRiff-TS was amplified from CAG::LR-Voltron2-TS-ER2-p2a-LR-CheRiff-TS-eYFP-ER2 (Addgene 203228). eGFP-ER2 was amplified from CaMKII::QuasAr2-TS-eGFP-ER2 (lab stock). The fragments were assembled together with Gibson Assembly[113] and cloned into pLenti hSynI vector (HT075 from[114]).

3.5.3 Primary neuron culture

Glass-bottom dishes (14 mm) were first treated with 40 μg ml^{-1} poly-D-lysine (PDL) in phosphate-buffered saline (PBS) at room temperature for 1 h. They were then incubated overnight at 4 °C with 20 μg ml^{-1} laminin (Thermo Fisher Scientific, 23-017-015). After extensive PBS washes, hippocampi were isolated from embryonic day 18 (E18) rats and suspended in BrainPhys medium (BPNM, STEMCELL Technologies, 05790) supplemented with 2% SM1 (STEMCELL Technologies, 05792), 5 mM L-glutamine (STEMCELL Technologies, 07100), and 35 μg ml^{-1} L-glutamic acid (Sigma-Aldrich, 49449) to achieve a final cell concentration of 3.0 x 10^6 cells ml^{-1}. The neurons were then plated at 30,000 cells cm^{-2} onto the prepared dishes, and 2 ml of BPNM with 2% SM1 (BPNM/SM1) was added. Neuronal health was observed daily from DIV1 to DIV7, and the culture medium was replaced with fresh, pre-warmed (37 °C) BPNM/SM1 every 3–4 days.

3.5.4 Virus packaging

Lentiviruses produced in-house using a second-generation packaging system were employed in this study. Detailed protocols for their production and packaging have been described previously[71].

3.5.5 Lentiviral transduction of cultured neurons

The hSyn::Syp-HT and hSyn::vGluT1-HT vectors were introduced to the neurons via lentiviral transduction at DIV14. For optogenetic stimulation, CMV::CheRiff-eGFP

(Addgene 178821) vector was additionally introduced to the neurons via lentiviral transduction at DIV 16. The lentiviral vectors were added directly to the neuronal cultures in fresh BPNM/SM1 medium. The neuronal cultures were then incubated with the lentivirus-containing medium for 12 hours at 37 °C and 5% CO_2, followed by a medium replacement with lentivirus-free medium. Experiments were conducted at DIV 21.

3.5.6 HaloTag labeling in cultured neurons under optogenetic stimulation

Cultured neurons coexpressing CheRiff-eGFP and either Syp-HT or vGluT1-HT at DIV21 were washed twice with wash buffer (Tyrode solution containing 10 µM NBQX and 0.3 µM TTX). They were then exposed to 1 µM Dye 1 (AF_{647}-HTL) in wash buffer at 37 °C and 5% CO_2 for 1 minute. After two additional washes with wash buffer, the neurons were incubated in Tyrode solution supplemented with 1 µM Dye 2 (JF_{549i}-HTL) for 3 minutes. During the Dye 2 incubation, the neurons were optogenetically stimulated with blue light (470 nm, irradiance: 3.5 mW/mm^2). The stimulus waveform consisted of nine sets of 1 Hz pulses with a 50% duty cycle for 10 seconds, followed by a 10-second rest between each set. After two further washes with wash buffer, the neurons were fixed with 4% paraformaldehyde. The fixed cultures were subsequently washed in PBS for 24 hours. Negative control cultures were treated with Tyrode solution containing 10 µM NBQX, 0.3 µM TTX, and Dye 2, without optogenetic stimulation. All media were pre-incubated in 5% CO_2 for 30 minutes and heated to 37 °C prior to use.

Experiments were performed on a custom-built fluorescence microscope equipped with

a 470 nm light-emitting diode. Optogenetic stimulation was delivered through a 1x objective lens (Olympus MVPLAPO 1X, numerical aperture 0.25). Illumination intensity and timing were controlled using custom MATLAB code via a National Instruments DAQ interface.

3.5.7 HaloTag labeling in cultured neurons during KCl-depolarization

Cultured neurons expressing Syp-HT or vGluT1-HT at DIV21 were washed twice with wash buffer (Tyrode solution containing 10 μM NBQX and 0.3 μM TTX). They were then exposed to 1 μM Dye 1 (AF_{647}-HTL) in wash buffer at 37 °C and 5% CO_2 for 1 minute. After two additional washes with wash buffer, the neurons were incubated in stimulation buffer (osmotically balanced Tyrode solution with 100 mM KCl) supplemented with 1 μM Dye 2 (JF_{549i}-HTL) for 10 minutes. Following two more washes with wash buffer, they were fixed with 4% paraformaldehyde. The fixed cultures were subsequently washed in PBS for 24 hours. Negative control cultures were treated with Tyrode solution containing 10 μM NBQX, 0.3 μM TTX, and Dye 2. All media were pre-incubated in 5% CO_2 for 30 minutes and heated to 37 °C prior to use.

3.5.8 *In utero* electroporation

Progenitor cells in the embryonic mouse brain's layer 2/3 were transfected via *in utero* electroporation. Pregnant CD-1 mice were used, and a DNA solution containing Fast Green was injected into each embryo's lateral ventricle using a pulled-glass pipette. Five-

mm platinum electrodes, angled to target the left barrel cortex, delivered the electrical pulses. The electroporation protocol consisted of five pulses at 35 V, with each pulse lasting 50 ms at a frequency of 1 Hz. The DNA solution contained 1 μg/μL of pDK039.

3.5.9 Cranial window surgery

CD-1 mice (8–10 weeks old) expressing pDK039 via *in utero* electroporation were anesthetized with a ketamine/dexmedetomidine solution (77 mg/kg and 0.33 mg/kg, respectively) and secured in a stereotaxic apparatus. A craniotomy approximately 3 mm in diameter was performed over the left barrel cortex of the exposed skull (AP: 3.3–3.4 mm lateral, 1.6 mm posterior from bregma) using a dental drill. A round glass window with a 0.35 mm × 0.35 mm square hole, positioned 0.6 mm from the center, was placed over the craniotomy and affixed to the skull with dental cement (C&B Metabond). The hole was sealed with silicone gel (KWIK-CAST silicone sealant, WPI). Following recovery from anesthesia, the mice were returned to their home cages and received carprofen (5 mg/kg) and buprenorphine (0.1 mg/kg) on post-surgery days 0, 1, and 2. The cranial window design used in this experiment was adapted from previously published protocols[114,116].

3.5.10 Installation of dye injection port

Male or female CD-1 mice expressing pDK039 through *in utero* electroporation, aged 8–10 weeks, were selected and anesthetized with a ketamine/dexmedetomidine solution. A heating pad (WPI, ATC2000) was placed under each mouse to maintain a body

temperature of 36–37 °C, and ophthalmic ointment was applied to keep their eyes moist. The surgical coordinates for the left barrel cortex were identified as described previously[120]. A hollow titanium ring (outer diameter: 5 mm, inner diameter: 2.1 mm, thickness: 0.35 mm) was then attached around these coordinates on the skull using dental cement (C&B Metabond, Parkell, No. 242-3200). Holes were drilled through the skull until only a thin layer (approximately 20 μm) remained, and the titanium ring was filled with silicone gel, which was removed prior to dye injection and refilled afterward. After recovering from anesthesia, the mice were returned to their home cages.

3.5.11 Sequential HaloTag labeling in live animals

One week after installing the injection port over the barrel cortex, the mice were anesthetized with isoflurane and placed on a surgical platform. At each of the previously described injection points on the barrel cortex[120], 80 nL of Dye 1 (AF_{647}-HTL, 1 μM) was injected at a rate of 100 nL/min. The mice were then returned to their home cages. One hour later, the mice were anesthetized again with isoflurane, and 80 nL of Dye 2 (JF_{552}-HTL for **Figure 3.2** or JF_{549i}-HTL for **Figure 3.5**, 10 μM) was injected at the same injection points and with the same parameters as Dye 1. JF_{552}-injected animals remained under anesthesia for 20 minutes after Dye 2 injection before being euthanized and prepared for brain slicing. For JF_{549i}-injected animals, after an additional hour in their home cages, the mice were euthanized and prepared for brain slicing.

3.5.12 HaloTag labeling in live animals under optogenetic stimulation

One week after cranial window surgery, the mice were returned to the surgical stage and placed under less than 2% isoflurane anesthesia. The silicone gel was carefully removed, and 1 μM of Dye 1 (AF_{647}-HTL) was injected through the hole at a rate of 100 nL/min—delivering 100 nL at each depth in 0.1 mm increments from 1 mm down to the cortical surface. After the Dye 1 injection, 2.7 mg/kg of chlorprothixene hydrochloride (dissolved in PBS) was administered intraperitoneally, and the isoflurane level was reduced to below 0.5% for the remainder of the experiment. 20 minutes after the completion of the Dye 1 injection, 10 μM of Dye 2 (JF_{549i}-HTL) was injected using the same parameters. 20 minutes after the Dye 2 injection, neurons expressing CheRiff were optogenetically stimulated with blue light (470 nm, irradiance: 0.21 mW/mm^2) from a light-emitting diode. The stimulation protocol consisted of three sets of 5 Hz pulses with a 50% duty cycle for 2 minutes, with a 1-minute rest between each set. After optogenetic stimulation, the mice were euthanized and prepared for brain slicing.

3.5.13 HaloTag labeling in live animals under sensory deprivation condition

One week after installing the injection port over the barrel cortex, the mice were anesthetized with isoflurane and placed on a surgical platform. At each of the previously described injection points on the left barrel cortex[120], 80 nL of dye 1 (AF_{647}-HTL, 1 μM) was injected at a rate of 100 nL/min. 20 minutes after the dye 1 injection, all contralateral whiskers were trimmed, and 80 nL of dye 2 (JF_{549i}-HTL, 10 μM) was injected at the same points using the same parameters. The mice were then returned to their home cages for 1

hour before being euthanized and prepared for brain slicing. For the control group, the whiskers remained intact throughout the experiment.

3.5.14 Slice preparation for confocal imaging

Mice were euthanized by isoflurane overdose until breathing ceased, and their brains were promptly extracted. The brains were then sectioned into 150 μm-thick coronal slices using a vibratome (Leica, VT1200S) and fixed in 4% paraformaldehyde at 4 °C for 24 hours. After fixation, the slices were washed in PBS on a shaker at room temperature for 48 hours. Finally, the sections were mounted with VECTASHIELD PLUS Antifade Mounting Medium (Vectorlabs, H-1900-10) for confocal imaging.

3.5.15 Confocal imaging of Syp-HT or vGluT1-HT expressed in cultured rat hippocampal neuron

Fixed neuron cultures were imaged on a confocal microscope (LSM 980) using a 20× water immersion objective. The AF_{647} and JF_{549i} fluorophores were excited with 639-nm and 561-nm lasers, respectively. Each image had a pixel resolution of 0.052 μm × 0.052 μm, and the region of interest measured 424.27 μm × 424.27 μm (8192 × 8192 pixels). A pixel dwell time of 0.51 μs was used, and these imaging parameters were consistently applied in all experiments.

3.5.16 Confocal imaging of Syp-HT or vGluT1-HT expressed in brain slice

Confocal images of fixed brain slices were acquired using LSM 980 with 63× oil immersion objective in z-stack. EGFP, JF_{552}, JF_{549i}, and AF_{647} were excited with 488-nm, 561-nm, 561-nm, 639-nm lasers, respectively. Non-specific autofluorescent artifacts were excited with 488-nm and the detection ranges were from 641-nm to 694-nm. Voxel sizes were 0.085 μm by 0.085 μm by 0.46 μm. Pixel time was 0.50 μs for all experiments. The same imaging conditions were used for all samples within each set of experiments.

3.5.17 Image processing and data analysis

MATLAB, ImageJ, and Imaris were employed for processing the images. A 2D Gaussian filter was applied to denoise all images before analysis, using the same kernel sizes for each dataset within an experimental set. For axonal varicosity segmentation, z-stack images were segmented based on the GFP channel using Imaris and custom MATLAB code. The locations of varicosity were determined by using the Imaris spot detection function in GFP channel (threshold: 'quality' above 2.6). Autofluorescent artifacts were identified by their intensities in the 'autofluorescence detection channel' (threshold: 'quality' above 0.9). Spots within 2 mm of the center of an autofluorescent artifact were excluded from analysis. The same parameters were used throughout all experiments that required varicosity detection. Then, a 2.6 μm by 2.6 μm by 2.8 μm image subset was defined around each initial varicosity location. A binary mask was generated for each image subset using the Otsu algorithm. Next, a Euclidean distance transform was applied, followed by an extended minima transform. To remove small local minima, the MATLAB

function imextendedmin was used, and the remaining minima were then integrated into the original binary mask. The Watershed algorithm was used to segment the resulting binary masks. Any masked area with an x-y centroid coordinate offset by more than 0.6 μm from the center of the image subset and a circularity index smaller than 0.75 was excluded from the analysis. Background autofluorescence was calculated as the mean intensity of each non-masked area from the first Otsu thresholding. Background was subtracted from the mean intensity value within each masked area.

3.6 Manuscript information

3.6.1 The author's contribution

Doyeon Kim and Adam E. Cohen conceived this work. Doyeon Kim conducted experiments and analyzed the data. Ariana-Dalia Vlad contributed to molecular cloning. Doyeon Kim and Adam E. Cohen wrote the manuscript. Adam E. Cohen supervised the work.

4

Conclusion

This dissertation introduced two techniques for labeling synapse dynamics, based on HaloTag staining. One technique labels postsynaptic plasticity dynamics, while the other targets presynaptic vesicle release. Both techniques share the principle of sequentially tagging surface-exposed membrane proteins with membrane-impermeable synthetic dyes. This approach provides a means to record the history of synaptic dynamics *in vivo* and subsequently read it out *ex vivo*, thereby overcoming some limitations of real-time *in vivo* imaging.

In Chapter 1, I discussed the importance of mapping *in vivo* synaptic dynamics and plasticity, the shortcomings of current methods, and the concept of molecular recorders

for *in situ* labeling of cellular activities. To adapt the idea of molecular recorders for capturing synaptic dynamics, I described the molecular mechanisms underlying synaptic transmission and plasticity, as well as recent advances in HaloTag labeling techniques, all of which contributed to the development of these new synaptic dynamics labeling tools.

In Chapter 2, I introduced a pulse-chase labeling technique called EPSILON for the selective capture of potentiated spines, which maps both the location and the extent of synaptic plasticity across an entire neuron *in vivo*. Using this technique, I sought to elucidate the relationship between cell-level and synaptic-level memories by correlating immediate early gene expression with synaptic plasticity levels. Nevertheless, many important neuroscientific questions remain that could be addressed using this approach. Here, I propose several of these questions along with possible approaches employing EPSILON.

Different types of memory may exhibit distinct spatial patterns of potentiated synapses, depending on each memory's primary function[138]. For example, a random arrangement of potentiated synapses might enhance the precision of memory recall, whereas clustered potentiation can amplify dendritic inputs in a nonlinear manner—allowing action potentials to be triggered by relatively few synaptic inputs. Such modalities could be advantageous for memories that require a fast response, such as fear memory. Since I observed clustered potentiation during the encoding of contextual fear memory, the next step is to label potentiated spines under a paradigm that requires

precise memory formation, such as a sophisticated motor learning procedure[139], and determine whether this paradigm results in a differently distributed spatial pattern of synaptic potentiation.

How about the synaptic plasticity dynamics in different cell types? Different types of neurons receive inputs from various brain regions and likely employ different dendritic integration mechanisms[140,141]. For instance, layer 2/3 and layer 5 pyramidal neurons in the primary motor cortex exhibit distinct morphological and electrophysiological properties[142], and it has been reported that their synaptogenesis rates at the apical tuft dendrites differ during the same motor learning process, suggesting that their synaptic plasticity rules are different[143]. Although most *in vivo* synaptic plasticity studies have focused on apical tuft dendrites of a single neuronal type due to limitations in live imaging, EPSILON can precisely map synaptic plasticity patterns across different neuronal types within the same animal by tracking each dendrite in fixed brain tissue after expressing HT-GluA1 across multiple cortical layers via AAV transduction[133] or by performing multilayer *in utero* electroporation[144].

The current study used two different colors to separately label preexisting and newly exposed AMPARs, thereby mapping synaptic plasticity for a single memory event. Adding another color could help address questions regarding the synaptic mechanisms underlying overlapping neuronal ensembles[92]—for example, whether there is a spatial correlation between potentiated synapses in the overlapping engram for two linked memories. Although Sehgal et al. showed that memories formed in close temporal

proximity add new spines to the same dendrites that were targeted during the formation of an earlier memory in the retrosplenial cortex (RSC), their study did not account for the potentiation of preexisting spines—likely due to the low spatial resolution of miniscope imaging—and focused solely on the apical tuft dendrites of layer 5 RSC neurons[145]. Labeling the potentiated spines during the second memory formation using EPSILON labeling would enable detailed investigation of this phenomenon, regardless of the brain region, neuron type, or specific subregions of the neurons.

The current version of the EPSILON technique labels synaptic potentiation by staining exocytosed AMPARs but does not capture synaptic depression associated with vesicle endocytosis. If a pH-sensitive HaloTag ligand that binds HaloTag only under acidic conditions were developed, a similar principle could be applied to label depressed spines: the preexisting intracellular pool of AMPARs would be labeled with the first dye, while endocytosed AMPARs—exposed to the acidic environment of endocytic vesicles—would be labeled with the second dye. This approach could enable the study of *in vivo* long-term depression (LTD) dynamics in relation to memory loss.

In Chapter 3, I introduced another HaloTag labeling technique for presynaptic vesicle release. Using this technique, I demonstrated that it is possible to selectively map active presynaptic boutons both *in vitro* and *in vivo*. In live mice, presynaptic vesicle release induced by optogenetic stimulation under light anesthesia—as well as under natural conditions in awake animals—was successfully captured. These results have two main implications.

First, this technique can be used to map the functional connectome across the whole brain. In the short-term presynaptic plasticity model established in brain slices[146], the presynaptic activity pattern and the initial release probability of each bouton determine the subsequent dynamics of release probability[147]. This effect varies across different cell types[148] and along the distance from the soma to the target dendrite[149]. Various factors—including the types of calcium channels present[150], the organization of active zones[151], the size of the readily releasable vesicle pool[146], and the local calcium buffering capacity[152]—are thought to influence these dynamics. However, detailed *in vivo* studies have not been conducted due to current limitations in measuring release probability.

Since the technique introduced here can map *in vivo* release probability at multiple time points, one can envision applying different optogenetic stimulus patterns that evoke distinct spiking forms in target neurons[12] and then labeling the presynaptic vesicle release for each pattern *in vivo*. The resulting presynaptic vesicle release can be tracked—using different colors for different stimuli—along entire axons *ex vivo*, or analyzed in more detail regarding the physicochemical properties of each labeled presynaptic bouton using correlative electron microscopy[153] or immunohistochemistry with expansion microscopy[154]. Such experiments would provide additional information about functional synaptic transmission patterns, complementing the structural connectomes currently under construction[155].

Second, the balance of synaptic excitation (E) and inhibition (I) is tightly regulated,

and disruptions in E/I balance have been implicated in various neurological and psychiatric disorders[156]. Current techniques, such as multi-electrode arrays[118], *in vivo* patch-clamp[157], and calcium imaging[158], generally provide information at the network or whole-cell level but do not reveal the synaptic origins of this balance and its dynamics. Here, I propose expressing a Syp-HT construct in both inhibitory and excitatory neurons, using different colored morphological markers (e.g., GFP and mCherry) to separately resolve presynaptic vesicle release from distinct presynaptic sources. For example, one could express Syp-HT-P2A-mCherry in GABAergic interneurons[159] and Syp-HT-P2A-GFP in pyramidal neurons, and then label the presynaptic vesicle release during critical developmental periods[160] under various conditions (e.g., sensory deprivation). Then, the dynamics of each synapse can be analyzed separately in inhibitory and excitatory synapses by registering the dye signal to the structural fluorescent marker, which varies in color depending on the cell type. This approach would allow us to spatially map the development of E/I balance at the single-synapse level.

Combining these two techniques would offer a more powerful means to study the relationship between synaptic activity and plasticity. However, one obstacle to their simultaneous use is that they are not orthogonal, as both rely on HaloTag. This issue might be overcome by replacing HaloTag in EPSILON with another orthogonal self-labeling protein domain[161] whose slower labeling kinetics may be acceptable for tagging newly exocytosed, membrane-residing AMPARs. If presynaptic activity and

postsynaptic plasticity can be labeled simultaneously, their *in vivo* relationships can be studied. For example, in Chapter 2, clustered synaptic plasticity was observed during contextual fear memory formation in CA1 pyramidal neurons. By co-labeling the corresponding presynaptic activities, one could investigate whether the clustered spines receive presynaptic inputs within the same time window[102], or whether only one spine receives presynaptic input and diffusion of small molecules to nearby spines drives the observed clustering[103].

Both techniques have the potential to map neuronal circuits across the entire brain using brain-wide AAV transduction or transgenic lines. In fact, a transgenic mouse line for HT-GluA2 has recently been developed and used to map AMPAR turnover throughout the brain[75]. However, since the labeling techniques for presynaptic activity and postsynaptic plasticity both require the infusion of membrane-impermeable dyes—which do not cross the blood–brain barrier—alternative approaches must be employed to deliver these dyes for comprehensive synapse mapping. Intracerebroventricular cannulation[132] is one possible method for achieving brain-wide delivery of these dyes, although it is essential to carefully characterize the dye's diffusion kinetics and profiles in different brain regions.

The current HaloTag labeling techniques rely on fluorescent dye–conjugated HaloTag ligand molecules. Despite the vast library of available fluorescent dye conjugates, the number of measurable time points remains limited due to spectral overlap. Although temporally multiplexed imaging[162] can slightly expand this capacity,

it does not dramatically overcome the limitation. In contrast, using DNA or RNA probes followed by *in situ* transcriptomic readout can expand the readout capacity beyond these spectral constraints. For example, nucleic acid–conjugated HaloTag ligands with unique sequences can be applied at different time points, and the *ex vivo* readout can be performed using Multiplexed Error-Robust Fluorescence *In Situ* Hybridization (MERFISH)[163] or Sequential Fluorescence *In Situ* Hybridization (seqFISH)[164], both of which enable the detection of hundreds to thousands of nucleic acid probes. Of course, the intrabrain diffusion kinetics of these nucleic acid conjugates—which are heavier than conventional synthetic fluorescent dyes—should be carefully characterized.

In addition, both techniques described here are limited by spontaneous protein turnover, as dye-labeled proteins are gradually degraded and newly synthesized proteins can also become labeled with Dye 2. In the current studies, I circumvented this issue by designing experimental paradigms that were shorter than the turnover window of each target construct. However, for broader application of HaloTag labeling techniques to track newly surface-exposed proteins in long-term synaptic dynamics studies, one could consider introducing point mutations that reduce endocytosis[165] or tethering the dye-labeled protein tag to a proximal scaffold protein with a slower turnover rate[166].

Overall, this work lays a robust foundation for future studies aimed at deciphering the dynamic interplay between synaptic activity, plasticity, and behavior in the brain.

The technical principles developed here not only advance our understanding of neural circuit mechanisms underlying learning and memory but also offer versatile tools that can be adapted to study the dynamics of other membrane proteins across a range of biological disciplines. I hope that both the technical innovations and scientific insights presented in this dissertation will significantly contribute to expanding our knowledge of cellular signaling processes and neural circuit function in diverse biological systems.

References

1. Kholodenko, B. N. Cell-signalling dynamics in time and space. *Nature reviews Molecular cell biology* **7**, 165–176 (2006).

2. Rizzoli, S. O. & Betz, W. J. Synaptic vesicle pools. *Nature Reviews Neuroscience* **6**, 57–69 (2005).

3. Südhof, T. C. Neurotransmitter release: the last millisecond in the life of a synaptic vesicle. *Neuron* **80**, 675–690 (2013).

4. Citri, A. & Malenka, R. C. Synaptic plasticity: multiple forms, functions, and mechanisms. *Neuropsychopharmacology* **33**, 18–41 (2008).

5. Neher, E. & Sakmann, B. The patch clamp technique. *Scientific American* **266**, 44–51 (1992).

6. Jiang, F. *et al.* Advances in the electrophysiological recordings of long-term potentiation. *International Journal of Molecular Sciences* **24**, 7134 (2023).

7. Scanziani, M. & Häusser, M. Electrophysiology in the age of light. *Nature* **461**, 930–939 (2009).

8. Jun, J. J. *et al.* Fully integrated silicon probes for high-density recording of neural activity. *Nature* **551**, 232–236 (2017).

9. Tian, L., Hires, S. A. & Looger, L. L. Imaging neuronal activity with genetically encoded calcium indicators. *Cold Spring Harbor Protocols* **2012**, pdb-top069609 (2012).

10. Xu, Y., Zou, P. & Cohen, A. E. Voltage imaging with genetically encoded indicators. *Current opinion in chemical biology* **39**, 1–10 (2017).

11. Grienberger, C. & Konnerth, A. Imaging calcium in neurons. *Neuron* **73**, 862–885 (2012).

12. Park, P. *et al.* Dendritic excitations govern back-propagation via a spike-rate accelerometer. *Nature Communications* **16**, 1333 (2025).

13. Wong-Campos, J. D. *et al.* Voltage dynamics of dendritic integration and back-propagation in vivo. *bioRxiv* (2023).

14. Stuyt, G., Godenzini, L. & Palmer, L. M. Local and global dynamics of dendritic activity in the pyramidal neuron. *Neuroscience* **489**, 176–184 (2022).

15. Marvin, J. S. *et al.* An optimized fluorescent probe for visualizing glutamate neurotransmission. *Nature methods* **10**, 162–170 (2013).

16. Li, S.-A. *et al.* Progress in pH-Sensitive sensors: essential tools for organelle pH detection, spotlighting mitochondrion and diverse applications. *Frontiers in Pharmacology* **14**, 1339518 (2024).

17. Granseth, B., Odermatt, B., Royle, S. J. & Lagnado, L. Clathrin-mediated endocytosis is the dominant mechanism of vesicle retrieval at hippocampal synapses. *Neuron* **51**, 773–786 (2006).

18. Voglmaier, S. M. *et al.* Distinct endocytic pathways control the rate and extent of synaptic vesicle protein recycling. *Neuron* **51**, 71–84 (2006).

19. Fu, M., Yu, X., Lu, J. & Zuo, Y. Repetitive motor learning induces coordinated formation of clustered dendritic spines in vivo. *Nature* **483**, 92–95 (2012).

20. Roth, R. H. *et al.* Cortical synaptic AMPA receptor plasticity during motor learning. *Neuron* **105**, 895–908 (2020).

21. Tan, H. L., Roth, R. H., Graves, A. R., Cudmore, R. H. & Huganir, R. L. Lamina-specific AMPA receptor dynamics following visual deprivation in vivo. *Elife* **9**, e52420 (2020).

22. Horton, N. G. *et al.* In vivo three-photon microscopy of subcortical structures within an intact mouse brain. *Nature photonics* **7**, 205–209 (2013).

23. Fan, J. L. *et al.* High-speed volumetric two-photon fluorescence imaging of neurovascular dynamics. *Nature communications* **11**, 6020 (2020).

24. Zhang, Y., Cudmore, R. H., Lin, D.-T., Linden, D. J. & Huganir, R. L. Visualization of NMDA receptor–dependent AMPA receptor synaptic plasticity in vivo. *Nature neuroscience* **18**, 402–407 (2015).

25. Mizuta, K. & Sato, M. Multiphoton imaging of hippocampal neural circuits: techniques and biological insights into region-, cell-type-, and pathway-specific functions. *Neurophotonics* **11**, 033406–033406 (2024).

26. Aharoni, D. & Hoogland, T. M. Circuit investigations with open-source miniaturized microscopes: past, present and future. *Frontiers in cellular neuroscience* **13**, 141 (2019).

27. Berndt, A. *et al.* Current Status and Future Strategies for Advancing Functional Circuit Mapping In Vivo. *Journal of Neuroscience* **43**, 7587–7598 (2023).

28. Kolberg, K., Puettmann, C., Pardo, A., Fitting, J. & Barth, S. SNAP-tag technology: a general introduction. *Current pharmaceutical design* **19**, 5406–5413 (2013).

29. England, C. G., Luo, H. & Cai, W. HaloTag technology: a versatile platform for biomedical applications. *Bioconjugate chemistry* **26**, 975–986 (2015).

30. Ly, C. *et al.* Psychedelics promote structural and functional neural plasticity. *Cell reports* **23**, 3170–3182 (2018).

31. Wang, X., Christian, K. M., Song, H. & Ming, G. Synaptic dysfunction in complex psychiatric disorders: from genetics to mechanisms. *Genome medicine* **10**, 1–3 (2018).

32. Neher, E. & Sakaba, T. Multiple roles of calcium ions in the regulation of neurotransmitter release. *Neuron* **59**, 861–872 (2008).

33. Lai, Y. *et al.* Molecular mechanisms of synaptic vesicle priming by Munc13 and Munc18. *Neuron* **95**, 591–607 (2017).

34. Brunger, A. T. Structure and function of SNARE and SNARE-interacting proteins. *Quarterly reviews of biophysics* **38**, 1–47 (2005).

35. Bennett, M. K., Calakos, N. & Scheller, R. H. Syntaxin: a synaptic protein implicated in docking of synaptic vesicles at presynaptic active zones. *Science* **257**, 255–259 (1992).

36. Hodel, A. SNAP-25. *The international journal of biochemistry & cell biology* **30**, 1069–1073 (1998).

37. Chapman, E. R. How does synaptotagmin trigger neurotransmitter release? *Annu. Rev. Biochem.* **77**, 615–641 (2008).

38. Nakanishi, S. Metabotropic glutamate receptors: synaptic transmission, modulation, and plasticity. *Neuron* **13**, 1031–1037 (1994).

39. Gouaux, E. Structure and function of AMPA receptors. *The Journal of physiology* **554**, 249–253 (2004).

40. Mori, H. & Mishina, M. Structure and function of the NMDA receptor channel. *Neuropharmacology* **34**, 1219–1237 (1995).

41. Fon, E. A. & Edwards, R. H. Molecular mechanisms of neurotransmitter release. *Muscle & Nerve: Official Journal of the American Association of Electrodiagnostic Medicine* **24**, 581–601 (2001).

42. Evans, G. & Cousin, M. Tyrosine phosphorylation of synaptophysin in synaptic vesicle recycling. *Biochemical Society Transactions* **33**, 1350–1353 (2005).

43. Kwon, S. E. & Chapman, E. R. Synaptophysin regulates the kinetics of synaptic vesicle endocytosis in central neurons. *Neuron* **70**, 847–854 (2011).

44. Hinz, B. *et al.* Activity-dependent changes of the presynaptic synaptophysin-synaptobrevin complex in adult rat brain. *European journal of cell biology* **80**, 615–619 (2001).

45. Du, X. *et al.* Research progress on the role of type I vesicular glutamate transporter (VGLUT1) in nervous system diseases. *Cell & bioscience* **10**, 1–10 (2020).

46. Lynch, M. A. Long-term potentiation and memory. *Physiological reviews* **84**, 87–136 (2004).

47. Lisman, J., Yasuda, R. & Raghavachari, S. Mechanisms of CaMKII action in long-term potentiation. *Nature reviews neuroscience* **13**, 169–182 (2012).

48. Carvalho, A. L., Duarte, C. B. & Carvalho, A. P. Regulation of AMPA receptors by phosphorylation. *Neurochemical research* **25**, 1245–1255 (2000).

49. Benke, T. & Traynelis, S. F. AMPA-type glutamate receptor conductance changes and plasticity: still a lot of noise. *Neurochemical Research* **44**, 539–548 (2019).

50. Choquet, D. & Opazo, P. The role of AMPAR lateral diffusion in memory. in vol. 125 76–83 (Elsevier, 2022).

51. Patterson, M. A., Szatmari, E. M. & Yasuda, R. AMPA receptors are exocytosed in stimulated spines and adjacent dendrites in a Ras-ERK–dependent manner during

long-term potentiation. *Proceedings of the National Academy of Sciences* **107**, 15951–15956 (2010).

52. Dunwiddie, T. & Lynch, G. Long-term potentiation and depression of synaptic responses in the rat hippocampus: localization and frequency dependency. *The Journal of physiology* **276**, 353–367 (1978).

53. Mulkey, R. M., Endo, S., Shenolikar, S. & Malenka, R. C. Involvement of a calcineurin/inhibitor-1 phosphatase cascade in hippocampal long-term depression. *Nature* **369**, 486–488 (1994).

54. Lee, H.-K., Kameyama, K., Huganir, R. L. & Bear, M. F. NMDA induces long-term synaptic depression and dephosphorylation of the GluR1 subunit of AMPA receptors in hippocampus. *Neuron* **21**, 1151–1162 (1998).

55. Diering, G. H. & Huganir, R. L. The AMPA receptor code of synaptic plasticity. *Neuron* **100**, 314–329 (2018).

56. Lüscher, C. & Huber, K. M. Group 1 mGluR-dependent synaptic long-term depression: mechanisms and implications for circuitry and disease. *Neuron* **65**, 445–459 (2010).

57. Leuner, B. & Shors, T. J. New spines, new memories. *Molecular neurobiology* **29**, 117–130 (2004).

58. Fosque, B. F. *et al.* Labeling of active neural circuits in vivo with designed calcium integrators. *Science* **347**, 755–760 (2015).

59. Hyun, J. H. *et al.* Tagging active neurons by soma-targeted Cal-Light. *Nature communications* **13**, 7692 (2022).

60. Kim, C. K. *et al.* A molecular calcium integrator reveals a striatal cell type driving aversion. *Cell* **183**, 2003–2019 (2020).

61. Sanchez, M. I., Nguyen, Q.-A., Wang, W., Soltesz, I. & Ting, A. Y. Transcriptional readout of neuronal activity via an engineered Ca2+-activated protease. *Proceedings of the National Academy of Sciences* **117**, 33186–33196 (2020).

62. Muir, J. *et al.* Isolation of psychedelic-responsive neurons underlying anxiolytic behavioral states. *Science* **386**, 802–810 (2024).

63. Perez-Alvarez, A. *et al.* Freeze-frame imaging of synaptic activity using SynTagMA. *Nature communications* **11**, 2464 (2020).

64. Gobbo, F. *et al.* Activity-dependent expression of Channelrhodopsin at neuronal synapses. *Nature communications* **8**, 1629 (2017).

65. Ferro, M. *et al.* Functional mapping of brain synapses by the enriching activity-marker SynaptoZip. *Nature communications* **8**, 1229 (2017).

66. Choi, J.-H. *et al.* Interregional synaptic maps among engram cells underlie memory formation. *Science* **360**, 430–435 (2018).

67. Parot, V. J. All-optical neurophysiology using high-speed wide-area optical sectioning. (2019).

68. Wilhelm, J. *et al.* Kinetic and structural characterization of the self-labeling protein tags HaloTag7, SNAP-tag, and CLIP-tag. *Biochemistry* **60**, 2560–2575 (2021).

69. Los, G. V. *et al.* HaloTag: a novel protein labeling technology for cell imaging and protein analysis. *ACS chemical biology* **3**, 373–382 (2008).

70. Gautier, A. *et al.* An engineered protein tag for multiprotein labeling in living cells. *Chemistry & biology* **15**, 128–136 (2008).

71. Lin, D. *et al.* Time-tagged ticker tapes for intracellular recordings. *Nature Biotechnology* 1–9 (2023).

72. Huppertz, M.-C. *et al.* Recording physiological history of cells with chemical labeling. *Science* **383**, 890–897 (2024).

73. Keith, D. J. & El-Husseini, A. Excitation control: balancing PSD-95 function at the synapse. *Frontiers in molecular neuroscience* **1**, 200 (2008).

74. Bulovaite, E. *et al.* A brain atlas of synapse protein lifetime across the mouse lifespan. *Neuron* **110**, 4057–4073 (2022).

75. Mohar, B. *et al.* Brain-wide measurement of protein turnover with high spatial and temporal resolution. *bioRxiv* 2022–11 (2022).

76. Martin, S. J., Grimwood, P. D. & Morris, R. G. Synaptic plasticity and memory: an evaluation of the hypothesis. *Annual review of neuroscience* **23**, 649–711 (2000).

77. Wu, Q.-L., Gao, Y., Li, J.-T., Ma, W.-Y. & Chen, N.-H. The role of AMPARs composition and trafficking in synaptic plasticity and diseases. *Cellular and Molecular Neurobiology* **42**, 2489–2504 (2022).

78. Kim, J. *et al.* mGRASP enables mapping mammalian synaptic connectivity with light microscopy. *Nat Methods* **9**, 96–102 (2012).

79. Dore, K. *et al.* SYNPLA, a method to identify synapses displaying plasticity after learning. *Proceedings of the National Academy of Sciences* **117**, 3214–3219 (2020).

80. Getz, A. M. *et al.* High-resolution imaging and manipulation of endogenous AMPA receptor surface mobility during synaptic plasticity and learning. *Science Advances* **8**, eabm5298 (2022).

81. Kastellakis, G. & Poirazi, P. Synaptic clustering and memory formation. *Frontiers in molecular neuroscience* **12**, 300 (2019).

82. Watson, J. F., Ho, H. & Greger, I. H. Synaptic transmission and plasticity require AMPA receptor anchoring via its N-terminal domain. *Elife* **6**, e23024 (2017).

83. Bensussen, S. *et al.* A viral toolbox of genetically encoded fluorescent synaptic tags. *Iscience* **23**, (2020).

84. Xie, L. *et al.* A dynamic interplay of enhancer elements regulates Klf4 expression in naïve pluripotency. *Genes & Development* **31**, 1795–1808 (2017).

85. Kleinjan, M. S. *et al.* Dually innervated dendritic spines develop in the absence of excitatory activity and resist plasticity through tonic inhibitory crosstalk. *Neuron* **111**, 362–371 (2023).

86. Wong, V. *et al.* Plasticity-induced actin polymerization in the dendritic shaft regulates intracellular AMPA receptor trafficking. *bioRxiv* 2022–05 (2022).

87. Lu, W. *et al.* Subunit composition of synaptic AMPA receptors revealed by a single-cell genetic approach. *Neuron* **62**, 254–268 (2009).

88. Dörrbaum, A. R., Kochen, L., Langer, J. D. & Schuman, E. M. Local and global influences on protein turnover in neurons and glia. *Elife* **7**, e34202 (2018).

89. Trachtenberg, J. T. *et al.* Long-term in vivo imaging of experience-dependent synaptic plasticity in adult cortex. *Nature* **420**, 788–794 (2002).

90. Barrientos, S. A. & Tiznado, V. Hippocampal CA1 subregion as a context decoder. *Journal of Neuroscience* **36**, 6602–6604 (2016).

91. Ramirez, S. *et al.* Creating a false memory in the hippocampus. *Science* **341**, 387–391 (2013).

92. Josselyn, S. A. & Tonegawa, S. Memory engrams: Recalling the past and imagining the future. *Science* **367**, eaaw4325 (2020).

93. Hebb, D. O. *The Organization of Behavior: A Neuropsychological Theory*. (Psychology press, 2005).

94. Han, D. H., Park, P., Choi, D. I., Bliss, T. V. & Kaang, B.-K. The essence of the engram: cellular or synaptic? in vol. 125 122–135 (Elsevier, 2022).

95. Curzon, P., Rustay, N. R. & Browman, K. E. Cued and contextual fear conditioning for rodents. (2011).

96. Park, K. & Chung, C. Systemic cellular activation mapping of an extinction-impaired animal model. *Frontiers in cellular neuroscience* **13**, 99 (2019).

97. Magee, J. C. & Grienberger, C. Synaptic plasticity forms and functions. *Annual review of neuroscience* **43**, 95–117 (2020).

98. Arai, A., Black, J. & Lynch, G. Origins of the variations in long-term potentiation between synapses in the basal versus apical dendrites of hippocampal neurons. *Hippocampus* **4**, 1–9 (1994).

99. Branco, T. & Häusser, M. The single dendritic branch as a fundamental functional unit in the nervous system. *Current opinion in neurobiology* **20**, 494–502 (2010).

100. Landau, A. T. *et al.* Dendritic branch structure compartmentalizes voltage-dependent calcium influx in cortical layer 2/3 pyramidal cells. *Elife* **11**, e76993 (2022).

101. Makino, H. & Malinow, R. Compartmentalized versus global synaptic plasticity on dendrites controlled by experience. *Neuron* **72**, 1001–1011 (2011).

102. Bloss, E. B. *et al.* Single excitatory axons form clustered synapses onto CA1 pyramidal cell dendrites. *Nature neuroscience* **21**, 353–363 (2018).

103. Murakoshi, H., Wang, H. & Yasuda, R. Local, persistent activation of Rho GTPases during plasticity of single dendritic spines. *Nature* **472**, 100–104 (2011).

104. Routtenberg, A. & Rekart, J. L. Post-translational protein modification as the substrate for long-lasting memory. *Trends in neurosciences* **28**, 12–19 (2005).

105. Park, P. *et al.* The role of calcium-permeable AMPARs in long-term potentiation at principal neurons in the rodent hippocampus. *Frontiers in synaptic neuroscience* **10**, 42 (2018).

106. Plitt, M. H., Kaganovsky, K., Südhof, T. C. & Giocomo, L. M. Hippocampal place code plasticity in CA1 requires postsynaptic membrane fusion. *bioRxiv* (2023).

107. Shi, S. *et al.* Syntaxin-3 is dispensable for basal neurotransmission and synaptic plasticity in postsynaptic hippocampal CA1 neurons. *Sci Rep* **10**, 709 (2020).

108. Huang, M. *et al.* Neuronal SNAP-23 is critical for synaptic plasticity and spatial memory independently of NMDA receptor regulation. *iScience* **26**, 106664 (2023).

109. Graves, A. R. *et al.* Visualizing synaptic plasticity in vivo by large-scale imaging of endogenous AMPA receptors. *Elife* **10**, e66809 (2021).

110. Xu, Y. K. T. *et al.* Cross-modality supervised image restoration enables nanoscale tracking of synaptic plasticity in living mice. *Nat Methods* **20**, 935–944 (2023).

111. Wang, C. *et al.* Multiplexed aberration measurement for deep tissue imaging in vivo. *Nature methods* **11**, 1037–1040 (2014).

112. Juczewski, K., Koussa, J. A., Kesner, A. J., Lee, J. O. & Lovinger, D. M. Stress and behavioral correlates in the head-fixed method: stress measurements, habituation dynamics, locomotion, and motor-skill learning in mice. *Scientific reports* **10**, 1–19 (2020).

113. Gibson, D. G. *et al.* Enzymatic assembly of DNA molecules up to several hundred kilobases. *Nature methods* **6**, 343–345 (2009).

114. Tian, H. *et al.* Video-based pooled screening yields improved far-red genetically encoded voltage indicators. *Nature Methods* 1–13 (2023).

115. Manders, E., Verbeek, F. & Aten, J. Measurement of co-localization of objects in dual-colour confocal images. *Journal of microscopy* **169**, 375–382 (1993).

116. Goldey, G. J. *et al.* Removable cranial windows for long-term imaging in awake mice. *Nature protocols* **9**, 2515–2538 (2014).

117. Adam, Y. *et al.* Voltage imaging and optogenetics reveal behaviour-dependent changes in hippocampal dynamics. *Nature* **569**, 413–417 (2019).

118. Holtmaat, A., Wilbrecht, L., Knott, G. W., Welker, E. & Svoboda, K. Experience-dependent and cell-type-specific spine growth in the neocortex. *Nature* **441**, 979–983 (2006).

119. Seaton, G. *et al.* Dual-component structural plasticity mediated by αCaMKII

autophosphorylation on basal dendrites of cortical layer 2/3 neurones. *Journal of Neuroscience* **40**, 2228–2245 (2020).

120. Kim, D. *et al.* Mapping memories: pulse-chase labeling reveals AMPA receptor dynamics during memory formation. *bioRxiv* 2023–05 (2023).

121. Gobbo, F. & Cattaneo, A. Neuronal activity at synapse resolution: reporters and effectors for synaptic neuroscience. *Frontiers in Molecular Neuroscience* **13**, 572312 (2020).

122. Chen, T.-W. *et al.* Ultrasensitive fluorescent proteins for imaging neuronal activity. *Nature* **499**, 295–300 (2013).

123. Miesenböck, G., De Angelis, D. A. & Rothman, J. E. Visualizing secretion and synaptic transmission with pH-sensitive green fluorescent proteins. *Nature* **394**, 192–195 (1998).

124. Ryan, T. A. *et al.* The kinetics of synaptic vesicle recycling measured at single presynaptic boutons. *Neuron* **11**, 713–724 (1993).

125. Egashira, Y., Kumade, A., Ojida, A. & Ono, F. Spontaneously recycling synaptic vesicles constitute readily releasable vesicles in intact neuromuscular synapses. *Journal of Neuroscience* **42**, 3523–3536 (2022).

126. Hochbaum, D. R. *et al.* All-optical electrophysiology in mammalian neurons using engineered microbial rhodopsins. *Nature methods* **11**, 825–833 (2014).

127. Rienecker, K. D., Poston, R. G. & Saha, R. N. Merits and limitations of studying neuronal depolarization-dependent processes using elevated external potassium. *ASN neuro* **12**, 1759091420974807 (2020).

128. Schikorski, T. & Stevens, C. F. Morphological correlates of functionally defined synaptic vesicle populations. *Nature neuroscience* **4**, 391–395 (2001).

129. Oh, S. W. *et al.* A mesoscale connectome of the mouse brain. *Nature* **508**, 207–214 (2014).

130. Bullmore, E. & Sporns, O. Complex brain networks: graph theoretical analysis of structural and functional systems. *Nature reviews neuroscience* **10**, 186–198 (2009).

131. Cook, A., Walterspiel, F. & Deo, C. HaloTag-Based Reporters for Fluorescence Imaging and Biosensing. *ChemBioChem* **24**, e202300022 (2023).

132. DeVos, S. L. & Miller, T. M. Direct intraventricular delivery of drugs to the rodent central nervous system. *Journal of visualized experiments: JoVE* 50326 (2013).

133. Chan, K. Y. *et al.* Engineered AAVs for efficient noninvasive gene delivery to the central and peripheral nervous systems. *Nature neuroscience* **20**, 1172–1179 (2017).

134. Li, Z. *et al.* Synaptic vesicle recycling studied in transgenic mice expressing synaptopHluorin. *Proceedings of the National Academy of Sciences* **102**, 6131–6136 (2005).

135. Lim, D. H., LeDue, J., Mohajerani, M. H., Vanni, M. P. & Murphy, T. H. Optogenetic approaches for functional mouse brain mapping. *Frontiers in neuroscience* **7**, 54 (2013).

136. Shepard, B. D., Natarajan, N., Protzko, R. J., Acres, O. W. & Pluznick, J. L. A cleavable N-terminal signal peptide promotes widespread olfactory receptor surface expression in HEK293T cells. *PloS one* **8**, e68758 (2013).

137. Gradinaru, V. *et al.* Molecular and cellular approaches for diversifying and extending optogenetics. *Cell* **141**, 154–165 (2010).

138. Yang, G. *et al.* Sleep promotes branch-specific formation of dendritic spines after learning. *Science* **344**, 1173–1178 (2014).

139. Hwang, E. J., Dahlen, J. E., Mukundan, M. & Komiyama, T. Disengagement of motor cortex during long-term learning tracks the performance level of learned movements. *Journal of Neuroscience* **41**, 7029–7047 (2021).

140. Yuste, R. & Tank, D. W. Dendritic integration in mammalian neurons, a century after Cajal. *Neuron* **16**, 701–716 (1996).

141. Stuart, G. J. & Spruston, N. Dendritic integration: 60 years of progress. *Nature neuroscience* **18**, 1713–1721 (2015).

142. Kida, H., Toyoshima, S., Kawakami, R., Sakimoto, Y. & Mitsushima, D. Properties of layer V pyramidal neurons in the primary motor cortex that represent acquired motor skills. *Neuroscience* **559**, 54–63 (2024).

143. Ma, L. *et al.* Experience-dependent plasticity of dendritic spines of layer 2/3 pyramidal neurons in the mouse cortex. *Developmental neurobiology* **76**, 277–286 (2016).

144. Zhang, L., Getz, S. A. & Bordey, A. Dual in utero electroporation in mice to

manipulate two specific neuronal populations in the developing cortex. *Frontiers in Bioengineering and Biotechnology* **9**, 814638 (2022).

145. Sehgal, M. *et al.* Compartmentalized dendritic plasticity in the mouse retrosplenial cortex links contextual memories formed close in time. *Nature Neuroscience* 1–14 (2025).

146. Dobrunz, L. E. & Stevens, C. F. Heterogeneity of release probability, facilitation, and depletion at central synapses. *Neuron* **18**, 995–1008 (1997).

147. Regehr, W. G. Short-term presynaptic plasticity. *Cold Spring Harbor perspectives in biology* **4**, a005702 (2012).

148. Castro-Alamancos, M. A. & Connors, B. W. Distinct forms of short-term plasticity at excitatory synapses of hippocampus and neocortex. *Proceedings of the National Academy of Sciences* **94**, 4161–4166 (1997).

149. Grillo, F. W. *et al.* A distance-dependent distribution of presynaptic boutons tunes frequency-dependent dendritic integration. *Neuron* **99**, 275–282 (2018).

150. Catterall, W. A., Leal, K. & Nanou, E. Calcium channels and short-term synaptic plasticity. *Journal of Biological Chemistry* **288**, 10742–10749 (2013).

151. Matz, J., Gilyan, A., Kolar, A., McCarvill, T. & Krueger, S. R. Rapid structural alterations of the active zone lead to sustained changes in neurotransmitter release. *Proceedings of the National Academy of Sciences* **107**, 8836–8841 (2010).

152. Burrone, J., Neves, G., Gomis, A., Cooke, A. & Lagnado, L. Endogenous calcium buffers regulate fast exocytosis in the synaptic terminal of retinal bipolar cells. *Neuron* **33**, 101–112 (2002).

153. Schirra Jr, R. T. & Zhang, P. Correlative fluorescence and electron microscopy. *Current protocols in cytometry* **70**, 12–36 (2014).

154. Wen, G., Leen, V., Rohand, T., Sauer, M. & Hofkens, J. Current progress in expansion microscopy: chemical strategies and applications. *Chemical Reviews* **123**, 3299–3323 (2023).

155. Eisenstein, M. A milestone map of mouse-brain connectivity reveals challenging new terrain for scientists. *Nature* **628**, 677–679 (2024).

156. Selten, M., van Bokhoven, H. & Kasri, N. N. Inhibitory control of the excitatory/inhibitory balance in psychiatric disorders. *F1000Research* **7**, 23 (2018).

157. Anderson, J. S., Carandini, M. & Ferster, D. Orientation tuning of input conductance, excitation, and inhibition in cat primary visual cortex. *Journal of neurophysiology* **84**, 909–926 (2000).

158. He, H.-Y., Shen, W., Hiramoto, M. & Cline, H. T. Experience-dependent bimodal plasticity of inhibitory neurons in early development. *Neuron* **90**, 1203–1214 (2016).

159. Fan, L. Z. *et al.* All-optical electrophysiology reveals the role of lateral inhibition in sensory processing in cortical layer 1. *Cell* **180**, 521–535 (2020).

160. Zhang, Z., Jiao, Y.-Y. & Sun, Q.-Q. Developmental maturation of excitation and inhibition balance in principal neurons across four layers of somatosensory cortex. *Neuroscience* **174**, 10–25 (2011).

161. Kühn, S. *et al.* SNAP-tag2: faster and brighter protein labeling. *bioRxiv* 2024–08 (2024).

162. Qian, Y., Celiker, O. T., Wang, Z., Guner-Ataman, B. & Boyden, E. S. Temporally multiplexed imaging of dynamic signaling networks in living cells. *Cell* **186**, 5656–5672 (2023).

163. Chen, K. H., Boettiger, A. N., Moffitt, J. R., Wang, S. & Zhuang, X. Spatially resolved, highly multiplexed RNA profiling in single cells. *Science* **348**, aaa6090 (2015).

164. Lubeck, E., Coskun, A. F., Zhiyentayev, T., Ahmad, M. & Cai, L. Single-cell in situ RNA profiling by sequential hybridization. *Nature methods* **11**, 360–361 (2014).

165. Bucher, M. *et al.* Autism-associated SHANK3 missense point mutations impact conformational fluctuations and protein turnover at synapses. *Elife* **10**, e66165 (2021).

166. Heo, S. *et al.* Identification of long-lived synaptic proteins by proteomic analysis of synaptosome protein turnover. *Proceedings of the National Academy of Sciences* **115**, E3827–E3836 (2018).